UNIVERSITY OF CINCINNATI

DATE: May 8, 2002

I, Vincent Wu ,

hereby submit this as part of the requirements for the degree of:

Doctor of Philosophy

in:

Physics

It is entitled:

Design and Testing of a High Gradient Radio Frequency Cavity for the Muon Collider

Approved by:

Randy Johnson

Robert Endorf

Michael Sokoloff

Peter Suranyi

Design and Testing of a High Gradient Radio Frequency Cavity for the Muon Collider

A dissertation submitted to the

Division of Research and Advanced Studies
of the University of Cincinnati

in partial fulfillment of the
requirements for the degree of

DOCTORATE OF PHILOSOPHY (Ph.D.)

in the Department of Physics
of the College of Arts and Sciences

2002

by

Vincent Wu

B.S., State University of New York at Binghamton, 1993
M.S., University of Cincinnati, 1997

Committee Chair: Dr. Randy Johnson

To my parents, with profound gratitude.

Abstract

This thesis describes the design and testing of a high gradient RF cavity for the muon cooling channel of the muon collider. The 805 MHz multi-cell open iris cavity was high power tested with a 12 MW klystron in a superconducting solenoid environment. The cavity reached 21 MV/m for peak klystron power in the absence of the solenoidal field. During magnetic field operation, the cavity suffered serious surface damage and RF breakdown. Dark current in excess of 400 mA was observed. Present R & D results imply that the cavity is not suitable for the muon collider.

Acknowledgments

As with any experimental effort, many people have contributed to the successful completion of this project. My foremost thank goes to my thesis advisors Randy Johnson and Norbert Holtkamp for their constant support and guidance throughout my thesis research.

Next, I would like to thank Al Moretti, Derun Li, Zubao Qian, Tom Jurgens and Mark Champion for whom I have learned a great deal about the design and testing of RF cavity. They were always there to help when I needed them.

I thank Steve Geer (MUCOOL spokesperson) and Norbert Holtkamp for their relentless support of the project which kept the project alive during times of Fermilab budgetary cuts.

I thank the following Fermilab engineers and technicians for their hard work in planning and putting all the cavity sub-systems together: Allan Rowe, Dan Snee, Tim Hamerla, Arnold Germaine, Peter prieto, Karl Williams, Alex Martinez, Kermit Carlson, and Mike Foley.

I had the pleasure of working with Jim Norem, Lauren Ducas, Yagmur Torun, Nick Solomey and Milorad Popovic during the high power test of the cavity.

Contents

List of Tables

List of Figures

Chapter 1

Introduction

High energy particle accelerators are the dominant tools to study and understand the basic building blocks of matter. In high energy physics experiments, particles such as protons or electrons are accelerated to hundreds of GeV and allowed to collide with each other or into fixed targets. New particles are created from the high energy collisions, and their interactions and properties are studied using sophisticated detectors. High energy accelerators such as the Fermilab Tevatron (1 TeV proton and antiproton collider), the CERN LEP (101 GeV electron and positron collider) and the SLAC SLC (50 GeV electron and positron linear collider) have discovered many fundamental particles and advanced our knowledge of the basic forces of nature.

The Standard Model of electroweak and strong interactions has passed precision experimental tests at the highest energy scale accessible. Theoretical arguments indicate that new physics beyond the Standard Model associated with the electroweak gauge symmetry breaking and fermion mass generation will emerge in parton collisions at or approaching the TeV energy scale. The search for the Higgs boson which is considered to be the source of mass generation under the mechanism of spontaneous

symmetry breaking is one of the most important problems for the next generation of high energy accelerators.

The next energy frontier for the hadron machine will be the CERN Large Hadron Collider (LHC) which is a proton-proton collider with 14 TeV center of mass energy (CoM). The LHC will provide hard parton-parton collisions with typical CoM of 1 to 3 TeV. The LHC is several times the size of Fermilab and is probably approaching maximum cost and size limitation of feasible hadronic machines. Furthermore the effectiveness of a hadron machine is limited by the composite nature of hadrons. Because hadrons are composite particles, both the number and CoM energy of point-like interaction increase slowly with rising accelerator energy.

Conventional circular lepton machines may have already met their limit with the 202 GeV CoM energy (maximum) achieved by the LEP collider. The extension beyond LEP to the multi-TeV energies is constrained by beam-beam interaction and synchrotron radiation effects. The synchrotron radiation problem can be avoided by using two full energy electron and positron linacs. However, with current technology, a linear collider must be very long (30 to 40 km) to attain the TeV energy scale.

Some of the problems faced by future proton and electron machines can be avoided by using muons (heavy leptons). The synchrotron radiation loss produced in a given circular machine is inversely proportional to $(\text{mass})^4$. The muons, with a mass of about 207 times that of the electrons, would have negligible synchrotron radiation loss. This advantage allows higher CoM energy and smaller collider ring for particle collisions. A conceptual study [1] shows that a 4 TeV muon collider will fit within the

boundaries of existing laboratories such as Fermilab and Brookhaven. Small radiative loss also makes small beam energy spread achievable. Precise energy determination together with small beam energy spread will facilitate measurements of masses and widths of any new particle states found by the collider.

Besides the advantages from the machine point of view, a muon collider has unique physics potentials. Since the cross section for producing a Higgs-like scalar particle is proportional to the mass square of the incoming particles, the muon collider will be a unique Higgs factory. Measurements can also be made of the threshold cross sections for production of W^+W^-, t^+t^-, Zh and pairs of supersymmetric particles. This will determine the corresponding masses to high precision. In addition, the muon collider provides an intense neutrino beam that will be several orders of magnitude higher in particle flux than those presently available. It will permit extended studies of neutrino oscillations, nucleon structure functions, CKM matrix, *etc.* There are numerous other new physics possibilities for the muon collider suggested in the literatures [2, 3].

With all these advantages over the proton and electron machines, however, the muon collider has shortcomings. The major liability of the muon machines is the continuous decay of muons. (Muon lifetime is 2.2 μsec.) The enormous radiation from the muon decay is a serious problem for the machine components and the physics detectors. For a high luminosity collider, a large number of muons needs to be collected. These muons come from pion decay and the pions are produced in proton-nucleus interaction. Naturally, the result of this multi-step production process is that the muons occupy a large phase space volume (beam size), which must be reduced

before they are accelerated to high energy. For a practical collider, a cooling factor (in 6 dimensional phase space volume reduction) of 10^5 to 10^6 is required.

The cooling method that satisfies the cooling requirement within the time scale of the muon lifetime is ionization cooling. During ionization cooling, muons pass through some absorber material, losing both transverse and longitudinal momenta. The lost longitudinal momentum is then retrieved by coherent acceleration in high gradient RF cavities. This process results in a net loss of transverse momenta for the muons, and consequently in transverse cooling. Longitudinal cooling is accomplished by using wedge absorber. Higher energy muons are made to pass through more material than lower energy muons do. As a result, the energy spread of the muons is reduced (*i.e.*, longitudinal cooling). The ionization cooling technique is uniquely applicable to muons because of (1) their absence of strong nuclear interaction and (2) minimal electromagnetic shower production for muons at energies around 200 MeV/c.

In recent years, the muon collider collaboration launched an active research and development (R & D) program at Fermilab (called MUCOOL) to study the feasibility of using the ionization cooling technique in realistic muon cooling channel design [4]. One of the major thrusts of this program is the design and test of suitable high gradient RF cavities. This thesis presents the design work, and the low and high power test results for a multi-cell open iris cavity for the transverse cooling channel.

1.1 MUCOOL: The Muon Ionization Cooling R & D Program

The goals of MUCOOL are to demonstrate the feasibility of ionization cooling, to produce a cooled muon beam and to develop the cooling hardware to the point where a complete ionization cooling channel can be confidently designed. Simulations of cooling channels are carried out to study cooling performance, beam dynamics and tolerances. Prototypes of the critical components are to be designed, constructed and tested to see that they achieve the operational parameters required for the real cooling channel. Then the prototypes of the cooling sections will be tested with incoming muons in the momentum range of 100 to 300 MeV/c. The phase space volume occupied by the population of muons upstream and downstream of the cooling sections will be measured so that cooling is demonstrated.

1.1.1 Ionization Cooling Concept

The idea of ionization cooling of muons is illustrated by the conceptual drawing in Fig. 1.1. A muon beam of large emittance[1], represented by momentum arrows with large divergence in Fig. 1.1, goes through a material medium and loses energy (or momentum) via ionization. Then it is accelerated in a RF cavity. Since the losses are parallel to the particle motion, both transverse and longitudinal momenta are reduced. The acceleration in RF cavity restores only the longitudinal momentum. At the cavity exit, the muons have smaller transverse momenta (*i.e.*, less beam divergence), and

[1]Emittance is the phase space volume of the canonical coordinates and momenta (q_i, p_i) occupied by the muons. Physically, a large emittance beam means that the particles have large position spread and divergent momenta.

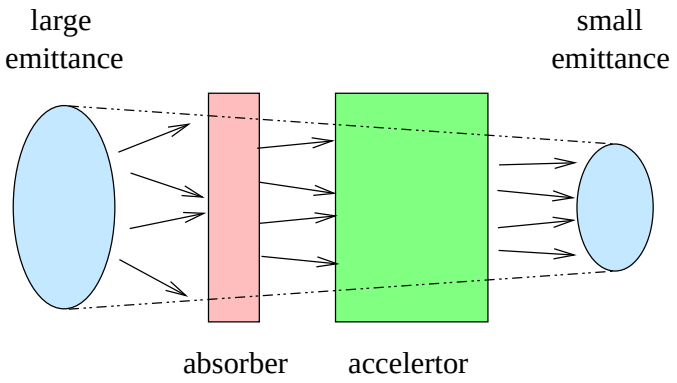

Figure 1.1: Concept of ionization cooling.

thus are cooler in the transverse direction. However, in addition to the ionization losses in the material, the muons also are scattering off the nuclei, a random process, which increases the beam divergence and gives rise to a beam heating effect.

The equation describing transverse cooling [5, 6, 7] is

$$\frac{d\epsilon_n}{ds} = -\frac{1}{\beta^2 E}\frac{dE}{ds}\epsilon_n + \frac{\beta_\perp (0.014)^2}{2\beta^3 m_\mu L_R E}, \tag{1.1}$$

where the first term is the ionization cooling effect and the second is the multiple scattering heating term. The variable ϵ_n is the normalized emittance of the beam. It is related to the geometric emittance $\epsilon_\perp$ by $\epsilon_n = \epsilon_\perp/(\beta\gamma)$, where $\beta = v/c$ and $\gamma = (1-\beta^2)^{-1/2}$. The variable E is the muon energy in GeV, dE/ds is the mean ionization energy loss rate, $\beta_\perp$ is the betatron function (which is related to the beam size σ_x by $\sigma_x = (\epsilon_\perp \beta_\perp)^{1/2}$), and L_R is the radiation length of the material medium. To get optimal cooling, the heating term must be minimized by making $\beta_\perp$ small (*e.g.*, putting absorber in region of strong focusing) and L_R large (*i.e.*, using low-Z absorber material such as liquid hydrogen).

Longitudinal cooling is needed to reduce the energy spread of the muon beam.

The equation for longitudinal cooling [8, 9] is

$$\frac{d\sigma_E^2}{ds} = -2\frac{\partial(dE/ds)}{\partial E}\sigma_E^2 + \frac{d(<\Delta E_{rms}^2>)}{ds}, \tag{1.2}$$

where σ_E is the energy spread. The first term results in cooling if $\partial(dE/ds)/\partial E > 0$. The second term is the heating due to the random fluctuations in the particle energy loss ($<\Delta E_{rms}^2>$). To achieve longitudinal cooling, one introduces a transverse variation in the absorber density or thickness (*i.e.*, using a wedge) at a location where there is dispersion[2]. The wedge will reduce the energy spread, but simultaneously increase the transverse emittance in the direction of the dispersion. Thus, longitudinal cooling is accomplished by the exchange of emittance between the longitudinal and transverse directions.

1.1.2 Alternating Solenoid Channel for Muon Cooling

Muon ionization cooling channels have three major constituents: (1) focusing elements to capture and confine the beam, (2) absorber materials to provide the ionization energy losses and (3) accelerators to replenish the longitudinal momentum lost in the absorbers. Solenoids are chosen as the primary focusing elements. To conserve space, the absorbers and the accelerators are placed inside the solenoids. Therefore, only normal conducting RF cavities can be used for acceleration.

The Alternating Solenoid Channel (ASC) is the design choice for the cooling channel of the muon collider. At the early cooling stages of the collider, the lattice of the ASC uses solenoids with alternating field directions. The schematic of a period of the cooling lattice is shown in Fig. 1.2. Within the channel, liquid hydrogen absorbers

[2]Dispersion is the dependence of the transverse position of the particles on the energy.

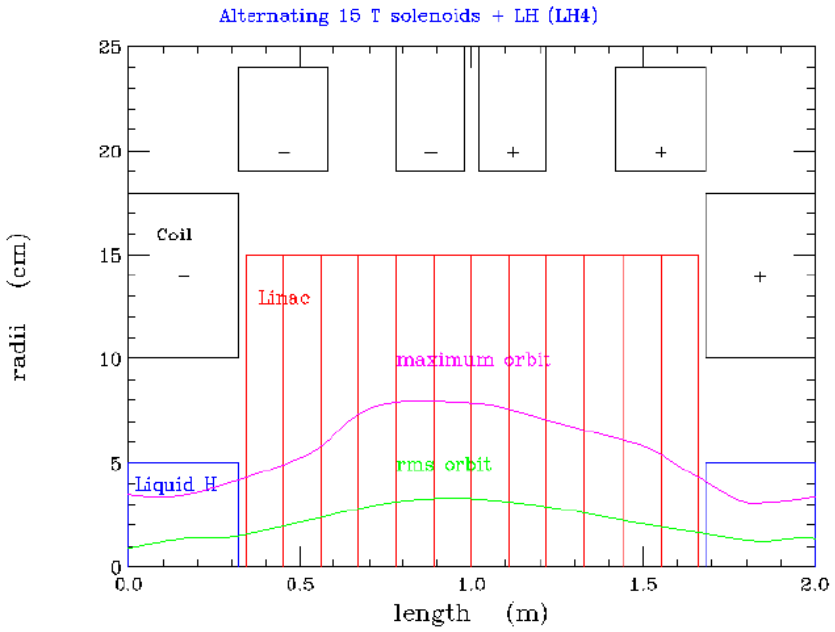

Figure 1.2: The schematic of a period of transverse cooling lattice. The plus and minus signs in the coil blocks refer to currents moving into or out of the paper, respectively.

are placed in high field regions (15 T) to minimize multiple scattering and the high gradient cavities are in matching sections of lower fields (5 T and 10 T). In order to minimize the final transverse emittance of the beam, the last few cooling sections require the strongest possible radial focusing. For this reason, very high field solenoids of 30 T and current carrying liquid lithium lenses are considered. The liquid lithium lenses can act as both absorber and focusing element.

1.1.3 R & D Program for High Gradient RF Cavities

One of the hardware R & D programs of MUCOOL is the high gradient RF cavity. There are two candidates for the MUCOOL cavities: (1) pill-box type of copper cavity with beryllium windows at the entrance and exit of the accelerating cells and (2)

copper cavity with open irises. Both cavities operate at 805 MHz and provide an accelerating gradient of 30 MV/m for an average muon momentum of 186 MeV/c. The beryllium window cavity is being developed at Lawrence Berkeley National Laboratory, the University of Mississippi and Fermilab. The open iris cavity is being developed at Fermilab. Both cavities are to be tested at high electric field in 5 T solenoidal field and powered with a 12 MW klystron at Fermilab.

Interleaved $\frac{\pi}{2}$ Mode Structure with Beryllium Windows

The beryllium window cavity as shown in Fig. 1.3 is a $\frac{\pi}{2}$ mode[3] standing wave struc-

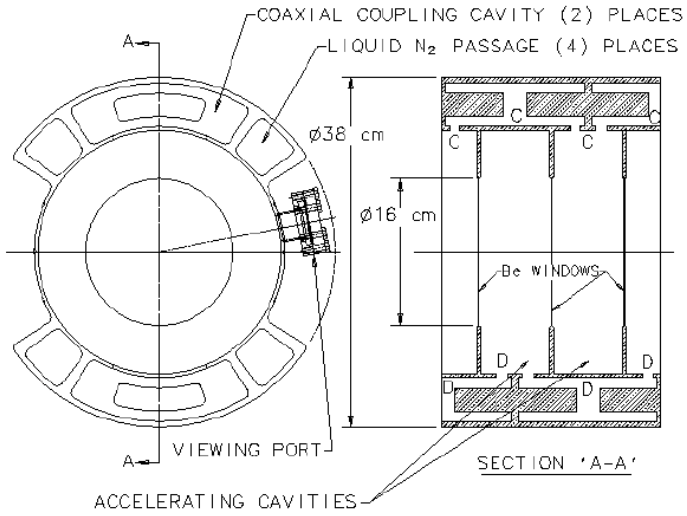

Figure 1.3: The MUCOOL beryllium window cavity.

ture[4]. The structure consists of two interleaved $\pi/2$ mode cavities that are electrically independent. Cell to cell couplings in each cavity are provided by side coupled coaxial cells. A unique feature of the cavity is the use of beryllium foils of 125 μm thickness which seals off the irises, resulting in pill-box type cell geometry. This yields higher accelerating gradient for a given input power to the cavity[5]. Another potential feature of the cavity is that it operates at liquid nitrogen temperature to reduce the resistivity of the cavity. This results in lower total RF system cost.

The beryllium window cavity is a novel device with some difficult and uncertain R & D issues. The mounting of the beryllium foils onto the copper irises in a manner which makes a good RF contact is a challenging engineering problem. Because of the different mechanical and thermal properties of beryllium and copper, the mechanical stability of the windows is questionable and tunability of the cavity may be difficult. Multipacting[6] at the beryllium windows in pill-box type of cell geometry can be a potential problem.

π Mode Structure with Open Irises

Of all the difficulties and uncertainties associated with the beryllium window cavity, the π mode[7] cavity without the use of beryllium windows is conceived as an alternative

[3]For RF cavities that operate at $\pi/2$ mode, the electric fields in adjacent cells are 90° out of phase.

[4]Cavities that are standing wave structures operate in resonant condition, *i.e.*, the electromagnetic fields in the cavities form standing waves.

[5]The reason for the higher accelerating gradient is that for pill box cavity the on axis field is the same as the surface field.

[6]Multipacting is a phenomenon where the electron emissions from the cavity surface are in resonant with the RF fields. In practice, multipacting can lead to large buildup of electrons in the cavity, resulting in large extraction of power from the RF fields and preventing the increase of the accelerating gradient.

[7]For π mode cavity, the electric fields in adjacent cells are 180° out of phase with each other.

cooling channel cavity. The π mode cavity is a multi-cell standing wave structure with open irises. Since the accelerating gradient of the open cell cavity is intrinsically lower than that of the close cell geometry for a given input power, the main challenge of the open iris cavity is the push for high gradient. The gradient in a cavity is limited by the breakdown field on the surface of the cavity and the amount of dark current emission. Thus, RF surface breakdown and the minimization of the dark current are the main issues of the open iris cavity. The detailed design work of the cavity is presented in chapter 3, and the cavity test results are presented in chapter 4 and 5.

Chapter 2

Theoretical Background

2.1 Transmission Line Theory

Transmission lines such as coaxial cables, cylindrical waveguides and microstrip lines are commonly used for power transmission in microwave and radio frequency applications. Generally, the coaxial cables are used in low power applications, the waveguides in high power applications, and the microstrip lines in integrated circuits. The operating frequencies in microwave and RF applications are in the range of about 10^8 to 10^{11} Hz (which corresponds to wavelengths of about 10^{-3} to 1 meter). Since the lengths of the transmission lines are comparable to or longer than the wavelengths, transmission lines are considered as distributed-parameter networks, where the magnitude and the phase of the voltages and the currents vary along the lines. This admits wave propagations in transmission lines.

Wave propagations in the transmission lines can be solved by equivalent circuit model. Schematically, a transmission line is represented by a two-wire line as shown in Fig. 2.1. We are interested in finding the wave solutions for the current and voltage as they propagate along the line. These solutions can be found by modeling the

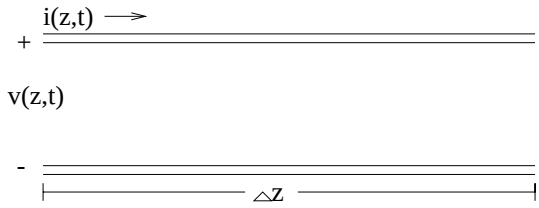

Figure 2.1: Two-wire representation of a transmission line.

transmission line by the circuit shown in Fig. 2.2 and applying Kirchhoff's laws. The

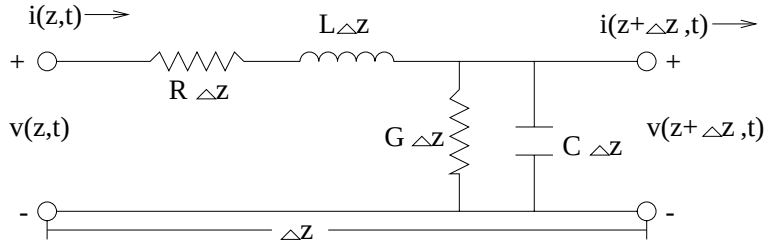

Figure 2.2: Equivalent circuit model of a transmission line.

conductor and the dielectric losses in the line are modeled by the series resistance $R\Delta z$ and the shunt conductance $G\Delta z$, respectively. The series inductance $L\Delta z$ represents the total self-inductance of the two conductors, and the shunt capacitance $C\Delta z$ represents the capacitance between the two conductors. Kirchhoff's law applied to this circuit yields the following two equations for the voltage v and the current i,

$$v(z,t) - R\Delta z\ i(z,t) - L\Delta z\frac{\partial}{\partial t}i(z,t) - v(z+\Delta z,t) = 0 \tag{2.1}$$

and

$$i(z,t) - G\Delta z\ v(z+\Delta z,t) - C\Delta z\frac{\partial}{\partial t}v(z+\Delta z,t) - i(z+\Delta z,t) = 0\ . \tag{2.2}$$

In the limit of $\Delta z \to 0$, Eqs. 2.1 and 2.2 become

$$\frac{\partial}{\partial z}v(z,t) = -R\ i(z,t) - L\frac{\partial}{\partial t}i(z,t) \tag{2.3}$$

and

$$\frac{\partial}{\partial z}i(z,t) = -G\ v(z,t) - C\frac{\partial}{\partial t}v(z,t)\ . \tag{2.4}$$

Assuming solutions with sinusoidal time dependence e^{iwt} where w is the angular frequency, Eqs. 2.3 and 2.4 can be combined to yield the equations for the voltage V and the current I,

$$\frac{d^2}{dz^2}V(z) - \gamma^2 V(z) = 0 \tag{2.5}$$

and

$$\frac{d^2}{dz^2}I(z) - \gamma^2 I(z) = 0\ , \tag{2.6}$$

where $\gamma = \sqrt{(R+iwL)(G+iwC)} = \alpha + ik_z$ is the complex propagation constant. The real part of γ is interpreted as the decay constant α describing the losses along the transmission line and the imaginary part is the wave propagation constant k_z. Traveling wave solutions to Eqs. 2.5 and 2.6 are

$$V(z) = V_\circ^+ e^{-\gamma z} + V_\circ^- e^{\gamma z} \tag{2.7}$$

and

$$I(z) = I_\circ^+ e^{-\gamma z} + I_\circ^- e^{\gamma z}\ , \tag{2.8}$$

where $V_\circ^+$ and $V_\circ^-$ are voltage amplitudes; $I_\circ^+$ and $I_\circ^-$ are current amplitudes propagating in the + and -z direction respectively. Inserting the wave solutions into Eq. 2.3 gives

$$I(z) = \frac{1}{Z_\circ}(V_\circ^+ e^{-\gamma z} - V_\circ^- e^{\gamma z})\ , \tag{2.9}$$

where $Z_\circ \equiv (R+iwL)/\gamma$ is the characteristic impedance of the transmission line. Comparison of Eq. 2.9 with the wave solutions implies that the characteristic impedance

can be expressed as $Z_\circ = V_\circ^+/I_\circ^+ = -V_\circ^-/I_\circ^-$. The wavelength λ and the velocity v_p of the traveling waves are defined as $\lambda = 2\pi/k_z$ and $v_p = w/k_z$.

A common problem in RF or microwave applications is that of finding the input impedance of a lossless transmission line (where $R \to 0$ and $G \to \infty$) terminated by an arbitrary load impedance Z_L. Real lines have losses. However, in most practical cases, the losses are so small that the solutions of a lossless line can be used. The circuit model of the problem is shown in Fig. 2.3. The voltage and current are given

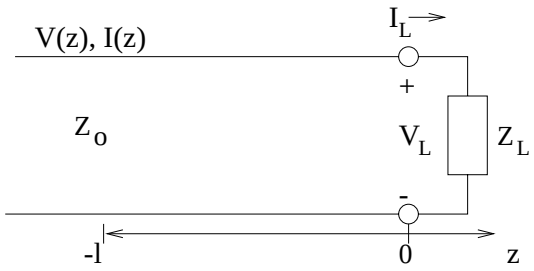

Figure 2.3: Circuit model of a terminated lossless transmission line.

by Eqs. 2.7 and 2.9 with decay constant $\alpha = 0$. At the load ($z = 0$), the load impedance is given by

$$Z_L = \frac{V(0)}{I(0)} = Z_\circ \frac{V_\circ^+ + V_\circ^-}{V_\circ^+ - V_\circ^-} \ . \tag{2.10}$$

The reflection coefficient Γ, defined as the ratio of reflected voltage amplitude to incident voltage amplitude, can be written as

$$\Gamma \equiv \frac{V_\circ^-}{V_\circ^+} = \frac{Z_L - Z_\circ}{Z_L + Z_\circ} \ . \tag{2.11}$$

For the case of a matched load, *i.e.*, $Z_L = Z_\circ$, the reflection coefficient is zero.

To find the input impedance at an arbitrary location $-l$ from the load, one has to take into account the total distance traveled by the waves. Thus, the reflection

coefficient picks up a phase factor of electrical length $2k_z l$, *i.e.*, $\Gamma(l) = |\Gamma| e^{-2ik_z l}$. The load impedance as seen at $-l$ is

$$Z_{in} = \frac{V(-l)}{I(-l)} = Z_\circ \frac{1 + \Gamma e^{-2ik_z l}}{1 - \Gamma e^{-2ik_z l}} = Z_\circ \frac{Z_L + iZ_\circ \tan k_z l}{Z_\circ + iZ_L \tan k_z l} \ . \tag{2.12}$$

Equation 2.12 can be interpreted as the input impedance for a transmission line of length l with an arbitrary load Z_L.

The power delivered to the load can be expressed in terms of the reflection coefficient. In terms of Γ, the voltage and current are given by

$$V(z) = V_\circ^+ (e^{-ik_z z} + \Gamma e^{ik_z z}) \tag{2.13}$$

and

$$I(z) = \frac{V_\circ^+}{Z_\circ} (e^{-ik_z z} - \Gamma e^{ik_z z}) \ . \tag{2.14}$$

The time average power to the load is

$$P_{av} \equiv \frac{1}{2} Re[V(z) I^*(z)] = \frac{|V_\circ^+|^2}{2Z_\circ} (1 - |\Gamma|^2) \ , \tag{2.15}$$

where Re denotes the real part of a complex quantity and I^* is the complex conjugate of I. Note that the power delivered to the load is the difference of the incident and the reflected powers as expected from energy conservation. The reflected power is proportional to $|\Gamma|^2$.

It is often necessary to compare two power levels (P_1 and P_2) in RF networks. The unit of this comparison is decibel (dB) and is defined as $10 \log(P_1/P_2)$. Absolute power is expressed in unit of dBm as $10 \log(P_1/1\ mW)$ where $P_2 = 1\ mV$.

The Smith chart is a useful graphical aid when solving transmission line problems. A sample Smith chart is shown in Fig. 2.4. The chart is essentially a polar plot of the

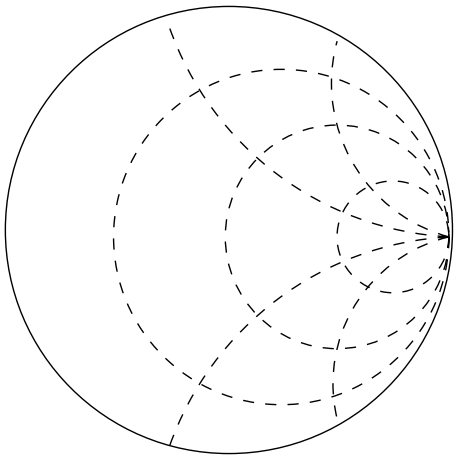

Figure 2.4: Smith chart. The center of the solid circle is the origin of the (Γ_r, Γ_i) coordinate system where Γ_r and Γ_i are the real and imaginary parts of the reflection coefficient. The solid circle has radius of one in accordance to the condition $|\Gamma| \leq 1$. The dashed circles with centers on the diameter are examples of resistance circles and the dashed circles with centers on the vertical $\Gamma_r = 1$ line (off the chart) are the reactance circles.

reflection coefficient $\Gamma = |\Gamma|e^{i\theta}$. The magnitude $|\Gamma|$ is plotted as a radius ($|\Gamma| \leq 1$) from the center of the chart, and the angle θ ($-180° \leq \theta \leq 180°$) is measured from the right-hand side of the horizontal diameter. The Smith chart is used to convert from the reflection coefficient to the normalized impedance, and vice versa. Using Eq. 2.11, the reflection coefficient is

$$\Gamma = \frac{z_L - 1}{z_L + 1} = |\Gamma|e^{i\theta} \tag{2.16}$$

where $z_L = Z_L/Z_o$ is the normalized load impedance. In terms of Γ, the normalized load impedance is

$$z_L = \frac{1 + |\Gamma|e^{i\theta}}{1 - |\Gamma|e^{i\theta}} \ . \tag{2.17}$$

Expressing Γ and z_L in real and imaginary components, *i.e.*, $\Gamma = \Gamma_r + i\Gamma_i$ and $z_L = r_L + ix_L$, Eq. 2.17 can be reduced to two real equations representing two families

of orthogonal circles in the Γ_r and Γ_i plane. The two families of circles are called the resistance circles and the reactance circles as given by

$$(\Gamma_r - \frac{r_L}{1+r_L})^2 + \Gamma_i^2 = (\frac{1}{1+r_L})^2 \tag{2.18}$$

$$(\Gamma_r - 1)^2 + (\Gamma_i - \frac{1}{x_L})^2 = (\frac{1}{x_L})^2 \tag{2.19}$$

respectively. For transmission lines that are matched to their loads (*i.e.*, $r_L = 1$), the circle has its center at $\Gamma_r = 0.5$, $\Gamma_i = 0$ and has a radius of 0.5. This circle passes through the center of the Smith chart.

2.2 Transmission Lines and Waveguides

Transmission lines and waveguides basically come in two broad types: (1) waveguides with a single closed conductor and (2) transmission lines with two or more conductors. Using Maxwell's equations in a source free region filled with a homogeneous, linear, and isotropic material (μ, ϵ), we have

$$\vec{\nabla} \times \vec{E} = -iw\mu\vec{H} \tag{2.20}$$

$$\vec{\nabla} \times \vec{H} = iw\epsilon\vec{E} \ , \tag{2.21}$$

where $\vec{E}$ and $\vec{H}$ are the spatial parts of the electric and the magnetic fields each with a common e^{iwt} time dependence. Equations 2.20 and 2.21 can be combined to yield Helmholtz wave equations for the fields,

$$\vec{\nabla}^2\vec{\phi} + k^2\vec{\phi} = 0 \ , \tag{2.22}$$

with $\vec{\phi} = \vec{E}$ or $\vec{H}$ and $k = w\sqrt{\epsilon\mu}$. Assuming the transmission lines (or waveguides) are uniform in the z-direction and the wave propagations along the z-direction ($e^{-ik_z z}$)

with propagation constant k_z, the fields can be expressed as the sum of the transverse ($\perp$) and the axial (z) field components,

$$\vec{E} = (\vec{e}_\perp + e_z\hat{z})e^{-ik_z z} \tag{2.23}$$

$$\vec{H} = (\vec{h}_\perp + h_z\hat{z})e^{-ik_z z} \ . \tag{2.24}$$

Both the transverse and the axial fields are functions of the transverse coordinates. The transverse magnetic field is related to the transverse electric field by

$$\vec{h}_\perp = \sqrt{\frac{\epsilon}{\mu}}\hat{z} \times \vec{e}_\perp \ . \tag{2.25}$$

The actual forms of the electric and the magnetic field components are determined by the materials at the boundaries of the line or the guide. The boundary conditions at the interface of media 1 to media 2 are summarized as follows

$$\hat{n} \cdot (\vec{D}_2 - \vec{D}_1) = \rho_s \tag{2.26}$$

$$\hat{n} \cdot (\vec{B}_2 - \vec{B}_1) = 0 \tag{2.27}$$

$$(\vec{E}_2 - \vec{E}_1) \times \hat{n} = \vec{M}_s \tag{2.28}$$

$$(\vec{H}_2 - \vec{H}_1) \times \hat{n} = -\vec{J}_s \ , \tag{2.29}$$

where ρ_s, $\vec{J}_s$ and $\vec{M}_s$ are the surface charge density, surface electric current and surface magnetic current, respectively; $\hat{n}$ is the unit normal vector from medium 1 to medium 2. The quantities $\vec{D}$ and $\vec{B}$ are defined by the relations $\vec{D} = \epsilon\vec{E}$ and $\vec{B} = \mu\vec{H}$ for linear media.

In microwave and RF applications, the two most common boundary conditions used are the so-called electric and magnetic boundary conditions. The electric boundary condition is the condition for a perfect conductor at a surface. Inside a perfect

conductor, all fields are zero. Assuming the perfect conductor fills all space at one side of the boundary, one has $\vec{M}_s = 0$ at the surface. Then Eq. 2.28 implies that the tangential components of the electric field are zero at the boundary, *i.e.*, $\hat{n} \times \vec{E} = 0$. The other three boundary conditions become $\hat{n} \cdot \vec{D} = \rho_s$, $\hat{n} \cdot \vec{B} = 0$ and $\hat{n} \times \vec{H} = \vec{J}_s$. The magnetic boundary condition is defined by the conditions that all fields are zero inside the conductor and that the tangential components of the magnetic field at the boundary are zero (*i.e.*, $\hat{n} \times \vec{H} = 0$). Other conditions are $\hat{n} \cdot \vec{D} = 0$, $\hat{n} \cdot \vec{B} = 0$ and $\hat{n} \times \vec{E} = -\vec{M}_s$.

2.2.1 Coaxial lines

Coaxial lines as shown in Fig. 2.5 are routinely used in low power applications. They

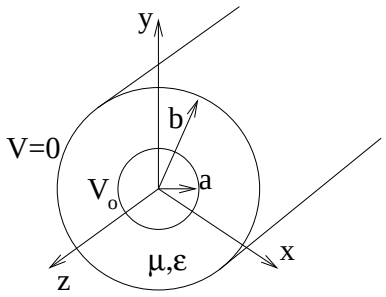

Figure 2.5: Coaxial line.

consist of two concentric conductors that are maintained at voltage levels of zero and $V_\circ$ volts. The dominant propagating mode is the TEM mode characterized by $h_z = e_z = 0$. Nontrivial solutions of the transverse electric and magnetic fields to Eqs. 2.20 and 2.21 exist for $k_z = k$. The cutoff wave number, $k_c \equiv (k^2 - k_z^2)^{1/2}$, is zero for the TEM modes. Since the curl of $\vec{e}_\perp$ is zero, $\vec{e}_\perp$ is derivable from the gradient of a scalar potential Φ. Applying the separation of variables in cylindrical coordinates

(ρ, ϕ) and the boundary conditions for the voltage in Fig. 2.5, the potential is

$$\Phi(\rho, \phi) = \frac{V_\circ}{\ln(b/a)} \ln \frac{b}{\rho} \ . \tag{2.30}$$

The sinusoidal electric and magnetic fields are

$$\vec{E} = \frac{V_\circ}{\ln(b/a)} \frac{e^{-ik_z z}}{\rho} \hat{\rho} \tag{2.31}$$

$$\vec{H} = \frac{I_\circ}{2\pi} \frac{e^{-ik_z z}}{\rho} \hat{\phi} \ , \tag{2.32}$$

where $I_\circ$ is the current amplitude.

2.2.2 Rectangular Waveguides

In accelerator applications, the rectangular and the circular waveguides are commonly used for high power transmissions between the power sources and the accelerating structures. This is because of their high power handling capability and low loss. There are two basic types of propagating modes in the waveguides: (1) TE modes and (2) TM modes. The TE modes are characterized by the conditions that $E_z = 0$ and $H_z \neq 0$, while the TM modes by $H_z = 0$ and $E_z \neq 0$.

The drawing of a rectangular waveguide is shown in Fig. 2.6. For TE waves trav-

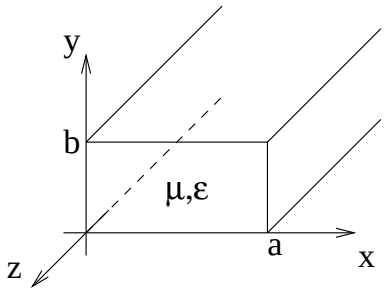

Figure 2.6: Rectangular waveguide.

eling along the z-direction, the longitudinal component of the magnetic field satisfies the wave equation

$$(\nabla_\perp^2 + k_c^2) h_z(x,y) = 0 \ , \tag{2.33}$$

where $k_c^2 = k^2 - k_z^2$ and $\nabla_\perp^2$ is the Laplacian in the transverse coordinates (x, y). The solution to Eq. 2.33 is

$$h_z = (A\cos k_x x + B \sin k_x x)(C \cos k_y y + D \sin k_y y) \ , \tag{2.34}$$

where A, B, C and D are constants, k_x and k_y are wave numbers in the x and y directions, to be determined by boundary conditions. Applying the electric boundary conditions, $e_x = 0$ at $y = 0$ and b, and $e_y = 0$ at $x = 0$ and a to the electric fields (found using Eqs. 2.20 and 2.21), the z-component of the magnetic field becomes

$$H_z(x,y,z) = h_z e^{-ik_z z} = A_{mn} \cos(k_x x) \cos(k_y y) e^{-ik_z z} \ , \tag{2.35}$$

where $k_x = m\pi/a$, $m = 0, 1, 2 \ldots$ and $k_y = n\pi/b$, $n = 0, 1, 2 \ldots$. The constant A_{mn} is the field amplitude and the propagation constant $k_z = \sqrt{k^2 - (m\pi/a)^2 - (n\pi/b)^2}$. In order to have propagating modes, the condition $k > k_c = \sqrt{(m\pi/a)^2 + (n\pi/b)^2}$ must be met. For $k < k_c$, the modes are called cutoff or evanescent and decay exponentially along the waveguide. Thus, each TE_{mn} mode has a cutoff frequency, below which it can't propagate, defined by $f_{c,mn} = (2\pi\sqrt{\mu\epsilon})^{-1}\sqrt{(m\pi/a)^2 + (n\pi/b)^2}$. The various field components, obtained from Maxwell's equations using H_z, are

$$E_x = A_{mn} \frac{iw\mu\pi n}{k_c^2 b} \cos(k_x x) \sin(k_y y) e^{-ik_z z} \tag{2.36}$$

$$E_y = A_{mn} \frac{-iw\mu\pi m}{k_c^2 a} \sin(k_x x) \cos(k_y y) e^{-ik_z z} \tag{2.37}$$

$$H_x = A_{mn}\frac{ik_z\pi m}{k_c^2 a}\sin(k_x x)\cos(k_y y)e^{-ik_z z} \tag{2.38}$$

$$H_y = A_{mn}\frac{ik_z\pi n}{k_c^2 b}\cos(k_x x)\sin(k_y y)e^{-ik_z z}\ . \tag{2.39}$$

For $a > b$, the lowest propagating mode is TE_{10}. There is a frequency interval (called the passband) between this and the next lowest mode in which only the TE_{10} mode can propagate.

The power flow in the waveguide for the TE_{mn} mode is

$$P_{mn} = \frac{1}{2}Re\int_s \vec{E}\times\vec{H}^*\cdot\hat{z}\ ds\ , \tag{2.40}$$

where the integration is taken over the cross section s of the waveguide. Along the waveguide, the power loss per unit length due to the resistive loss in the conductor is

$$P_l = \frac{R_s}{2}\int_c |\vec{J}_s|^2 dl, \tag{2.41}$$

where R_s is the surface resistivity[1], $\vec{J}_s = \hat{n}\times\vec{H}$, and c is the path around the perimeter of the waveguide cross section. The attenuation due to conductor loss is characterized by the attenuation constant $\alpha_c = P_l/(2P_{mn})$ in units of neper[2] per meter.

For TM modes, the longitudinal component of the electric field satisfies the following equation:

$$(\nabla_\perp^2 + k_c^2)e_z(x,y) = 0\ . \tag{2.42}$$

Since the wave equation is the same as that of the TE modes, the derivation of the solution follows similar treatment. The solution is

$$e_z(x,y) = (A\cos k_x x + B\sin k_x x)(C\cos k_y y + D\sin k_y y)\ . \tag{2.43}$$

[1]Note that the surface resistivity is related to the conductivity σ by the relation $R_s = (\sigma\delta_s)^{-1}$, where δ_s is the skin depth.

[2]The conversion of α_c to decibel per meter (dB/m) is $\alpha_{c,dB} = 20\alpha_c\log_{10} e$.

Applying the electric boundary conditions, $e_z = 0$ at $x = 0$ and a, and at $y = 0$ and b, yields

$$E_z(x, y, z) = B_{mn} \sin(k_x x) \sin(k_y y) e^{-ik_z z} \ , \tag{2.44}$$

with $k_x = m\pi/a$, $m = 1, 2, 3 \ldots$ and $k_y = n\pi/a$, $n = 1, 2, 3 \ldots$ and B_{mn} is the field amplitude. Using Maxwell's equations, the transverse field components are

$$\begin{aligned}
E_x &= \frac{-ik_z \pi m}{a k_c^2} B_{mn} \cos(k_x x) \sin(k_y y) e^{-ik_z z} && (2.45)\\
E_y &= \frac{-ik_z \pi n}{b k_c^2} B_{mn} \sin(k_x x) \cos(k_y y) e^{-ik_z z} && (2.46)\\
H_x &= \frac{iw\epsilon \pi n}{b k_c^2} B_{mn} \sin(k_x x) \cos(k_y y) e^{-ik_z z} && (2.47)\\
H_y &= \frac{-iw\epsilon \pi m}{a k_c^2} B_{mn} \cos(k_x x) \sin(k_y y) e^{-ik_z z} && (2.48)
\end{aligned}$$

with propagation constant $k_z = \sqrt{k^2 - (m\pi/a)^2 - (n\pi/b)^2}$. The cutoff frequency of the TM_{mn} mode is $f_{c,mn} = (2\pi\sqrt{\mu\epsilon})^{-1}\sqrt{(m\pi/a)^2 + (n\pi/b)^2}$. The first propagating TM mode is the TM_{11}. In a rectangular waveguide, the TM_{mn} modes are degenerate with the TE_{mn} modes. However, there can't be TM_{m0} or TM_{0n} modes.

2.2.3 Circular Waveguides

The geometry for a circular waveguide is shown in Fig. 2.7. The traveling wave

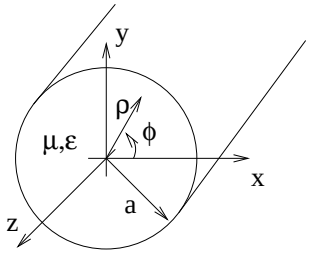

Figure 2.7: Circular waveguide.

solutions for such a waveguide are obtained by solving Helmholtz wave equation in cylindrical coordinates (ρ, ϕ, z). For the TE modes, the wave equation is

$$(\frac{\partial^2}{\partial\rho^2} + \frac{1}{\rho}\frac{\partial}{\partial\rho} + \frac{1}{\rho^2}\frac{\partial^2}{\partial\phi^2} + k_c^2)h_z(\rho,\phi) = 0 \ , \tag{2.49}$$

with $k_c^2 = k^2 - k_z^2$. The solution is

$$h_z = (A\sin n\phi + B\cos n\phi)[CJ_n(k_c\rho) + DY_n(k_c\rho)] \ , \tag{2.50}$$

where A, B, C and D are constants; J_n and Y_n are the Bessel functions of the first and second kinds, respectively. In order to have single-valued solutions azimuthally, $n = 0, 1, 2 \ldots$. At the origin ($\rho = 0$), $Y_n = \infty$. Hence, to have finite solutions at the origin, the constant D must be zero. Then the longitudinal component of the magnetic field becomes

$$H_z(\rho,\phi,z) = h_z e^{-ik_z z} = (A\sin n\phi + B\cos n\phi)J_n(k_c\rho)e^{-ik_z z} \ . \tag{2.51}$$

The other constants are found by applying the electric boundary condition, $E_\phi = 0$ at $\rho = a$. The azimuthal component of the electric field becomes

$$E_\phi(\rho,\phi,z) = \frac{iw\mu}{k_c}(A\sin n\phi + B\cos n\phi)J_n^{'}(k_c\rho)e^{-ik_z z} \ , \tag{2.52}$$

where $J_n^{'}$ is the first derivative of J_n. $E_\phi = 0$ at $\rho = a$ if $k_c = P_{nm}^{'}/a$ where $P_{nm}^{'}$ is the mth root of $J_n^{'}$. The propagation constant for the TE_{nm} mode is $k_z = \sqrt{k^2 - (P_{nm}^{'}/a)^2}$, and the cutoff frequency is $f_{c,nm} = P_{nm}^{'}/(2\pi a\sqrt{\mu\epsilon})$. The other transverse field components are

$$E_\rho \ = \ \frac{-iw\mu n}{k_c^2\rho}(A\cos n\phi - B\sin n\phi)J_n(k_c\rho)e^{-ik_z z} \tag{2.53}$$

$$H_\rho = \frac{-ik_z}{k_c}(A\sin n\phi + B\cos n\phi)J_n'(k_c\rho)e^{-ik_z z} \quad (2.54)$$

$$H_\phi = \frac{-ik_z n}{k_c^2\rho}(A\cos n\phi - B\sin n\phi)J_n(k_c\rho)e^{-ik_z z}\ , \quad (2.55)$$

where A and B are determined by the excitation of the waveguide. The lowest propagating mode is the TE_{11} mode.

In the case of the TM modes, the longitudinal component of the electric field satisfies the same wave equation as the TE modes. The solution is

$$E_z(\rho,\phi,z) = (A\sin n\phi + B\cos n\phi)J_n(k_c\rho)e^{-ik_z z}\ , \quad (2.56)$$

with $n = 0, 1, 2\ldots$. Applying the electric boundary condition, $E_z = 0$ at $\rho = a$, gives $k_c = P_{nm}/a$ where P_{nm} is the mth root of J_n. For the TM_{nm} mode, the propagation constant is $k_z = \sqrt{k^2 - (P_{nm}/a)^2}$ with a cutoff frequency $f_{c,nm} = P_{nm}/(2\pi a\sqrt{\mu\epsilon})$. The transverse field components are

$$E_\rho = \frac{-ik_z}{k_c}(A\sin n\phi + B\cos n\phi)J_n'(k_c\rho)e^{-ik_z z} \quad (2.57)$$

$$E_\phi = \frac{-ik_z n}{k_c^2\rho}(A\cos n\phi - B\sin n\phi)J_n(k_c\rho)e^{-ik_z z} \quad (2.58)$$

$$H_\rho = \frac{iw\epsilon n}{k_c^2\rho}(A\cos n\phi - B\sin n\phi)J_n(k_c\rho)e^{-ik_z z} \quad (2.59)$$

$$H_\phi = \frac{-iw\epsilon}{k_c}(A\sin n\phi + B\cos n\phi)J_n'(k_c\rho)e^{-ik_z z}\ , \quad (2.60)$$

where A and B are determined by the source of the excitation. The first propagating TM mode is the TM_{01} mode.

2.3 RF Cavities with Cylindrical Symmetry

In linear accelerators, the accelerating structures usually have cylindrical symmetry. The simplest type of cavity with cylindrical symmetry is the pill-box cavity, which

is basically a small section of a circular waveguide closed at both ends by a conductor.The geometry of such a cavity is shown in Fig. 2.8. Since the cells of many linac

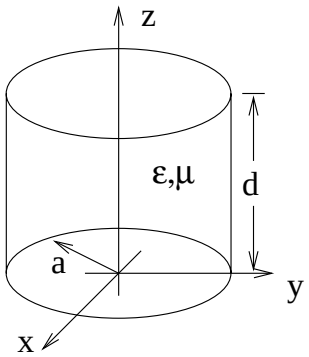

Figure 2.8: Pill-box cavity.

structures resemble a pill box, it is expedient to obtain the analytical solutions of the pill-box cavity. The solutions can be used to estimate various RF parameters such as the cavity size for a given operating frequency, or to simulate RF cavities in beam transport codes.

The solution of the pill-box cavity is obtained from that of the circular waveguide by imposing additional boundary conditions at the closed ends. The need for axial electric field (E_z) for beam acceleration means that only the TM modes are of interest. From the circular waveguide solutions, one can construct standing wave solutions of the transverse electric fields as

$$\vec{E}_\perp(\rho,\phi,z) = \vec{e}(\rho,\phi)[A^+ e^{-ik_z z} + A^- e^{ik_z z}] \ , \tag{2.61}$$

where $\vec{E}_\perp = E_\rho$ or E_ϕ; A^+ and A^- are the wave amplitudes in the forward direction ($+z$) and the backward direction ($-z$), respectively. $\vec{e}(\rho,\phi)$ represents the dependence on the transverse coordinates, which are the same functions as those of the circular

waveguide solutions. Applying the boundary conditions $\vec{E}_\perp = 0$ at $z = 0$ and d, imply that $A^+ = -A^-$ and $-2iA^+ \sin(k_z d) = 0$. Then $k_z d = l\pi$ for $l = 0, 1, 2 \ldots$. This means that the cavity must be an integer multiple of half-guide wavelength long. The resonant frequency of the TM_{nml} mode is

$$f_{nml} = \frac{c}{2\pi\sqrt{\mu\epsilon}} \sqrt{\left(\frac{P_{nm}}{a}\right)^2 + \left(\frac{l\pi}{d}\right)^2} \ . \tag{2.62}$$

The field components are summarized as follows,

$$\begin{aligned}
E_z &= (A_{nm} \sin n\phi + B_{nm} \cos n\phi) J_n(k_c\rho) \cos(k_z z) && (2.63)\\
E_\rho &= \frac{-k_z}{k_c} (A_{nm} \sin n\phi + B_{nm} \cos n\phi) J_n^{'}(k_c\rho) \sin(k_z z) && (2.64)\\
E_\phi &= \frac{-k_z n}{k_c^2 \rho} (A_{nm} \cos n\phi - B_{nm} \sin n\phi) J_n(k_c\rho) \sin(k_z z) && (2.65)\\
H_\rho &= \frac{iw\epsilon n}{k_c^2 \rho} (A_{nm} \cos n\phi - B_{nm} \sin n\phi) J_n(k_c\rho) \cos(k_z z) && (2.66)\\
H_\phi &= \frac{-iw\epsilon}{k_c} (A_{nm} \sin n\phi + B_{nm} \cos n\phi) J_n^{'}(k_c\rho) \cos(k_z z) \ , && (2.67)
\end{aligned}$$

where $k_c = P_{nm}/a$ for $n = 0, 1, 2 \ldots$ and $m = 1, 2, 3 \ldots$, and $k_z = l\pi/d$. The constants A_{nm} and B_{nm} are determined by the excitation source.

The first TM mode is the TM_{010} with resonant frequency $f_{010} = 2.405c/(2\pi a\sqrt{\mu\epsilon})$. The field components are

$$\begin{aligned}
E_z &= E_\circ J_0(\frac{2.405}{a}\rho) && (2.68)\\
H_\phi &= -icE_\circ \sqrt{\frac{\epsilon}{\mu}} J_1(\frac{2.405}{a}\rho) \ , && (2.69)
\end{aligned}$$

where $E_\circ$ is the field amplitude. ($J_1 = J_0^{'}$.) As seen from the field equation, the TM_{010} mode has strong electric field on the axis because J_0 is the maximum on the

axis[3]. This kind of field configuration is ideally suited for beam acceleration. Thus, the individual cells of accelerating structures usually operate in the TM_{010} mode.

In general, single-cell accelerating cavities have several designations. First, they are broadly characterized as TM_{nml} and TE_{nml} modes, where the indices n, m, and l are associated with the azimuthal, radial and axial degrees of freedom, respectively. Second, the cavity modes are labeled as monopole ($n = 0$), dipole ($n = 1$), quadrupole ($n = 2$), *etc.*, according to their degrees of azimuthal variation.

Multi-cell cavities have one additional designation associated with the total number of cells (the additional longitudinal degree of freedom). When N number of single-cell cavities are coupled together, each mode in the single-cell cavity is split into N modes. The band of N modes is called the passband of the corresponding single-cell cavity mode. This is analogous to the case of one dimensional harmonic oscillator where a system of one oscillator has one oscillation state, two coupled oscillators have two (normal) states and so on. Multi-cell accelerating cavities usually operate in one of the passband modes of the TM monopole mode (TM_{010}).

2.4 Equivalent Circuit of RF Cavities

The characteristics of RF cavities can be modeled as lumped-element resonant circuits. At a particular frequency, a RF cavity can be modeled by either a parallel or a series RLC circuit. For the following analysis, the parallel RLC circuit as shown in Fig. 2.9 is used. In the model, the capacitance C and the inductance L are the

[3]The azimuthal magnetic field provides some beam focusing in principle, but the effect is small because J_1 decreases to zero on the axis where the beam primarily is.

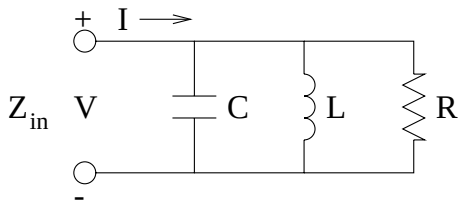

Figure 2.9: A parallel RLC circuit model of the RF cavity.

electric and the magnetic energy storage elements, respectively. The resistance R represents the power loss in the circuit. For a sinusoidal excitation source (e^{iwt}), the input impedance is

$$Z_{in} = \left(\frac{1}{R} + \frac{1}{iwL} + iwC\right)^{-1} \ . \tag{2.70}$$

The complex power delivered to the resonant circuit is

$$P_{in} = \frac{1}{2}VI^* = \frac{|V|^2}{2Z_{in}^*} = \frac{|V|^2}{2}(\frac{1}{R} + \frac{i}{wL} - iwC) \ , \tag{2.71}$$

where V is the voltage across the terminal and I^* is the complex conjugate of the input current. The individual terms of the input power are identified as the power loss $P_{loss} = |V|^2/(2R)$, the time averaged electric stored energy $U_e = |V|^2C/4$, and the time averaged magnetic stored energy $U_m = |V|^2/(4w^2L)$. Thus, the input power becomes $P_{in} = P_{loss} + 2iw(U_m - U_e)$. At resonance, the magnetic energy equals the electric energy, and the input impedance is purely resistive, *i.e.*, $Z_{in} = R$. The resonant frequency for the equivalent circuit is $w_\circ = 1/\sqrt{LC}$.

The parameter that characterizes the performance of the resonant circuit is the quality factor which is defined as

$$Q = w\frac{U_T}{P_{loss}} = w\frac{U_m + U_e}{P_{loss}} \ , \tag{2.72}$$

where U_T is total average stored energy. At resonance, the quality factor becomes

$$Q_\circ = w_\circ \frac{2U_m}{P_{loss}} = \frac{R}{w_\circ L} = w_\circ RC \ . \tag{2.73}$$

The behavior of the input impedance near resonance can be studied by letting $w = w_\circ + \Delta w$. In the vicinity of resonance, the input impedance (Eq. 2.70) becomes

$$Z_{in} \approx \frac{R}{1 + i2Q_\circ \Delta w / w_\circ} \ . \tag{2.74}$$

Equation 2.74 gives the typical resonance curve of a resonant circuit that peaks at $w_\circ$ with $|Z_{in}| = R$. When $|Z_{in}|$ has fallen to 0.707 of its maximum value, its phase is 45° if $w < w_\circ$ and -45° if $w > w_\circ$. From Eq. 2.74, we have $Q_\circ = w_\circ/(2\Delta w)$. This relation shows that the quality factor can be interpreted as a measure of the sharpness of the resonance. It provides a means of measuring the quality factor.

2.5 External Coupling of RF Cavities

In practical situations, a RF cavity is coupled to some external load (or power source such as a klystron). The means of coupling could be an aperture, an electric probe, or a magnetic loop. To describe the effect of loading, a parameter called the loaded quality factor is defined as

$$Q_L = w_\circ \frac{U_T}{P_T} \ , \tag{2.75}$$

where $P_T = P_c + P_e$ represents the total power loss in the system, P_c is the ohmic loss at the cavity wall and P_e is the power flowing out of the cavity through the coupler. Substituting the total power loss into Eq. 2.75, one can define the unloaded and the

external quality factors as

$$Q_\circ = w_\circ \frac{U_T}{P_c} \tag{2.76}$$

$$Q_e = w_\circ \frac{U_T}{P_e} \ , \tag{2.77}$$

respectively. $Q_\circ$ characterizes the intrinsic performance of the cavity, while Q_e describes its external interaction without internal loss. With these definitions, Eq. 2.75 becomes

$$\frac{1}{Q_L} = \frac{1}{Q_\circ} + \frac{1}{Q_e} \ . \tag{2.78}$$

The strength of the external coupling is quantified by the coupling coefficient β,

$$\beta = \frac{Q_\circ}{Q_e} = \frac{P_e}{P_c} \ . \tag{2.79}$$

The external coupling of a cavity is characterized by the following set of β values,

$$\begin{aligned} \beta &> 1 \quad \text{overcouple} \\ \beta &= 1 \quad \text{critical coupling} \\ \beta &< 1 \quad \text{undercouple} \ . \end{aligned}$$

For cavity testing in the absence of external beam, impedance matching between the cavity and the external load requires that the reflection coefficient be zero (*i.e.*, no power reflection from the cavity). Thus, the matching condition is that the input power (P_e) to the cavity equals the power loss in the cavity (P_c). However, when there is external beam loading, the cavity needs to be overcoupled to account for the additional power loss to the beam. The matching condition for a beam-loaded cavity is

$$\beta = 1 + \frac{P_b}{P_c} \ , \tag{2.80}$$

where P_b is the power loss to the beam. The loaded quality factor can be expressed in terms of β using Eq. 2.79, *i.e.*,

$$Q_L = \frac{Q_\circ}{1+\beta} \ . \tag{2.81}$$

The effect of external loading is the reduction of the unloaded quality factor of the system.

2.5.1 Cavity Decay

When the excitation source of a RF cavity is off or removed, the energy in the system decays due to ohmic loss or power leakage through the coupler. Because of energy conservation, the rate of energy decay equals the decrease in the total power of the cavity,

$$\frac{dU_T}{dt} = -P_T = -w\frac{U_T}{Q_L} \ . \tag{2.82}$$

The solution is

$$U_T = U_\circ e^{-\frac{t}{\tau_L}}, \tag{2.83}$$

where $U_\circ$ is the initial energy and $\tau_L = Q_L/w$ is the decay time constant. Experimentally, the loaded quality factor can be determined by measuring the time constant from the cavity decay.

2.5.2 Driven Cavity with a Coupler

The steady state behavior of a driven cavity can be analyzed by the equivalent circuit shown in Fig. 2.10. The generator is represented by an ideal current source with an

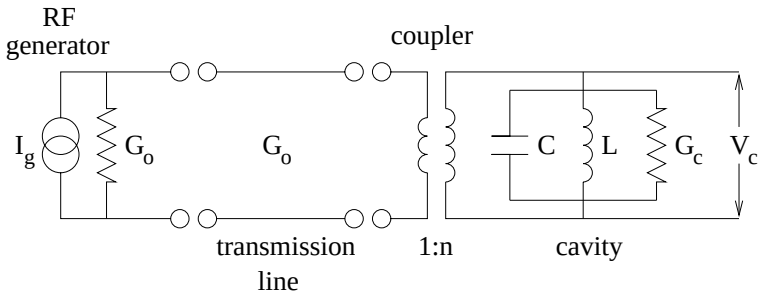

Figure 2.10: Equivalent circuit model of a driven RF cavity.

admittance of $G_\circ$[4]. Matching is assumed between the generator and the transmission line; hence they have the same admittance. In order to match the transmission line to a cavity of arbitrary impedance, the coupler is modeled by a step-up transformer with a transformer ratio of n. With a voltage V_c across the cavity, the total stored energy and the dissipated power have the usual expressions of $U_T = CV_c^2/2$ and $P_c = G_c V_c^2/2$. Then the unloaded quality factor is $Q_\circ = G_c^{-1}\sqrt{C/L}$. Assuming the transmission line is connected to the coupler, the power loss through the coupler as seen from the cavity is $P_e = G_\circ V_c^2/(2n^2)$. Note that $G_\circ/n^2$ is the admittance transformation by the transformer. This yields an external quality factor of $Q_e = (n^2/G_\circ)\sqrt{C/L}$. The coupling coefficient is $\beta = G_\circ/(n^2 G_c)$.

In practice, the reflection coefficient is measured directly instead of the coupling coefficient. Therefore, it is important to relate the two quantities. Using Eq. 2.11, the reflection coefficient of the cavity-coupler system is

$$\Gamma = \frac{1 - Y_c/G_\circ}{1 + Y_c/G_\circ} \ , \tag{2.84}$$

[4]The admittance defined as the inverse of the impedance, is introduced for the convenience of adding impedances in a parallel circuit.

where Y_c is the input admittance. The normalized input admittance $Y_c/G_\circ$ is found by summing all the admittances in the parallel RLC circuit and then multiply throughout by the square of the transformer ratio. The result is

$$\frac{Y_c}{G_\circ} = \frac{n^2 G_c}{G_\circ} + i\frac{n^2}{G_\circ}\sqrt{\frac{C}{L}}(\frac{w}{w_\circ} - \frac{w_\circ}{w}) = \frac{1}{\beta} + iQ_e(\frac{w}{w_\circ} - \frac{w_\circ}{w}) \ , \tag{2.85}$$

where w is the generator frequency and $w_\circ$ is the resonant frequency of the cavity. Substituting Eq. 2.85 into Eq. 2.84 gives

$$\Gamma(w) = \frac{\beta - 1 - iQ_\circ(w/w_\circ - w_\circ/w)}{\beta + 1 + iQ_\circ(w/w_\circ - w_\circ/w)} \ . \tag{2.86}$$

At resonance, the reflection coefficient becomes

$$\Gamma = \frac{\beta - 1}{\beta + 1} \ . \tag{2.87}$$

Applying energy conservation, the input power to the cavity is

$$P_{in} = P_f(1 - |\Gamma|^2) = \frac{4P_f}{Q_e Q_\circ[(1/Q_\circ + 1/Q_e)^2 + (w/w_\circ - w_\circ/w)^2]} \ , \tag{2.88}$$

where P_f is the forward power from the generator and $P_f|\Gamma|^2$ is the reflected power at the coupler.

2.6 Linear Accelerating Structures

There are two basic types of linear accelerating structures: (1) standing wave structures and (2) traveling wave structures. In a standing wave structure, the electromagnetic wave enters the structure through an input coupler and reflects off the ends of the structure to form standing wave pattern. On the other hand, the electromagnetic wave in a traveling wave structure propagates down the structure and exit through an output coupler to an external load.

2.6.1 Acceleration and RF Parameters

The acceleration of charged particle beams required two conditions: (1) an electric field component in the direction of particle motion and (2) the synchronization of the beam with the accelerating field[5]. For the following discussion, particle motion is assumed on axis and in the z-direction. The electric field for traveling wave structure is

$$E_z(z,t) = E(z)cos(wt - \int_0^z k(z')dz' + \phi_s) \ , \tag{2.89}$$

where $E(z)$ is the on-axis field, $k(z) = w/v_p(z)$, v_p is the phase velocity of the wave and ϕ_s is an arbitrary phase. For the standing wave structure, the electric field is

$$E_z(z,t) = E(z)cos(wt + \phi_s) \ . \tag{2.90}$$

In order to have synchronized acceleration, the particle velocity must equals the phase velocity of the wave. The particle that satisfies such a condition is called the synchronous particle. The force experienced by the synchronous particle is $F_z = qE(z)\cos\phi_s$, where ϕ_s is called the synchronous phase. The synchronous phase is defined with respect to the crest of the electric field as shown in Fig. 2.11. It describes the position of the synchronous particle relative to the RF field.

The energy gain of an on-axis particle in the RF field is computed by considering its passage through a gap as illustrated in Fig. 2.12. The energy gain is

$$\Delta U = q\int_{-L/2}^{L/2} E(z)\cos[wt(z) + \phi_s]dz = qV_\circ T\cos\phi_s \ , \tag{2.91}$$

[5]The second condition is important for providing consistent energy transfer from the electric field to the beam.

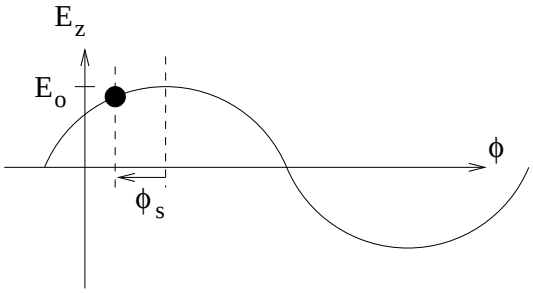

Figure 2.11: Phase relationship of the synchronous particle with respect to the electric field.

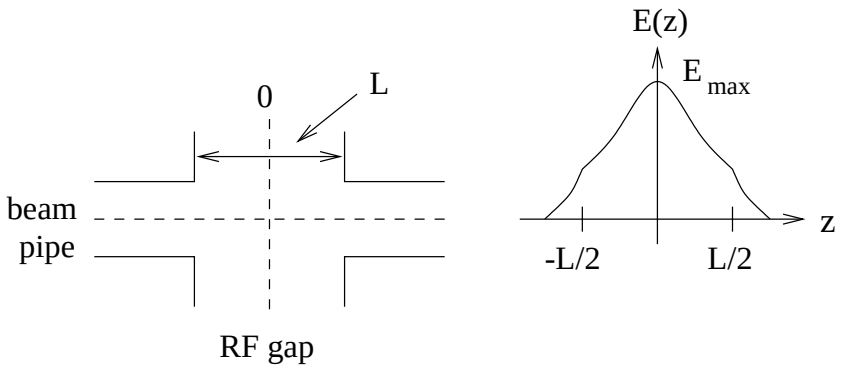

Figure 2.12: An accelerating RF gap and its on-axis electric field. The electrical center of the field is assumed to be coincided with the geometrical center of the gap.

where

$$V_\circ = \int_{-L/2}^{L/2} E(z)dz \tag{2.92}$$

and

$$T = \frac{\int_{-L/2}^{L/2} E(z)\cos[wt(z)]dz}{\int_{-L/2}^{L/2} E(z)dz} \ . \tag{2.93}$$

The quantity T is called the transit time factor, which is the fraction of the maximum energy gained by the particle due to the sinusoidal time variation of the field. The average accelerating gradient is defined as $E_\circ = V_\circ/L$.

The performance of a RF cavity is characterized by several parameters (figures of

merit). The first is the unloaded quality factor defined in previous section. The next parameter is the shunt impedance

$$R_s = \frac{V_\circ^2}{P_{loss}} \ , \tag{2.94}$$

where P_{loss} is the power loss at the cavity wall. For a given amount of input power, a high shunt impedance cavity produces more accelerating voltage per unit power loss. In other word, R_s characterizes the cavity's efficiency in converting available RF power to the accelerating field. To take into account the transit time factor effect, the effective shunt impedance is defined as $r_s = T^2 R_s$. For linac application, the shunt impedance per unit length is often used,

$$Z_s = \frac{R_s}{L} \text{ or } \frac{r_s}{L} \ , \tag{2.95}$$

where L is the total length of the accelerating structure. Another figure of merit is the ratio of effective shunt impedance over the quality factor,

$$\frac{r_s}{Q_\circ} = \frac{(V_\circ T)^2}{w_\circ U_T} \ , \tag{2.96}$$

which depends only on the cavity geometry. This parameter is useful for comparing the RF performance of cavities of different shapes, independent of their sizes.

In the design of an accelerating structure for a particular application, the first and the most important parameter to decide on is the operating frequency. Both beam dynamic and RF issues such as wake field effect, dynamic aperture, available power source, *etc.*, are considered in choosing the operating frequency. It is important to know the impacts of the frequency choice on the various RF parameters. Therefore, it is useful to know the scaling of various RF parameters with respect to the frequency.

The frequency scaling of the cavity size can be obtained from Helmholtz wave equation. By scaling all linear dimensions (x, y, z) by a constant factor c, Helmholtz equation becomes

$$[\frac{\partial^2}{\partial(cx)^2} + \frac{\partial^2}{\partial(cy)^2} + \frac{\gamma^2}{c^2}]\psi(c\vec{x}) = 0 \ , \tag{2.97}$$

where $\vec{x} = (x, y, z)$ and γ is the eigenvalue. With the definitions $\vec{X} = c\vec{x}$ and $\Gamma = \gamma/c$, Eq. 2.97 becomes

$$[\frac{\partial^2}{\partial X^2} + \frac{\partial^2}{\partial Y^2} + \Gamma^2]\psi(\vec{X}) = 0 \ . \tag{2.98}$$

As one can see, the field remains unchanged, while the eigenvalue is altered by a factor of $1/c$. Hence the cavity size scales inversely with the frequency, *i.e.*,

$$c \propto 1/f \ . \tag{2.99}$$

The scalings of the shunt impedance and the quality factor with frequency can be calculated in a similar manner. Since the total stored energy (U_T) in the cavity is a volume integral of the field square, $U_T \propto c^3$. The power loss (P_l) in the cavity wall is proportional to the product of the surface resistance with the surface integral of the square of the magnetic field. Therefore, the power loss is proportional to $f^{1/2}c^2$. The accelerating voltage (V) is the line integral of the electric field, so it is proportional to c. Using the scalings of U_T, P_l, and V, the frequency scalings of R_s and $Q_\circ$ are

$$R_s \ \propto \ f^{-1/2} \tag{2.100}$$

$$Q \ \propto \ f^{-1/2} \ . \tag{2.101}$$

The shunt impedance per unit length Z_s is proportional to $f^{1/2}$.

2.6.2 Characteristic of Periodic Structures

Linear accelerating structures are often consisted of a periodic array of coupled cells. Therefore, it is useful to study the characteristic of a periodic structure. A periodic accelerating structure can be pictured as a chain of coupled electromagnetic oscillators and analyzed using an equivalent circuit model. This approach provides a quantitative description of the dispersion relation. The circuit model representing a periodic array of identical cells is shown in Fig. 2.13. The variables I_n and V_n are the equivalent

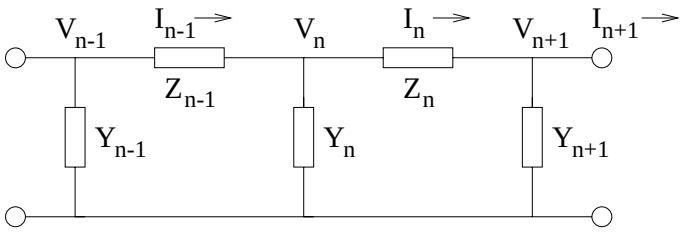

Figure 2.13: Equivalent circuit model of a periodic chain of identical electromagnetic oscillators. Each oscillator is represented by a series impedance (Z) and a shunt admittance (Y).

current and voltage in cell n, respectively. For identical cells, all series impedances are equal and likewise for all shunt admittances. Applying Kirchhoff's rule to the circuit model gives

$$I_{n-1} - I_n = YV_n \tag{2.102}$$

$$I_n - I_{n+1} = YV_{n+1} \tag{2.103}$$

$$V_n - V_{n+1} = ZI_n \ . \tag{2.104}$$

Substituting Eqs. 2.102 and 2.103 into Eq. 2.104 yields

$$\frac{I_{n-1}}{Y} - I_n(Z + \frac{2}{Y}) + \frac{I_{n+1}}{Y} = 0 \ . \tag{2.105}$$

Let d be the periodic length of the structure, k_z be the propagating constant, and $\phi = k_z d$ be the phase advance per cell. Floquet theorem [10] implies that

$$I_n = I_{n-1} e^{-i\phi} \tag{2.106}$$

$$I_{n+1} = I_n e^{-i\phi} \ . \tag{2.107}$$

Eliminating I_{n-1} and I_{n+1} in Eq. 2.105 gives

$$I_n [\frac{e^{i\phi}}{Y} - (Z + \frac{2}{Y}) + \frac{e^{-i\phi}}{Y}] = 0 \ . \tag{2.108}$$

In order to have nontrivial solutions to Eq. 2.108, the term in the bracket must equals zero, yielding the condition

$$\cos\phi(k) = 1 + \frac{YZ}{2} \ , \tag{2.109}$$

where Y and Z are functions of frequency in general. Equation 2.109 provides the dispersion relation which relates the frequency to the phase advance per cell for a particular choices of Z and Y. Since $\cos\phi$ obeys $-1 \leq \cos\phi \leq 1$, the phase advance per cell (ϕ) of a cavity operating mode lies between zero and π.

As an example for the application of Eq. 2.109, consider a periodic array of accelerating cells in a cavity that are coupled through irises in the region of the cavity axis. The cavity can be modeled as a series of electrically coupled LC circuits. Electrical couplings are used because the coupling irises are in strong electric field regions. The equivalent circuit model of a basic cell is shown in Fig. 2.14. The coupling element is represented by a shunt capacitance C_k. The equivalent series impedance is

$$Z = iwL + \frac{1}{iwC} = iwL(1 - \frac{w_\circ^2}{w^2}) \ , \tag{2.110}$$

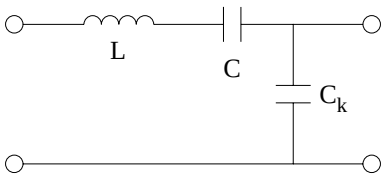

Figure 2.14: Equivalent circuit model of a basic cell of a periodic array of electrically coupled accelerating cells.

where $w_\circ^2 = 1/(LC)$ is the resonant frequency. The equivalent shunt admittance is iwC_k. Substituting the equivalent series impedance and shunt admittance into Eq. 2.109 gives

$$w = w_\circ \sqrt{2(\frac{C}{C_k})(1-\cos\phi)+1}\ . \tag{2.111}$$

The dispersion relation is plotted in Fig. 2.15. The region of $0 \leq \phi \leq \pi$ is called

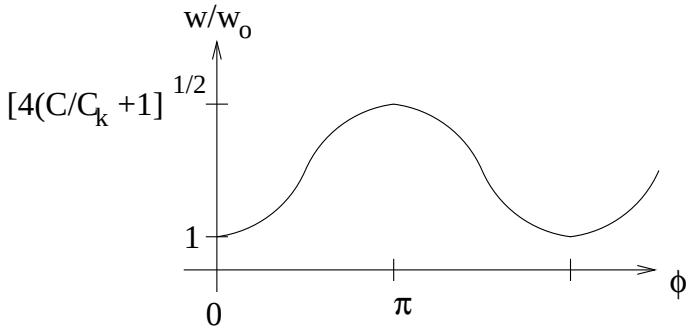

Figure 2.15: Dispersion relation of a periodic array of electrically coupled accelerating cells.

the passband of the TM_{010} mode. According to the plot (Fig. 2.15), the π mode lies higher than the zero mode for electrically coupled cells.

Chapter 3

Design of the 805 MHz RF Cavity

The RF cavity of the MUCOOL experiment that was designed, built and tested at Fermilab has three major components: the accelerating cavity, the high power RF coupler and the waveguide section for impedance matching. The power source for the cavity is a spare 805 MHz klystron from the past Fermilab linac upgrade. The cavity is a π mode standing wave structure with multiple cells and open irises. The RF coupler is a rectangular aperture located at the outer wall of an end cell of the cavity. The function of the coupler is to provide impedance matching (zero reflection) for maximum energy transmission to the cavity. Due to the engineering constraints in the design of the muon cooling channel, the standard rectangular waveguide (WR 975) that transfers the energy to the cavity from the klystron can't extend into the coupler. Instead, a waveguide of smaller dimensions must be used in the superconducting solenoid region that encloses the cavity. Since the exterior waveguide and the one in the solenoid region have different characteristic impedances, a special waveguide section is needed to match the impedances. The cavity design was simulated with the programs Mafia [11] and Superfish [12], while the RF coupler and the waveguide

transition piece were designed with Mafia. Only the design work that was done with Mafia is shown in this chapter.

3.1 RF Cavity

In the baseline cooling scenario of the muon collider, RF cavities with an average accelerating gradient of 30 MV/m or more are required to maintain an average muon momentum of 186 MeV/c. The operating frequency of the cavities is chosen to be 805 MHz.

The physical size of the cavities is limited by the bore of the superconducting solenoid (see Fig. 1.2). For each cavity module, the allowable structural length is 0.9 to 1.3 meters, and the maximum allowable radial extent is 17 centimeters. The extent of the structural length is determined mainly by the amount of muon re-acceleration needed. The length constraint limited each module to either 6 or 8 cells.

3.1.1 Design Rationale

To make the best use of the klystron input power, the shunt impedance of the cavity needs to be maximized. This yields the maximum accelerating gradient for a given input power to the accelerating structure. One of the important factors that determines the shunt impedance is the size of the iris opening. The shunt impedance decreases rapidly as the iris size increases. For this reason, the cell irises were designed to follow the maximum orbit of the particle beam as shown in Fig. 1.2.

The quality factor ($Q_\circ$) is proportional to the shunt impedance (R_s) and needs to be maximized as well. Generally speaking, $Q_\circ$ is maximized by reducing the power

losses at the cavity walls, while maintaining a reasonable level of stored energy in the cavity. Since the power loss at the cavity wall is due to the surface current induced by the magnetic field, one needs to know the radial behavior of the magnetic field. The analytical pill-box cavity solutions derived in chapter 2 can be used as guidance. According to the pill-box solutions, the magnetic field increases radially like the first derivative of the Bessel function J_0 and is high at the outer wall of the pill-box. Therefore, reducing the corners of the cavity reduces the fields on these surfaces. From a geometrical point of view, the wall surface area should be minimized to reduce surface losses.

Another guideline for maximizing the quality factor is from the equivalent circuit analysis of RF cavities. Using a RLC circuit model to represent the cavity, one obtains the relationship $R_s/Q_\circ = \sqrt{L/C}$ where L is the inductance and C is the capacitance. This relation gives us the hint that in general, the cavity shapes should be optimized to yield high L and low C.

A major concern of designing high gradient RF cavities is surface voltage breakdown (or sparking). All sharp corners in the cavity are rounded to circular arcs to avoid excessive concentration of charges. Since the high electric field regions are at the irises, the irises are casted into circular shapes. Quantitatively, one wishes to minimize the ratio of the maximum surface electric field E_s to the maximum on-axis electric field $E_\circ$. Specifically, the ratio $E_s/E_\circ$ must be 3 or less because $E_s = 90$ MV/m is the empirical breakdown surface field of copper at 805 MHz and $E_\circ = 30$ MV/m is the minimum accelerating gradient requirement.

In summary, the design criteria for the cavity are the following: (1) maximize the shunt impedance, (2) maximize the quality factor, (3) maximize the shunt impedance to quality factor ratio, and (4) minimize the ratio of maximum surface electric field to on-axis electric field. The optimization of these parameters requires the simulation of the cavity fields.

3.1.2 Numerical Models

This section presents the geometrical cavity model for the simulation of the cavity modes and explains the design choices for the various cavity dimensions.

The cavities that were considered for the simulations were the 6-cell and the 8-cell structures. The 6-cell example is shown in Fig. 3.1. For the purposes of structural

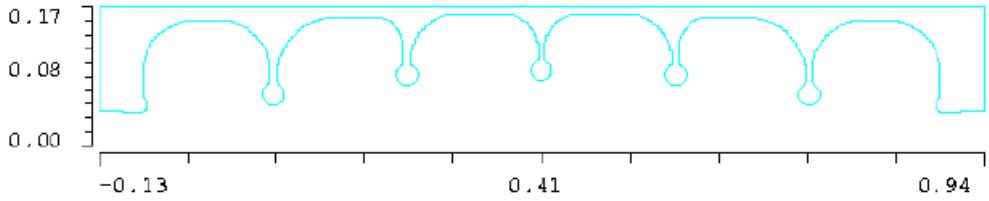

Figure 3.1: The 6-cell cavity model. The dimensions are in meters.

tuning and optimization of the cavity performance, individual cells were modeled first. The cell length is determined by the relation $kl_c = \pi$ where k is the propagation constant (wave number), l_c is the cell length and π is the phase advance per cell for a π mode cavity. After some substitutions of variables, the cell length becomes $l_c = \beta c/(2f)$ where $\beta = v_p/c$ and v_p is the particle velocity, c is the speed of light, and f is the operating frequency. In obtaining the cell length, the phase velocity of the RF wave is chosen to match the average velocity of the beam in order to have

proper beam acceleration. For an operating frequency of 805 MHz and a β of 0.87 (corresponding to an average beam momentum of 186 MeV/c), the cell length is 16.2 centimeters. The cross sections of the beam pipes are chosen to prevent the excitation of the waveguide modes. The beam pipe length is determined to be 3.926 cm by the requirement that the power of the evanescent mode falls off by 60 dB at the beam pipe end. It is calculated by the attenuation constant formula $\alpha_{dB} = 2\pi(8.678)l/\lambda_c$ where α_{dB} is the attenuation constant in unit of dB, l is the beam pipe length and λ_c is the cutoff frequency of the TM_{01} circular waveguide mode. For mechanical stability reason, the iris wall thickness and the outer wall thickness of the third (or fourth) cell are chosen to be 0.810 cm and 1.318 cm respectively. All other dimensions such as the radii of the iris balls, the cell arcs and the cell radii are free parameters for optimization and tuning.

3.1.3 Simulation Procedures and Results

The field solutions of the cavity modes were simulated using the Mafia eigenmode solver. Since the cavity has cylindrical symmetry, it was modeled in two dimension (rz coordinates). Because the mid-plane of the cavity is a symmetry plane, only half (first 3 cells) of the structure was simulated. The modes of specific interest are those in the passband of the TM monopole mode (TM_{010}). The chosen acceleration π mode is the last mode in the passband.

Due to the non-uniformity in the geometry of the irises, the cavity has three cells with different geometries and a symmetry plane at the third (middle) iris. For the sake of simplicity, the design of the 6-cell cavity began with the design of the

individual cells. First, each cell was optimized separately for high shunt impedance and high quality factor. Then they were tuned to 805 MHz. After the optimization of individual cell, all the cells were put together and simulated as a whole to obtain the overall RF characteristic of the cavity.

In the following discussion, the second cell is used as an example. The first and third cells were simulated in a similar manner. Figure 3.2 is the Mafia model of the

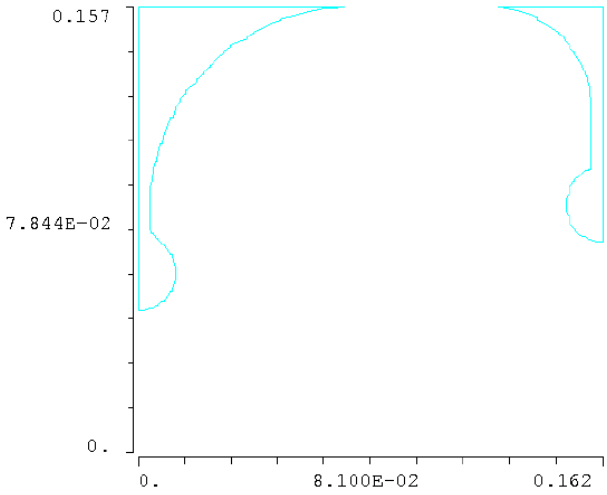

Figure 3.2: Model of the second cell in the cavity. The dimensions are in meters.

second cell.

A good field simulation requires the correct assignments of material properties and boundary conditions to the cell. The material of the cell walls is assumed to be a perfect conductor. For the calculations of all relevant cavity parameters, the perfect conductor solutions are adequate because of the small skin depth (at the sub-micron level) of copper. Vacuum is assumed inside the cell. The electric boundary condition is applied at the cell wall at the outer radius (maximum r) because of the presence of

electric conductor. At the left and right boundaries, magnetic boundary conditions are used because of the iris openings[1]. Magnetic boundary condition is also used at the cell axis because of the vanishing of the magnetic field there.

For the π mode cavity, each cell resonates in a TM_{010} mode that is similar to that of the pill-box cavity, as shown in Figs. 3.3 and 3.4. Figure 3.3 indicates that the

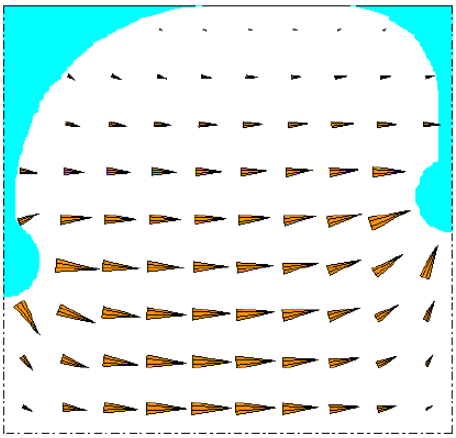

Figure 3.3: Electric field of the TM_{010} mode in the cell.

electric field is mainly longitudinal and decreases rapidly at the iris regions. Figure 3.4 shows the azimuthal nature of the magnetic field. The fields as a function of radius R at the mid-plane of the cell are plotted in Figs. 3.5 and 3.6. The electric field is the greatest on the cavity axis and falls off like the Bessel function J_0, which is ideal for beam acceleration. On the other hand, the magnetic field increases like the first derivative of the Bessel function J_0. This is the reason why one should make the

[1]In the case of the 3-cell model, the simulations show that either electric or magnetic boundary condition can be used at the side-wall of the beam pipe end. The difference in the mode frequencies between these two boundary conditions are a few tens of kHz. This is because the cutoff frequency of the lowest propagating mode TE_{11} in the beam pipe (considered as circular waveguide) is $f_{11} = c_\circ p'_{11}/(2\pi a) = 2.1975$ GHz, where p'_{11} is the root of J'_1 (derivative of the Bessel function of the first kind) and a is the radius of the waveguide. Hence the π mode can't escape into the beam pipes and the effects of different boundary conditions on its frequency is negligible.

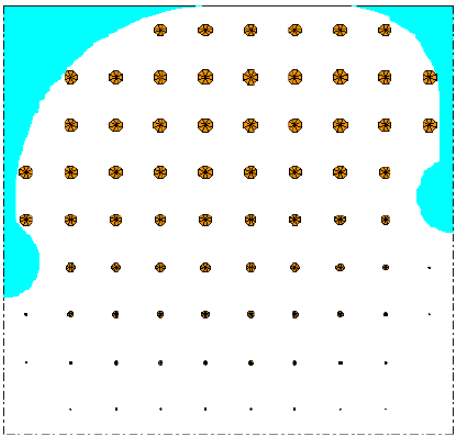

Figure 3.4: Magnetic field of the TM_{010} mode in the cell.

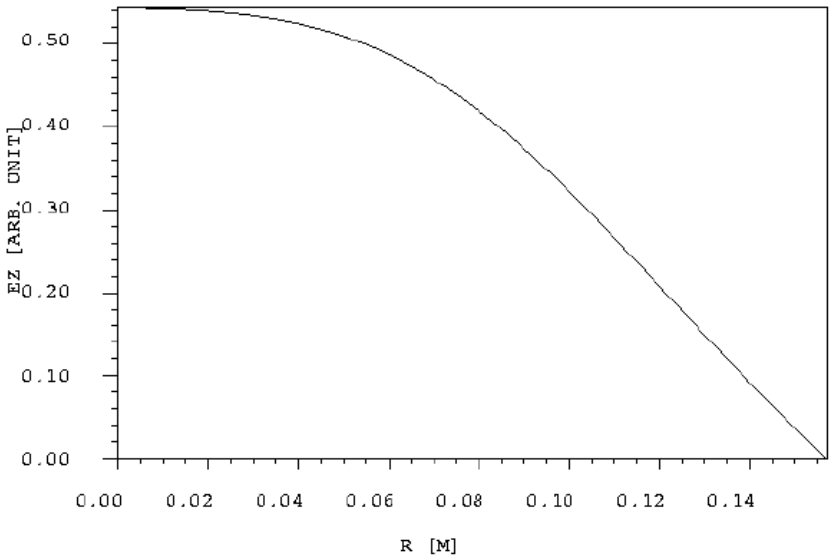

Figure 3.5: The longitudinal component of the electric field of the TM_{010} mode as a function of radius R at the mid-plane of the cell.

cavity wall at the equatorial region into curved surface to minimize the surface area (or the power loss).

The optimization of the cell was done in several steps. First, the sizes of the left and right cell arcs (see Fig. 3.2) at the cell radius were adjusted to yield high Q_o.

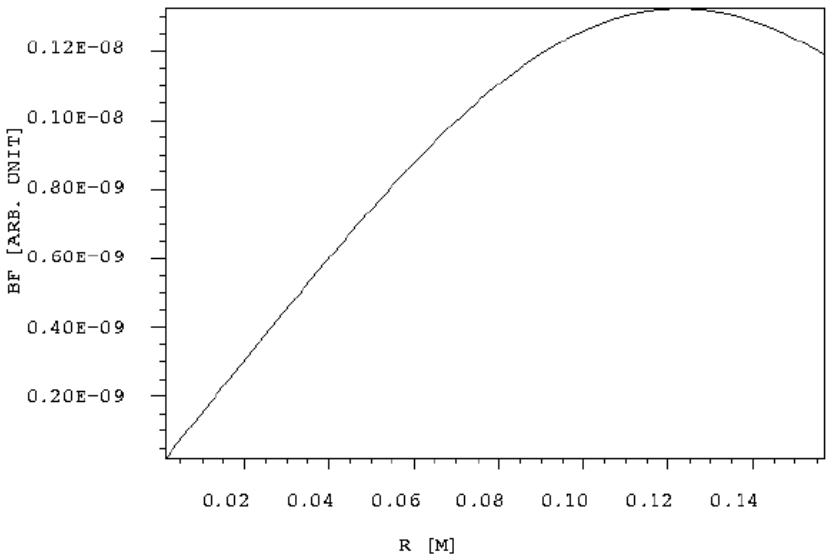

Figure 3.6: The azimuthal component of the magnetic field of the TM_{010} mode as a function of radius R at the mid-plane of the cell.

Then the iris ball radii were changed to give low $E_s/E_\circ$ ratio. Finally, the cell was tuned to 805 MHz by adjusting the cell radius.

After the simulations of the fields, the Mafia postprocessor was used to compute the total stored energy, the power loss at interior surfaces and the voltage on the cavity axis. The total stored energy is the sum of the time averaged electric and magnetic energies. The power loss is calculated by assigning the copper conductivity (5.8×10^7 $\Omega^{-1}\mathrm{m}^{-1}$) to the surface and using the perfect conductor solution of the magnetic field at the surface. This method is very accurate for good conductors at microwave frequencies. The voltage is computed as the line integral of the electric field on the axis where the field is corrected by the transit time factor T. Table 3.1 shows the simulation results for each cell. The end cells have the largest shunt impedance because they have the smallest irises.

Table 3.1: Quality factor, shunt impedance and $E_s/E_\circ$ for individual cells.

Cell	$Q_\circ$	R_sT^2 (MΩ/m)	$E_s/E_\circ$
1	34553	23.9	1.597
2	33315	16.9	1.948
3	34219	12.3	2.367

The simulation results for the 6-cell cavity are summarized in table 3.2. By comparing the data in tables 3.1 and 3.2, one sees that the couplings between cells lower

Table 3.2: Quality factor, shunt impedance and $E_s/E_\circ$ for the cavity.

Cell	Q_L	R_sT^2 (MΩ/m)	$E_s/E_\circ$
1	32961	25.9	1.600
2	32234	16.5	1.957
3	33164	11.9	2.373
	$Q_\circ$		
all	32813	17.9	2.019

the quality factor of individual cells by three to four percent. This behavior is consistent with the relation $Q_\circ = Q_L(1+\beta)$ where $Q_\circ$ is the unloaded Q of the individual cell, Q_L is the loaded Q and β is the coupling coefficient between the cells. The 2D electric field and the on-axis field profile are plotted in Figs. 3.7 and 3.8, respectively. Notice that in Fig. 3.8 the field decreases along the axis due to the decrease in the cell shunt impedance along the structure. The normalized peak on-axis electric fields are summarized in table 3.3. The fields in the end cells are about 17% higher than those of the middle cells.

The design choice for the 6-cell or the 8-cell cavity depends on their RF performance and cost. Simulation for the 8-cell cavity shows that its quality factor and

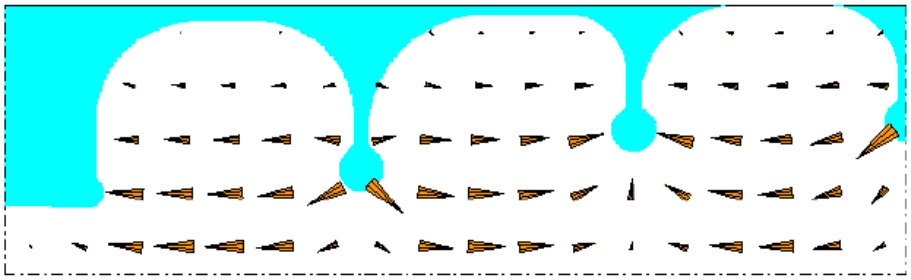

Figure 3.7: Electric field of the π mode of the 6-cell cavity. Half of the structure is simulated.

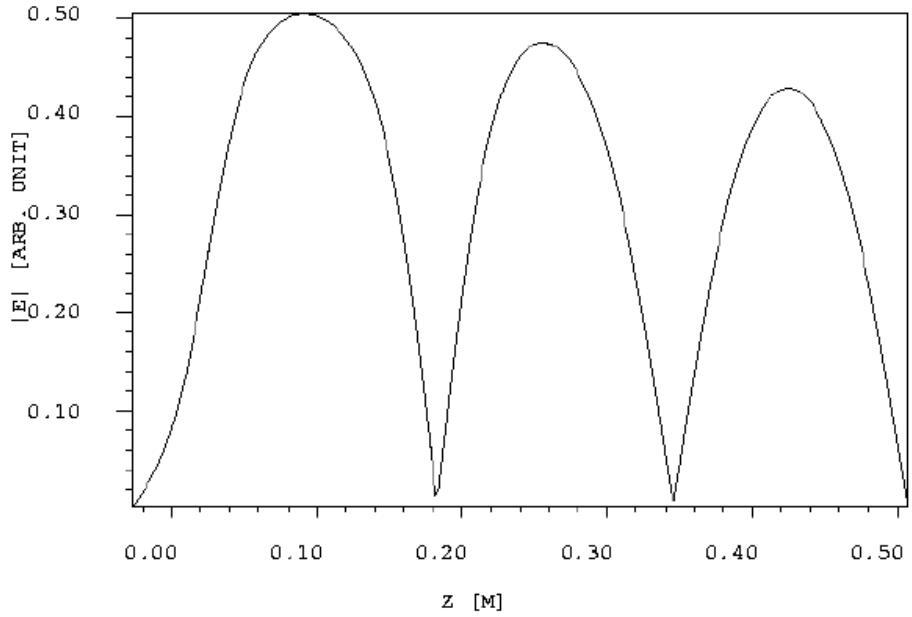

Figure 3.8: On-axis electric field profile (π mode) of the cavity. Only half of the structure is simulated.

Table 3.3: Normalized peak electric field levels in the cells.

Cell	1	2	3	4	5	6
$E_\circ/E_{o3}$	1.176	1.108	1.000	1.000	1.108	1.176

shunt impedance are similar to those of the 6-cell cavity. The difference is plus and minus a few percents. Hence, the 8-cell cavity has no apparent advantages over the 6-cell cavity. However, it costs more to build the 8-cell structure. Therefore the 6-cell structure was chosen for fabrication and testing in the superconducting solenoid.

3.1.4 RF System Specifications

The important parameters and the derived quantities of the cavity system are summarized in table 3.4. In the table, the shunt impedance Z_s is not corrected by the

Table 3.4: RF parameters for the cavity system.

Frequency (MHz)	805
Cell length (cm)	16.2
Z_s (MΩ/m)	31
$Q_\circ$	32813
Time constant (μs)	6.5
Transit time factor	0.76
Power (MW/m) for 30 MV/m	29
Repetition rate (Hz)	15

transit time factor and the power is computed using Z_s. The time constant is for the case of critical coupling. The dimensions of the cells, the irises and the beam pipes are shown in tables 3.5, 3.6 and 3.7, respectively. Note that "right" in the tables 3.6 and 3.7 designates on the side of the coupling cell.

3.2 High Power RF Coupler

RF coupler is an important part in the design of an accelerator structure because the efficiency of power delivery to the cavity depends critically on the geometry of

Table 3.5: Structural dimensions of the cells.

Cell	Cell Radius (cm)	Left Arc Radius (cm)	Right Arc Radius (cm)	Outer Wall Radius (cm)
1	15.255	5.724	6.058	17.460
2	15.684	3.518	7.059	17.460
3	16.183	4.283	5.653	17.460
4	16.183	5.653	4.283	17.460
5	15.684	7.059	3.518	17.460
coupling	15.212	6.014	5.680	17.460

Table 3.6: Structural dimensions of the irises.

Iris	Radius (cm)	Ball Radius (cm)	Wall Thickness (cm)
left end	4.000	0.900	2.634
1	5.000	1.300	0.810
2	7.400	1.300	0.810
3	8.000	1.250	0.810
4	7.400	1.300	0.810
5	5.000	1.300	0.810
right end	4.000	0.900	2.634

Table 3.7: Structural dimensions of the beam pipes.

Beam Pipe	Length (cm)	Radius (cm)
left	3.926	4.000
right	3.926	4.000

the coupler. There are several criteria for coupler design. First, the coupling cell needs to be in tune with the operating frequency (805 MHz) in order to provide the proper phase advance for the beam. Second, for maximum energy transfer to the accelerating structure, the cavity has to match to the feeding waveguide; *i.e.*, critical coupling ($\beta = 1$) is required. Third, the surface field in the coupler should be

minimized in order to reduce the risk of RF breakdown. Fourth, the field asymmetry in the cavity due to single input coupler should have minimal adverse effects on the beam. The last point won't be a problem for the 805 MHz cavity by virtue of the large muon beam size.

The design requirements make coupler design inherently a nontrivial 3D problem. Previously, the optimal dimensions of the coupling cell were often determined experimentally by trial and error. This is time consuming and requires substantial amount of empirical expertise. With the advent of powerful 3D electromagnetic code such as Mafia, the coupler dimensions can be predicted efficiently and accurately. Designing the coupler is done with the energy method [13] using Mafia 3D time domain and 2D eigenmode solvers[2]. The calculation of the coupling coefficient requires two time domain runs, *i.e.*, one for tuning and one for matching. For standing wave accelerating structures, the simulations of the steady state solutions take considerable amounts of time and memory space because of the high $Q_\circ$ value. The advantage of the energy method is that it utilizes the waveguide boundary condition in Mafia to provide the match load at the waveguide port, and the non-steady state solutions to compute the coupling coefficient by assuming $\beta = Q_\circ(t)/Q_e(t)$ valid at any time.

3.2.1 Numerical Models

Since the coupler design is a 3D problem, it is impractical to simulate the entire 6-cell structure in xyz coordinates. Instead, a 3D model consisting of the first two cells and

[2]The energy method treats the coupling coefficient calculation as a three dimensional problem in the time domain. The cavity fields are simulated as functions of both space and time. The fields are utilized to calculate power flow and power loss in the cavity.

the feeding waveguide is used. Furthermore, because of a reflection symmetry, only half of the structure needs to be simulated.

As seen from Fig. 3.9, energy coupling to the cavity is through a rectangular

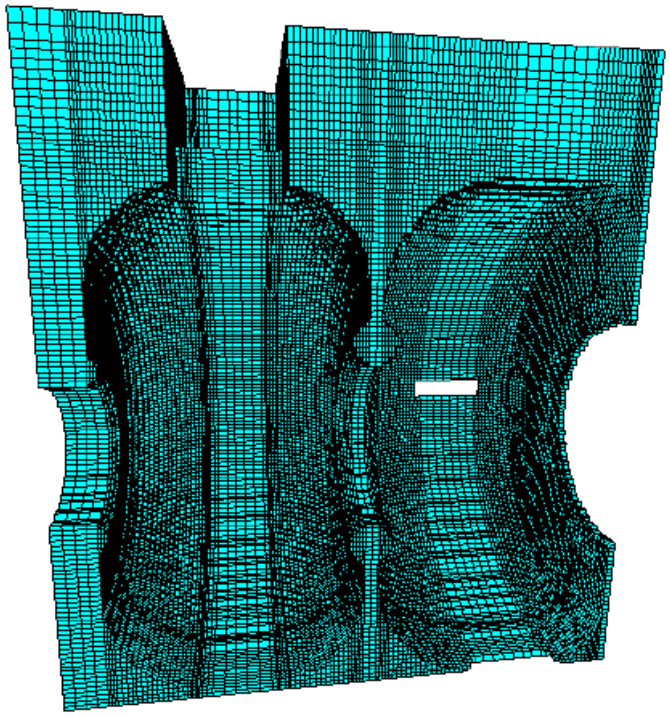

Figure 3.9: Three dimensional (xyz coordinates) 2-cell model for the coupler design. Note that only part of the input waveguide is shown.

aperture located at the outer wall of the end cell. This is the only location allowed in the cooling channel design. The orientation of the coupling slot is chosen to match the waveguide TE_{10} mode into the cavity π mode. The actual length of the waveguide is one guide wavelength (0.5658 m). The width of the waveguide is the same as that of the standard waveguide (WR975), but it is only half as high. The restriction on the height is imposed by the cooling channel design. The material of the cavity is assumed to be perfect conductor with vacuum inside the cells.

The transverse and longitudinal cross sectional views of the coupling cell are shown in Fig. 3.10. Generally, one has to determine the optimal set of width w, height h,

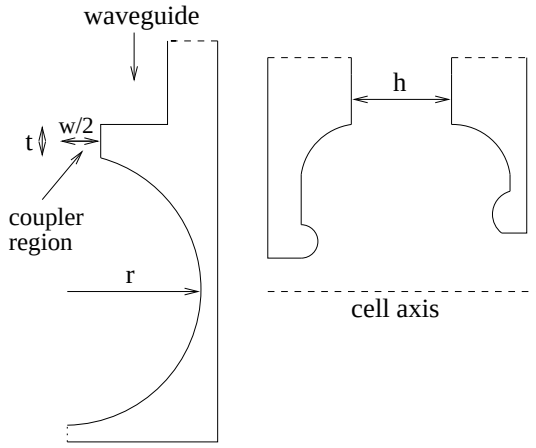

Figure 3.10: Transverse and longitudinal cross sectional views of the coupling cell.

thickness t and radius r for critical coupling. In this case, the thickness of the coupling slot is fixed as the outer wall thickness of the coupling cell. To lower the risk of RF breakdown, the ratio of the maximum field in the coupling slot to that of the waveguide, E_{cp}/E_{wg}, is minimized by setting the slot height equals the waveguide height. Simulation shows that $E_{cp}/E_{wg} = 3.3$. For a peak power of 12 MW (Fermilab 805 MHz klystron), the maximum electric field (E_{max}) in the waveguide is 1.339 MV/m for the TE_{10}. The peak field is computed using the power flow formula

$$P = 6.63 \times 10^{-4} E_{max}^2 wh[1 - (\lambda_\circ/\lambda_c)^2]^{1/2} \ ,$$

where w and h are the width and height of the waveguide, $\lambda_\circ$ is the free space wavelength and λ_c is the cutoff wavelength of the TE_{10} mode. For the given maximum E_{wg}, the peak field in the coupling slot is 4.418 MV/m, which is less than the limit

(90 MV/m) of surface breakdown field for copper. Besides the minimization of the E_{cp}/E_{wg} ratio, all corners of the coupling slot's cross section are rounded to a radius of 7 mm to minimize sparking. The remaining parameters w and r determine the matching and tuning of the cavity, respectively.

All boundary conditions (BC) in Fig. 3.9 are chosen according to the orientations of the electric and the magnetic fields at the boundaries. In the longitudinal direction z (along the cavity axis), the magnetic BC is used at the beam pipe and the second iris because of the openings. In the x direction (into the page in the Fig. 3.9), magnetic BC is applied at low x and electric BC at high x (because of the presence of the conducting wall). Along the waveguide direction y, electric BC is used at low y, while waveguide BC is used at high y (location of the waveguide port).

In general, the waveguide boundary condition in Mafia simulates an infinitely long waveguide. Thus it provides a match load at the waveguide port. The transverse electromagnetic fields of the waveguide modes for the waveguide BC are simulated in the 2D eigenmode solver and loaded into the time domain simulations. Figures 3.11, 3.12 and 3.13 show the transverse fields of the waveguide TE_{10} mode at the waveguide port. Only half of the structure is simulated because of symmetry. The frequency range where only the TE_{10} mode can propagate goes from 605.7 MHz to 1211 MHz (the cutoff frequency of the next mode). At the operation frequency of 805 MHz, TE_{10} is the only propagating mode in the waveguide.

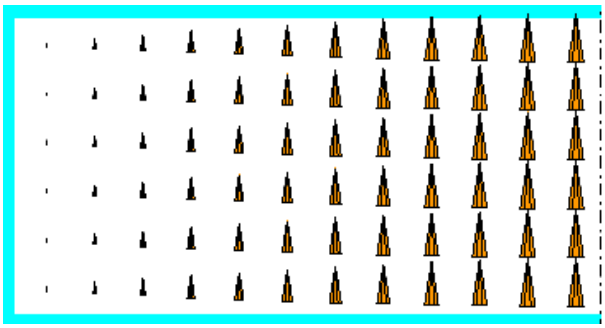

Figure 3.11: Real part of the transverse electric field of the TE_{10} waveguide mode at the waveguide port. Only one half of the waveguide cross section is plotted.

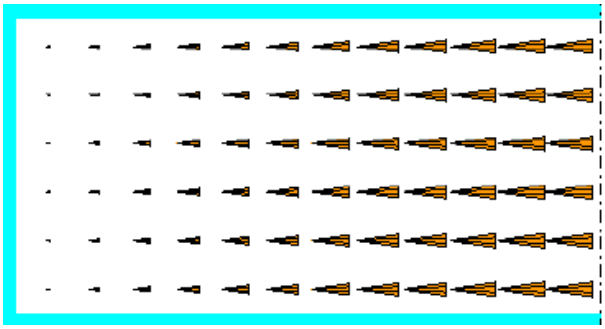

Figure 3.12: Real part of the transverse magnetic field of the TE_{10} waveguide mode at the waveguide port. Only one half of the waveguide cross section is plotted.

Figure 3.13: Imaginary part of the transverse magnetic field of the TE_{10} waveguide mode at the waveguide port. Only one half of the waveguide cross section is plotted.

3.2.2 Structure Tuning

The two cells of the model (Fig. 3.9) were tuned separately using the 3D time domain solver with the design goals of 805 MHz and on axis field ratio $E_1/E_2 = 1.061$ (see table 3.3). This saved considerable amounts of time and memory space compared to the case of tuning both cells together. The first cell with the coupling slot and the waveguide is used as an example in the following tuning demonstration.

The structure was excited by a Gaussian shaped dipole signal (Fig. 3.14) with

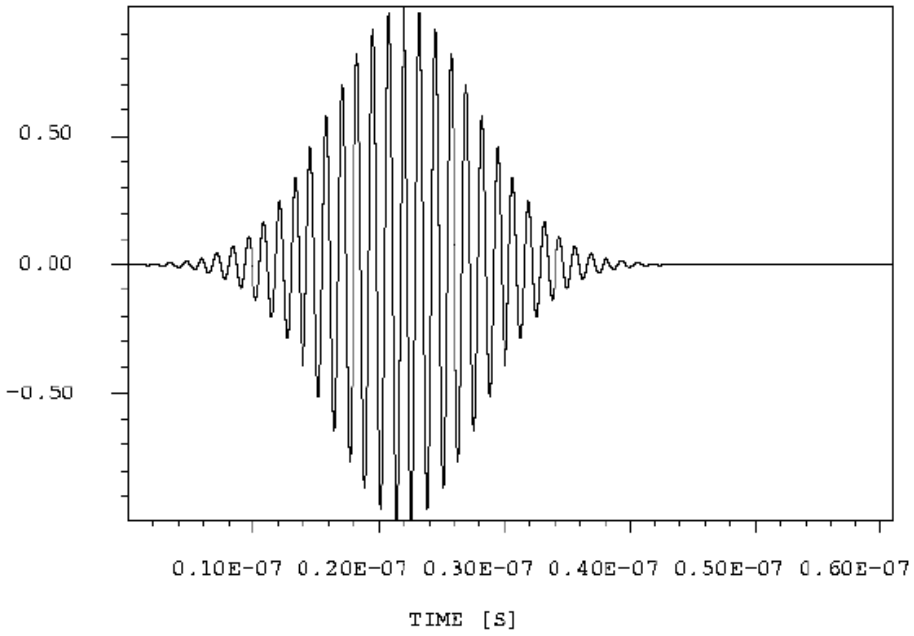

Figure 3.14: Dipole excitation signal for cavity tuning. The signal is normalized to one.

center frequency 805 MHz. The bandwidth of the signal was carefully chosen not to excite adjacent modes. Eigenmode simulation shows that the closest mode is about 500 MHz away. Hence a 60 dB bandwidth of 200 MHz for the dipole pulse is sufficient.

The excitation signal was placed in the middle of the cell and oriented along the cell axis where the electric field of the π mode has a strong component. The mode that is nearest to 805 MHz was coherently excited. The total simulation time for the time domain run was 55 RF periods.

The time signal of a field component at a location away from the excitation signal and the 3D electric field near the end of the simulation were recorded for frequency and field calculations. The mode frequency could be obtained from either the Fourier transform or by measuring the length of the last 15 oscillations of the time signal. The time signal of the x component of the magnetic field is plotted in Fig. 3.15. From

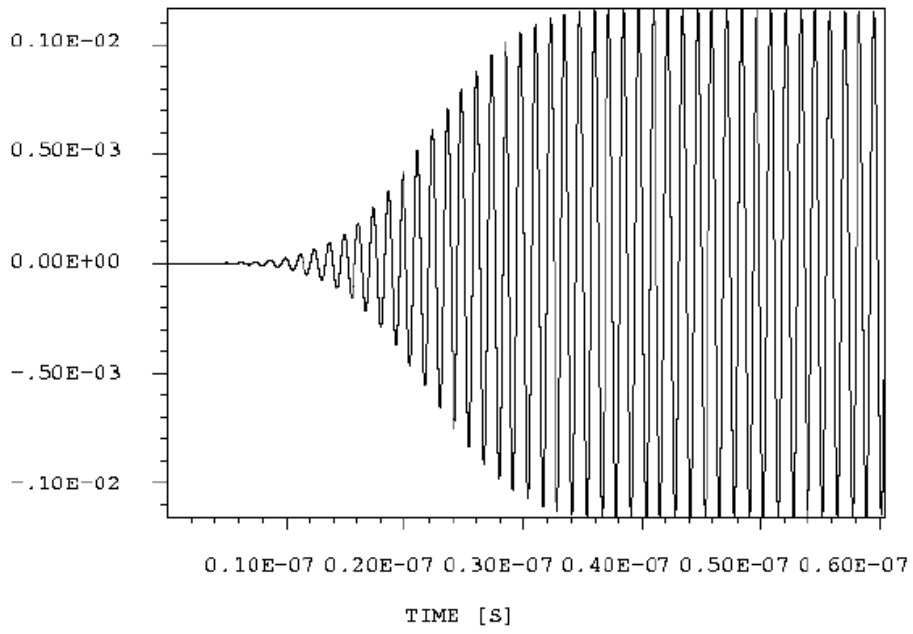

Figure 3.15: Time signal of the x component of the magnetic field inside the cell. Signal amplitude is in arbitrary unit.

the plot, one sees that the field builds up and levels off to a constant value when the excitation signal turns off. No decay behavior is seen here because the time constant

of the system is about two orders of magnitude larger than the total simulation time and also the structure is assumed to be a perfect conductor. Figures 3.16 and 3.17 show the electric fields in the cell and in the waveguide. The field behaves like the

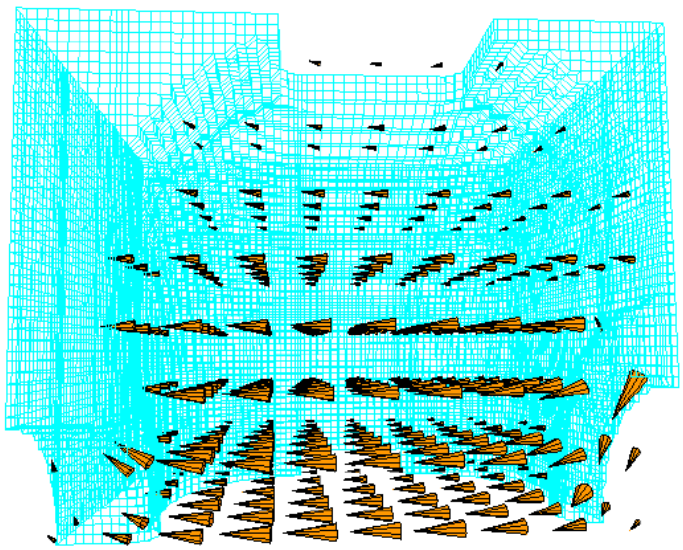

Figure 3.16: Electric field in the coupling cell. Only one quarter of the cell is shown here.

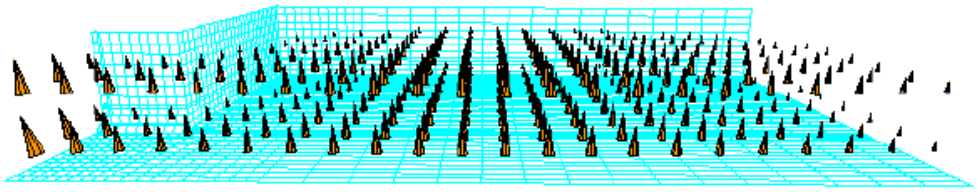

Figure 3.17: Electric field in the waveguide and the coupling slot (left).

TM_{010} mode in the cell, while in the waveguide like the TE_{10} mode. The maximum fields on the axis, in the coupling slot and in the waveguide are calculated from these 3D fields. Table 3.8 summarizes the simulation results for the case of a coupling slot width of 3.23 inches. For all tuning simulations, the cell frequencies are within

Table 3.8: Frequencies and field levels of the two cells.

Cell	Frequency (MHz)	Field Level (E_1/E_2)
1	805.218	1.047
2	805.015	1.000

500 kHz of the design frequency 805 MHz.

3.2.3 Structure Matching

A second time domain run was performed to find the coupling coefficient of the 6-cell cavity (Fig. 3.1), with the design goal of critical coupling ($\beta = 1$), using the two-cell model (Fig. 3.9). The coupling coefficient, assumed to be valid at any time, is

$$\beta = \frac{Q_\circ(t)}{Q_e(t)} \tag{3.1}$$

where $Q_\circ(t) = w_\circ U_T(t)/P_w(t)$ and $Q_e(t) = w_\circ U_T(t)/P_e(t)$, $w_\circ$ is the angular frequency of the cavity mode, U_T is the total stored energy, P_w is the total power loss at the cavity walls and P_e is the power flow out of the cavity into the waveguide port. As one can see, the coupling coefficient depends on the total wall loss in the 6-cell cavity which needs to be represented in the two-cell model.

In order to simulate the total wall loss in the 6-cell (copper) cavity, the conductivity of the second cell (the cell without the coupler) in the two cells model has to be adjusted to produce the total wall loss in cell 2 through 6. The conductivity was determined by using the 2D eigenmode solver where the wall loss in each cell could be calculated. The model for the simulation is shown in Fig. 3.1. Table 3.9 shows the normalized wall loss in each cell for a copper conductivity of 5.8×10^7 $(\Omega\text{m})^{-1}$.

Table 3.9: Wall losses in the 6-cell copper cavity.

Cell	1	2	3	4	5	6
wall loss (P_x/P_3)	0.6455	0.8052	1.0000	1.0000	0.8052	0.6455

Knowing the total wall loss in cell 2 through 6, the conductivity of the second cell is determined as 2.075×10^6 $(\Omega\mathrm{m})^{-1}$. The conductivity of the first cell is that of the copper.

In the time domain simulation, the 2-cell structure was excited by a monochromatic dipole signal of constant amplitude (shown in Fig. 3.18) at the in-tune frequency found in the previous section. The signal was located in the middle of the second cell

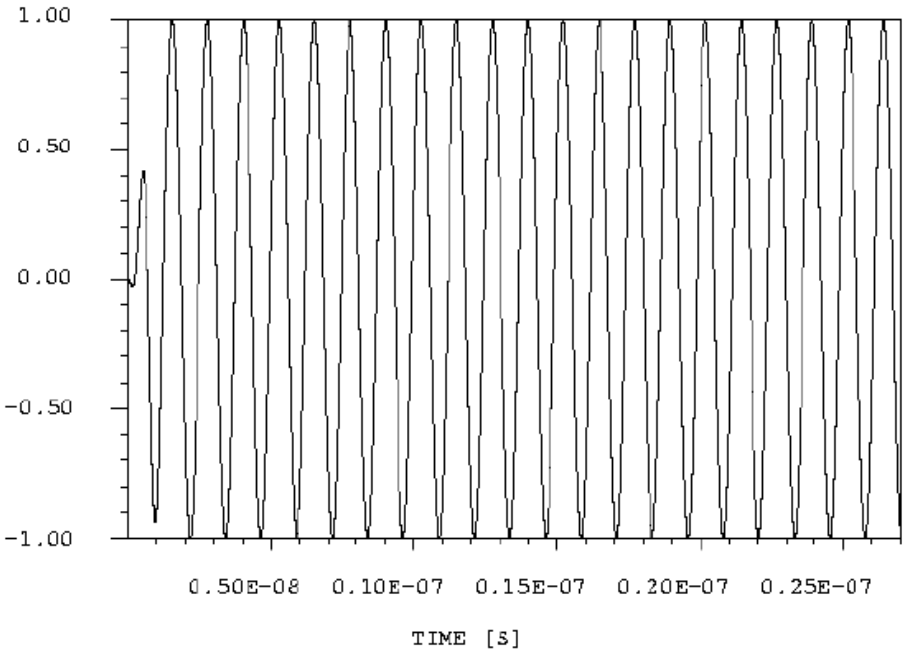

Figure 3.18: Monochromatic excitation signal for coupling coefficient simulations. About one fifth of the signal is shown. Signal is normalized to one.

and oriented along the cell axis to excite the π mode electric field. Its amplitude was

smoothly increased to one in one RF period and it continued indefinitely until the end of the simulation. Therefore, the signal delivered a constant amount of energy to the cavity per unit time. In a short time scale, its effects on the U_T, P_w and P_e calculations could not be ignored. However, its energy contribution relative to the total stored energy diminishes in time. One simple solution is to simulate long enough so that the difference in the coupling coefficients at two different times is at an acceptable level. The difference $\Delta\beta = \beta(t_2) - \beta(t_1) \leq 0.1$ for t_2 and t_1 near the end of the simulation was imposed. It was found that a total simulation time of 125 RF periods satisfies this stipulation.

The field components in the cavity were coherently excited according to

$$\Phi(t) = \Phi_\circ(1 - e^{-t/\tau}) \sin(w_\circ t + \theta_\circ) \tag{3.2}$$

where $\Phi_\circ$ is the steady state value, $\tau = 2Q_L/w_\circ$ is the time constant of the loaded system, $w_\circ$ is the angular frequency and $\theta_\circ$ is some arbitrary phase factor. The time signals of the x-component of the magnetic field in cell 1 and 2 are plotted in Figs. 3.19 and 3.20, respectively. All other field components have similar shapes. Data in table 3.10 show that the cells are fairly in tune. The nonlinear behaviors of the time signals indicate that there are very strong (electric) coupling between the two cells due to the large iris. Otherwise, the fields should increase linearly according to Eq. 3.2 for $t \ll \tau$. Anyhow, simulation with long run time (600 RF periods for example) indicates that the field signals do exhibit an overall linear behavior as shown in Fig. 3.21.

In the coupling coefficient calculation, the electromagnetic field was simulated as

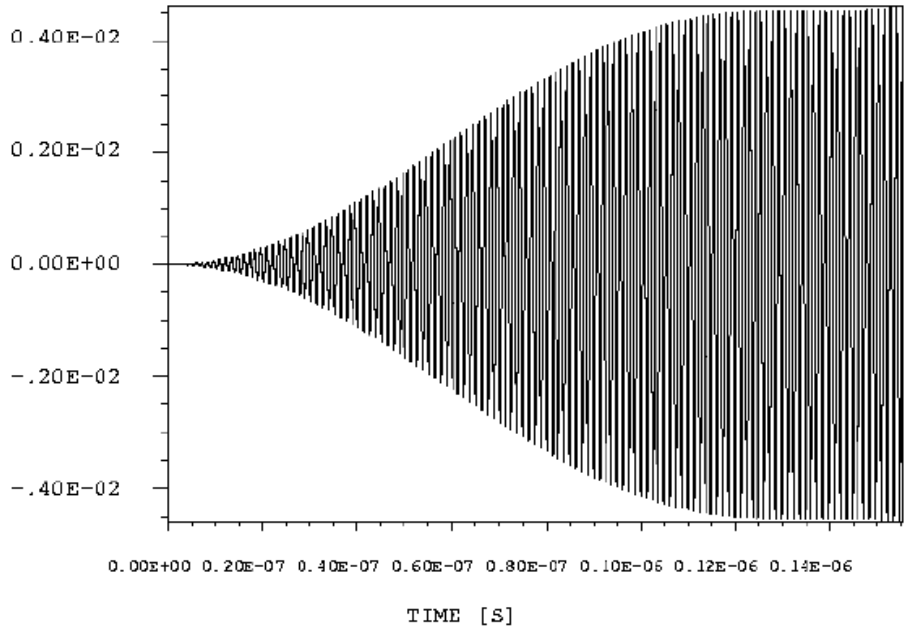

Figure 3.19: Time signal of the x-component of the magnetic field in cell 1.

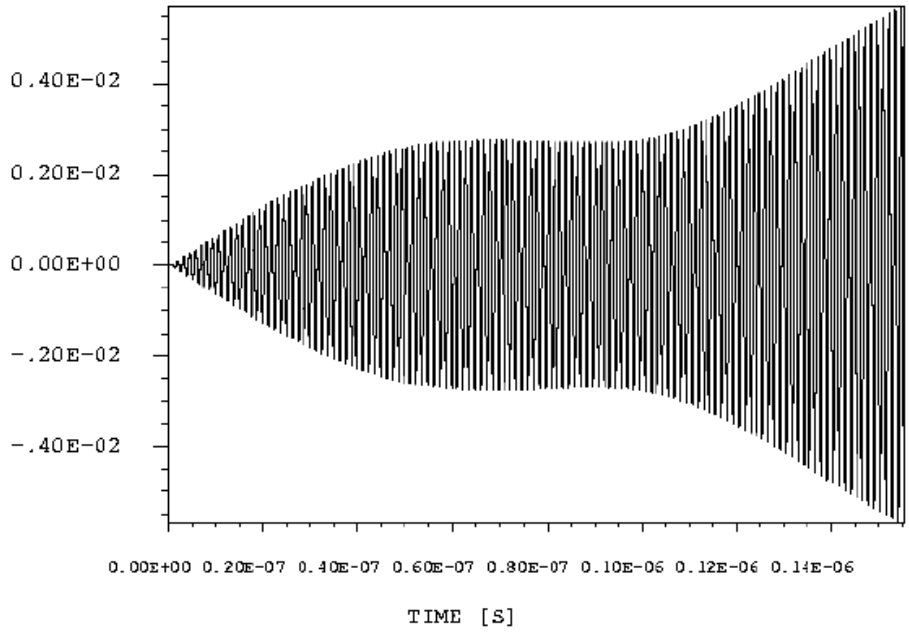

Figure 3.20: Time signal of the x-component of the magnetic field in cell 2.

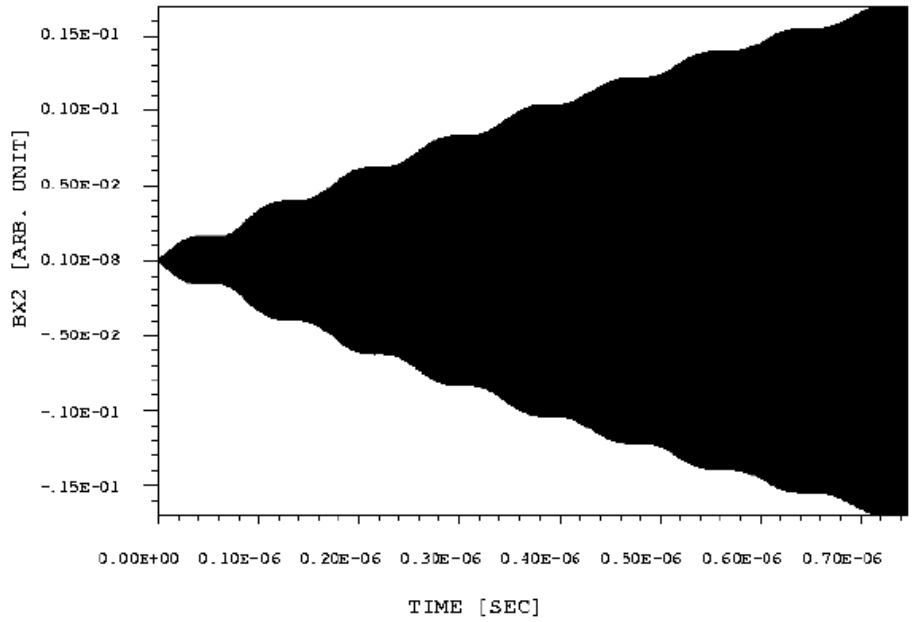

Figure 3.21: Time signal of the x-component of the magnetic field in cell 2. The total simulation time is 600 RF periods.

a function of time. The phase factors, *i.e.*, the sinusoidal time dependent parts, in the fields have to be canceled out; otherwise, the β values will vary depending on the time at which the fields are used. This problem is solved by combining the fields at $t_\circ$ and $t_\circ + T_{rf}/4$ where $t_\circ$ is near the end of the 125 RF periods and T_{rf} is the RF period. This effectively cancels out the phase factors. The wall loss and the external power are defined as

$$P_w(t_\circ) \approx \frac{R_s}{2} \oint_s [H^2(t_\circ) + H^2(t_\circ + \frac{T_{rf}}{4})] ds \tag{3.3}$$

and

$$P_e(t_\circ) \approx \frac{1}{2} \int_s [S_l(t_\circ) + S_l(t_\circ + \frac{T_{rf}}{4})] ds \ , \tag{3.4}$$

respectively. The wall loss integral is taken over the entire interior surface of the

cavity, while the external power is integrated over the transverse cross section of the waveguide port. In Eq. 3.3, R_s is the surface resistivity and H is the magnetic field at the surface. In Eq. 3.4, S_l is the longitudinal component of the Poynting vector directed out of the waveguide.

The coupling coefficient was calculated using the 3D electric and magnetic fields that are shown in Fig. 3.22 through 3.25. Figure 3.22 shows that the adjacent

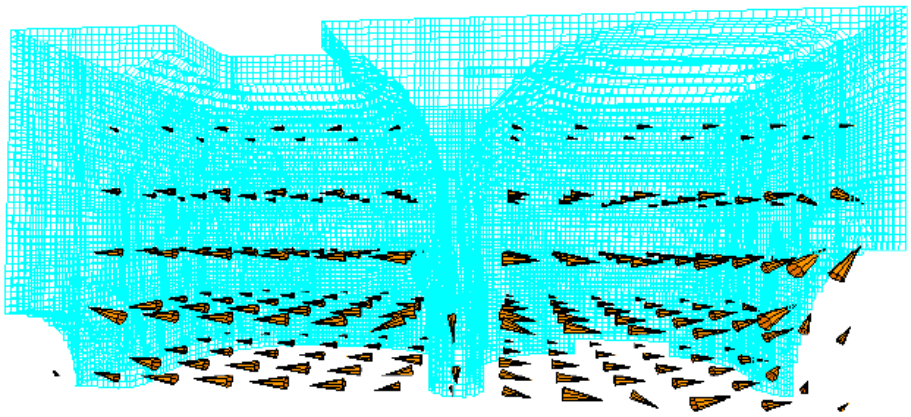

Figure 3.22: 3D electric field in the cavity. Only one quarter of the structure is shown here.

electric fields are 180° out of phase which is characteristic of the π mode. As indicated in Figs. 3.24 and 3.25, the fields in the waveguide are the TE_{10} mode. The Poynting vector showing the power flowing out of the cavity into the waveguide is plotted in Fig. 3.26. For an accurate determination of the coupling strength of the coupler, it is important that the simulated waveguide boundary condition provides a match load. By zooming into the region near the waveguide port, one can see whether there are reflections (*i.e.*, Poynting vector directed toward the cavity) at the waveguide port or not. The simulation results for a coupling slot width of 3.23 inches (the case closest

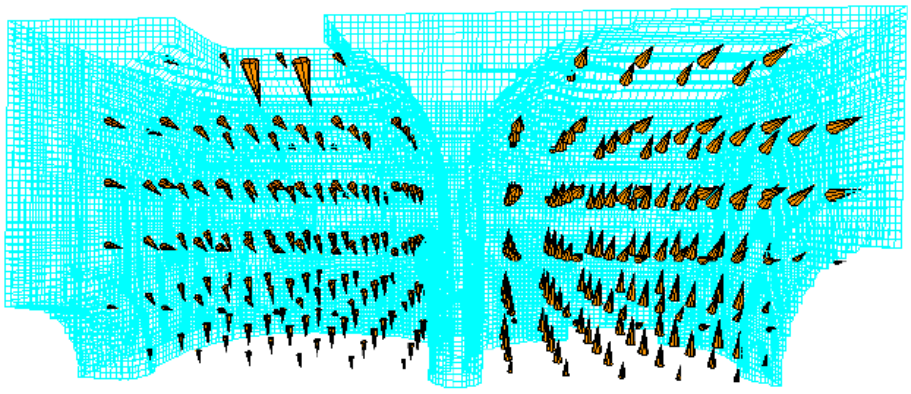

Figure 3.23: 3D magnetic field in the cavity. Only one quarter of the structure is shown here.

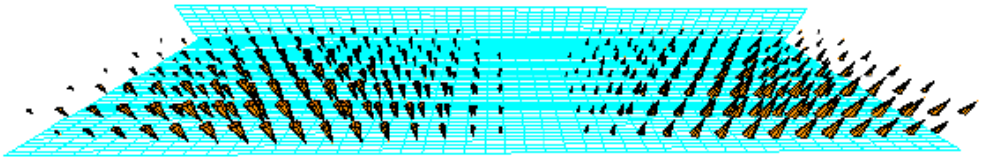

Figure 3.24: 3D electric field in the waveguide. The waveguide port is located at the right and the cavity (not shown) is to the left.

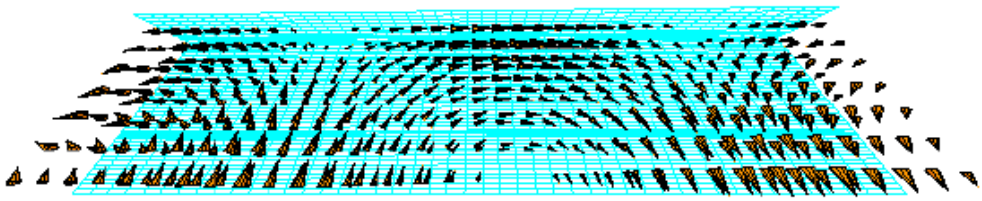

Figure 3.25: 3D magnetic field in the waveguide. The waveguide port is located at the right and the cavity (not shown) is to the left.

to critical coupling) and the dimensions of the connecting waveguide and the coupling slot are summarized in tables 3.10 and 3.11, respectively. The excitation frequency in this case is 805.060 MHz. The uncertainty in measuring the frequencies in Mafia is about 100 to 200 kHz. Several cases of slot width were simulated and the results

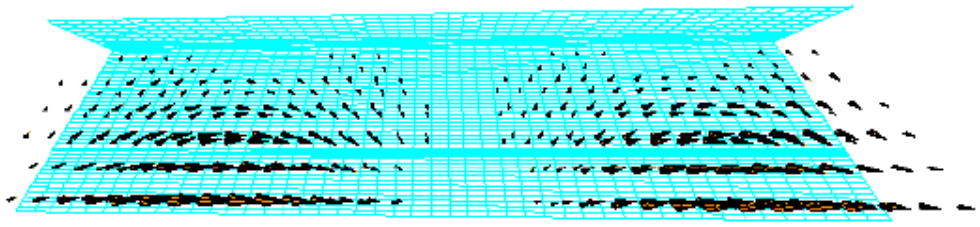

Figure 3.26: Poynting vector in the waveguide. Waveguide port is at the right and the cavity (not shown) is to the left.

Table 3.10: Coupling coefficient, frequencies, and field levels of the two cells for a coupling slot width of 3.23 inches.

β	Cell	Frequency (MHz)	Field Level (E_1/E_2)
0.959	1	805.283	1.012
	2	804.721	1.000

Table 3.11: Waveguide and coupling slot dimensions.

	Width (cm)	Height (cm)	Length (cm)
waveguide	24.765	6.191	
coupling slot	8.204	6.191	2.248

are plotted in Fig. 3.27.

3.3 Waveguide Section for Impedance Matching

In the engineering design of the cooling channel, the RF waveguide can't reach the cavity in the superconducting solenoid region due to limited space. A waveguide of smaller dimension (height) has to be used for connection to the cavity. Since the characteristic impedance of a rectangular waveguide is proportional to its height for the TE_{10} mode, matching is needed between the waveguide (WR975) from the

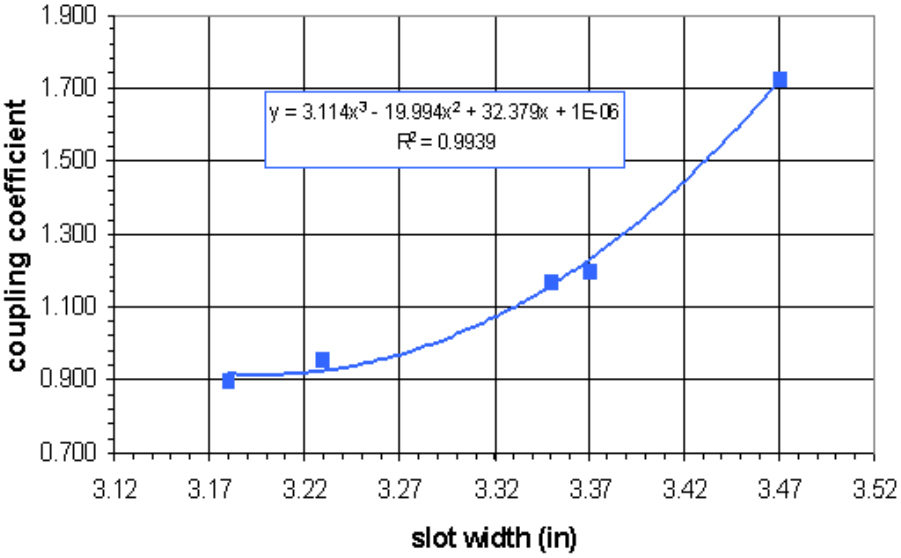

Figure 3.27: Coupling coefficient verse slot width.

klystron and the waveguide (chosen to be half the height of WR975) that connects to the coupler. The matching section needs to have less than 1% of reflected power (or equivalently, a reflection coefficient $|S_{11}| < 0.1$) and a bandwidth that covers the klystron bandwidth (1% of 805 MHz). Several designs were considered, *i.e.*, a straight taper, a 1-section and a 2-section quarter wave transformers. The cost and ease of fabrication determine which choice to use. Three dimensional time domain simulations were performed to calculate the reflection coefficient S_{11} and the transmission coefficient S_{21}.

3.3.1 Numerical Models

The 3D models for the various designs were setup in xyz coordinates as shown in Fig. 3.28 through 3.30. For each design, only half of the structure needs to be simulated. The lengths of the standard and half-height waveguides are one half guide

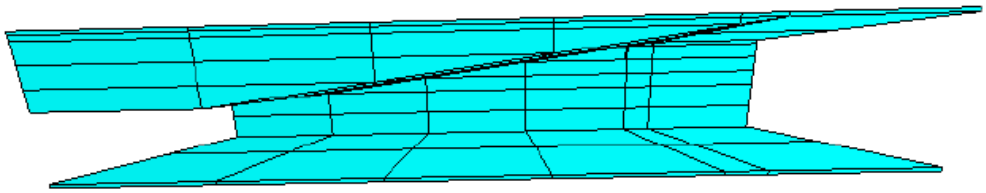

Figure 3.28: 3D model of the straight taper. For the waveguides at the two ends, only one quarter of their actual lengths is shown.

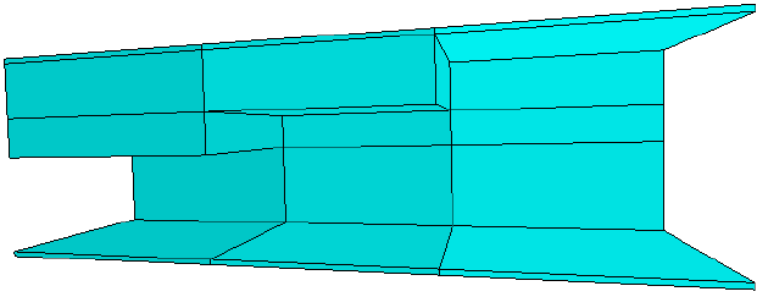

Figure 3.29: 3D model of the 1-section quarter wave transformer.

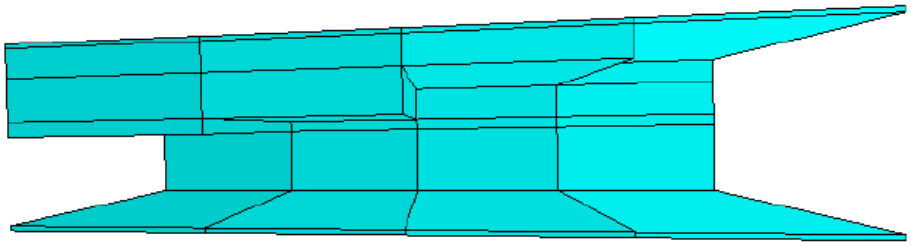

Figure 3.30: 3D model of the 2-section quarter wave transformer.

wavelength (28.289 cm) in the case of the straight taper and are one quarter guide wavelength (14.145 cm) in the cases of the quarter wave transformers. The cross sectional dimensions of the waveguides are listed in table 3.12. The widths of the taper and the transformers are the same as those of the waveguides. This allows transmission of the TE_{10} waveguide mode. The corners at the steps of the transformers were

Table 3.12: Cross sectional dimensions of the waveguides.

	Width (cm)	Height (cm)
standard waveguide	24.765	12.383
half-height waveguide	24.765	6.191

rounded to a radius of 1/8" to minimize the risk of sparking. The dimensions of the transformers would be determined according to the criteria developed in the section on impedance matching.

All boundary conditions are chosen according to field symmetries at the boundaries. The boundary conditions at low and high x (vertical direction) are electric. In the horizontal direction (into the page of Figs. 3.28, 3.29 or 3.30), electric BC is applied at low y and magnetic BC is at high y. At the two waveguide ports, waveguide BC is used to provide match loads. The waveguide BC is simulated the same way as in the coupler design. The materials of the structures are perfect conductors with vacuum inside the waveguides, the taper and the transformers.

3.3.2 Impedance Matching

The basic idea of impedance matching is illustrated in Fig. 3.31. The picture depicts

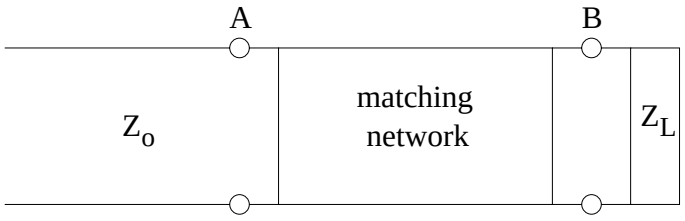

Figure 3.31: Basic idea of impedance matching.

the matching of an arbitrary load Z_L to a feeding line of characteristic impedance $Z_\circ$ by a lossless network. Intuitively speaking, the reflection that occurs at A due to the discontinuity in the characteristic impedance (or geometry) must be canceled out by the superposition of all the partial reflections from the matching network, so that the total reflection in the feed line is zero. The main reason for impedance matching is to provide maximum power transmission to the load, hence minimizing the power loss in the feed line due to reflections.

The circuit model in Fig. 3.32 is used to obtain the condition for impedance

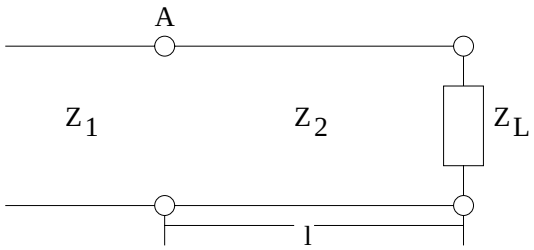

Figure 3.32: Circuit model of a 1-section quarter wave transformer.

matching by a 1-section quarter wave transformer. Applying transmission line theory, the effective load impedance (transformed by Z_2) presented to a lossless feed line at point A is

$$Z_A = Z_2[\frac{Z_L + iZ_2\tan(\beta l)}{Z_2 + iZ_L\tan(\beta l)}] \ , \tag{3.5}$$

where i is the imaginary number, β is the propagation constant and l is the length of the transformer. For a quarter wave transformer, $l = \lambda/4$. Taking the limit of $\beta l \to \pi/2$ in Eq. 3.5, Z_A becomes

$$Z_A = \lim_{\beta l \to \pi/2} Z_A = \frac{Z_2^2}{Z_L} \ . \tag{3.6}$$

Impedance matching requires $Z_A \equiv Z_1$ or equivalently $Z_2 = (Z_1 Z_L)^{1/2}$ for the transformer. The longitudinal cross section of the 1-section quarter wave transformer is shown in Fig. 3.33. The characteristic impedance for a traveling wave is the ratio of

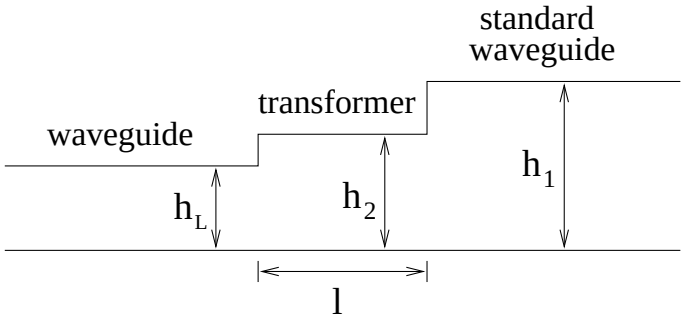

Figure 3.33: Longitudinal cross section of the 1-section quarter wave transformer.

voltage to current. For the TE_{10} mode in a rectangular waveguide,

$$Z \equiv \frac{V}{I} \propto \frac{hE_y}{wH_x} \tag{3.7}$$

where h is the waveguide height (along y direction), w is the waveguide width (along x direction), E_y is the electric field component and H_x is the magnetic field component. Then Eq. 3.6 yields $h_2 = (h_1 h_L)^{1/2}$, where h_1 and h_L are the heights of the standard and half-height waveguides, respectively. This simple relation provides the matching condition for the height of the quarter wave transformer. In reality, because there are losses in the waveguides and the effect of reactances associated with step discontinuities, the length l of the transformer is tuned to center the minimum of the reflection coefficient at 805 MHz.

For the 2-section quarter wave transformer, an extra quarter wave section is added as shown in Fig. 3.34. To find the matching condition, one applies Eqs. 3.5 and 3.6

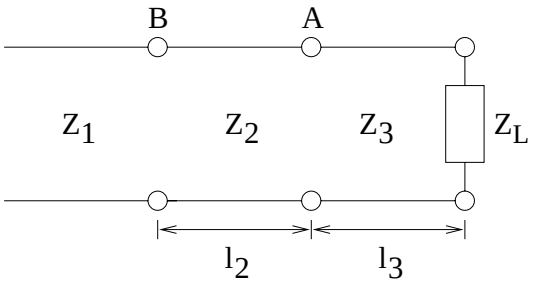

Figure 3.34: Circuit model of the 2-section quarter wave transformer.

twice and the matching requirement, $Z_B \equiv Z_1$ at point B. These operations yield the condition $Z_2 = Z_3(Z_1/Z_L)^{1/2}$. Figure 3.35 shows the longitudinal cross section

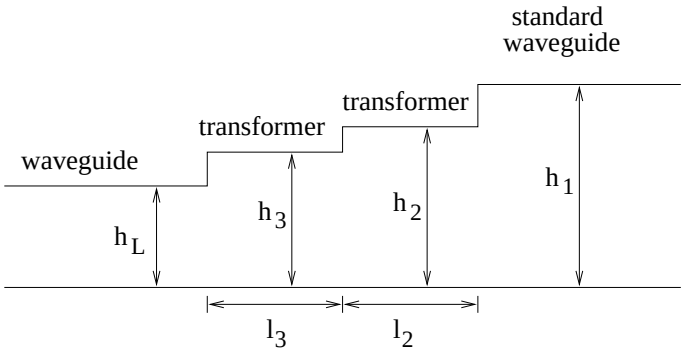

Figure 3.35: Longitudinal cross section of the 2-section quarter wave transformer.

of the 2-section quarter wave transformer. Using Eq. 3.7, one obtains the relation $h_2 = h_3(h_1/h_L)^{1/2}$ for impedance matching. Either h_2 or h_3 can be chosen to optimize the bandwidth of the transformer. One of the transformer lengths is used to shift the reflection coefficient minimum to 805 MHz.

For the continuous taper as shown in Fig. 3.36, it is useful to have approximate analytical solution for the total reflection coefficient to get a good estimate for its length and for the locations of the reflection coefficient minima. One can consider the

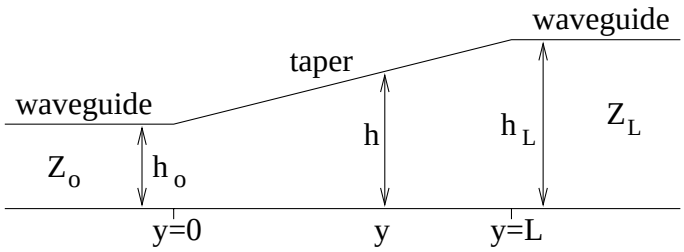

Figure 3.36: Longitudinal cross section of the continuous taper.

continuous taper as consist of many small steps and apply the theory of small reflections. At each step (Fig. 3.37), there is a small reflection $\Delta\Gamma$ due to the impedance

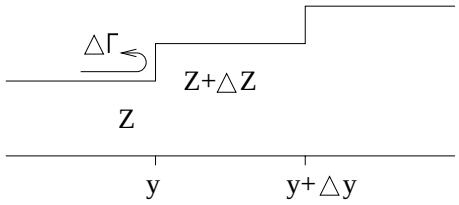

Figure 3.37: Small incremental waveguide step for approximating a continuous taper.

change ΔZ. From the theory of transmission lines,

$$\Delta\Gamma = \frac{(Z + \Delta Z) - Z}{(Z + \Delta Z) + Z} \simeq \frac{\Delta Z}{2Z} \ . \tag{3.8}$$

As the step length $\Delta y \to 0$, Eq. 3.8 becomes an exact differential,

$$d\Gamma = \frac{dZ}{2Z} = \frac{1}{2}\frac{d}{dy}[ln(\frac{Z}{Z_\circ})]dy \ . \tag{3.9}$$

The total reflection Γ at $y = 0$ is found by summing all the partial reflections in the matching section of length L with their appropriate phases,

$$\Gamma = \frac{1}{2}\int_{y=0}^{L} e^{-2i\beta y}\frac{d}{dy}[ln(\frac{Z}{Z_\circ})]dy \ , \tag{3.10}$$

where β is the propagation constant.

The impedance function of a straight taper with constant width is defined as

$$Z = a(by + L) \tag{3.11}$$

where L is the length of the taper, a and b are constants. Applying the boundary conditions $Z(y = 0) = Z_\circ$ and $Z(y = L) = Z_L$, one obtains $a = Z_\circ/L$ and $b = Z_L/Z_\circ - 1$. Since the height (h_L) of the standard waveguide is twice the height ($h_\circ$) of the other waveguide, Z_L is two times $Z_\circ$. Substituting the impedance function into Eq. 3.10, the total reflection coefficient for the straight taper becomes

$$\Gamma = \frac{1}{2}\int_0^L \frac{e^{-2i\beta y}}{y + L} dy \ . \tag{3.12}$$

For each taper length L, the integral can be evaluated numerically by a mathematical software such as MATLAB [14]. From the numerical result in Fig. 3.38, one sees the expected behavior that the peaks of the reflection coefficient goes down as the taper length increases. To avoid large reflections (or mismatches) at low frequencies, the taper length should be an integer multiple of half guide wavelength.

3.3.3 Simulations of the S-parameters S_{11} and S_{21}

Broadband simulations were performed for the scattering parameters S_{11} and S_{21} to obtain the passband characteristics of the matching sections. This is possible in Mafia when the waveguide ports are homogeneously filled.

The procedure was to launch the first TE mode at the standard waveguide port, let it travels down the matching section and to record the time signals of the incident, reflected and transmitted waves. The TE_{10} was stimulated by a symmetric Gaussian shaped pulse with center frequency 805 MHz. The upper limit of the frequency range

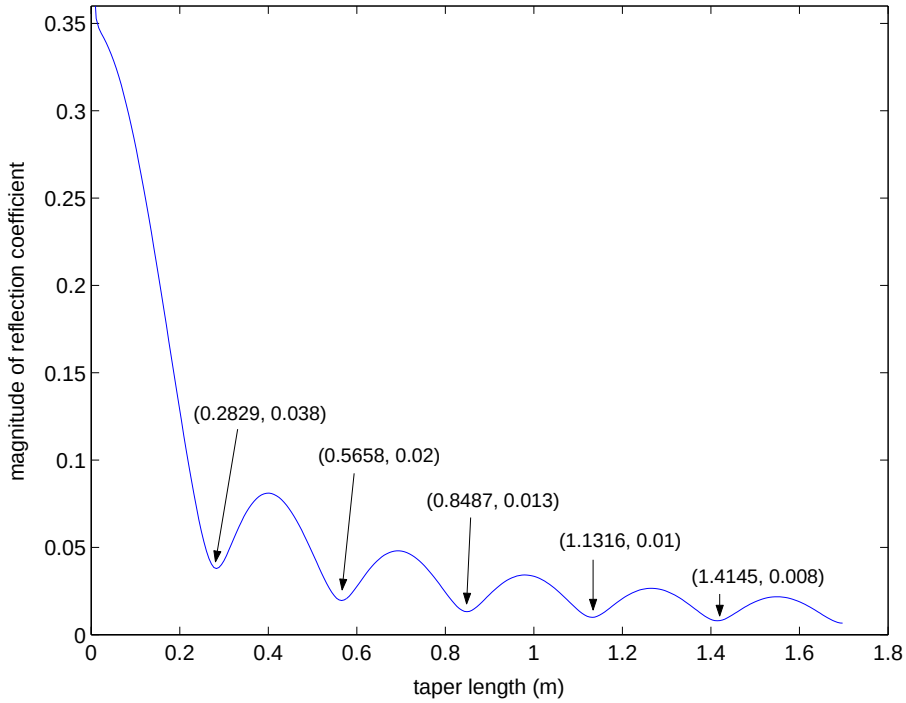

Figure 3.38: The approximate analytical solution of the reflection coefficient of the straight taper. The numerical integration is for the TE_{10} mode at 805 MHz and for a total taper length of 3 guide wavelengths. Minima occur at every half guide wavelength.

for the simulations is 1.4 GHz at which the excitation pulse is down by 60 dB. The maximum frequency was chosen to be about 200 MHz higher than the upper limit (1.211 GHz) of the TE_{10} passband because the results were noisy at the end of the frequency range. For the simulations, the frequency resolution was chosen to be 1 MHz. The total simulation time was typically 1 to 3 hours. A frequency resolution of 100 kHz gave similar results with a minor drop in the reflection coefficient, but with a significant increase in the simulation time.

After the time domain simulations, fast Fourier transforms were performed on the fields to find the spectra of the magnitude and phase of the scattering parameters.

The magnitude of S_{11} was calculated as the ratio of the spectrum of the reflected wave magnitude to the spectrum of the incoming wave magnitude. The calculation of S_{21} was likewise. For the straight taper, the reflection coefficient is plotted in Fig. 3.39. Note that the reflection coefficient at 805 MHz is close to the analytical

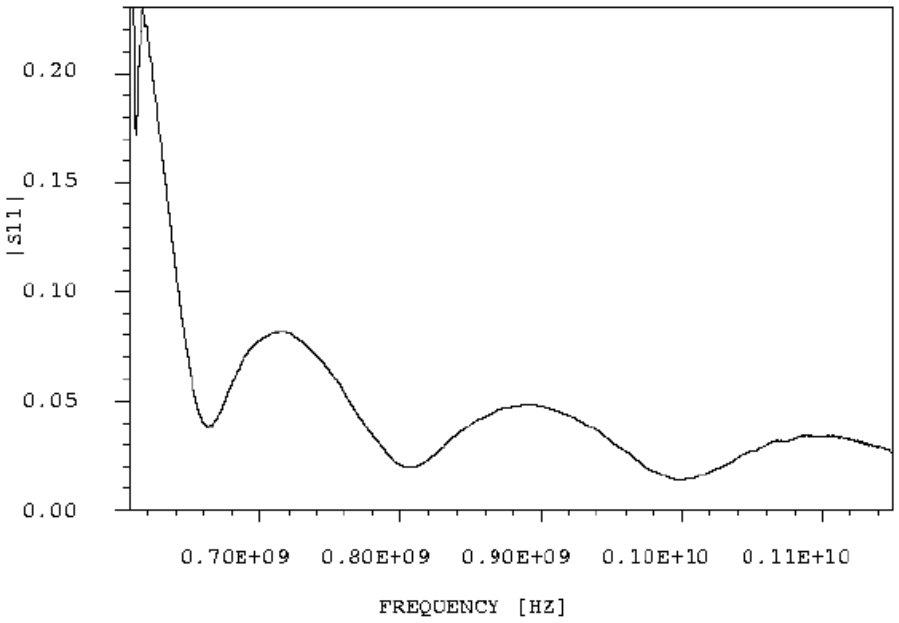

Figure 3.39: Magnitude of the reflection coefficient of the straight taper with a length of approximately one guide wavelength (0.5598 m). $|S_{11}|$ at 805 MHz is about 0.02.

result (second minimum) in Fig. 3.38. The difference in the taper lengths is about 6 mm and the reflection coefficients differ by 0.3%. The phases of the S-parameters are not important here as far as the passband characteristics of the taper is concerned. For the 1-section and 2-section quarter wave transformers, the reflection coefficients are shown in Figs. 3.40 and 3.41 Since the transmission curves contain no new informations, they won't be shown here. According to Figs. 3.39, 3.40 and 3.41, all three designs satisfy the design goals, *i.e.*, $|S_{11}| < 0.1$ at 805 MHz and a bandwidth

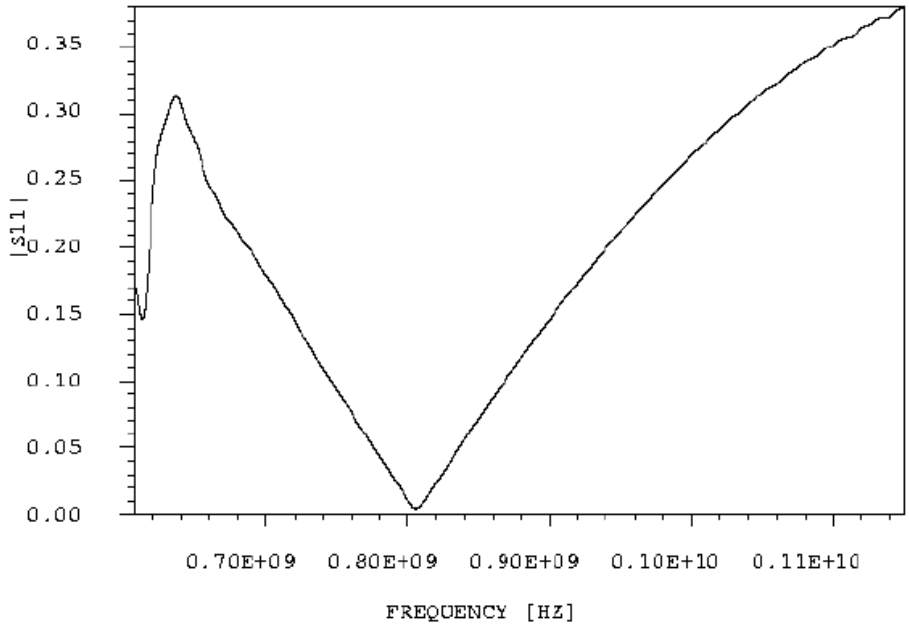

Figure 3.40: Magnitude of the reflection coefficient of the 1-section quarter wave transformer.

greater than 8.05 MHz. However, the quarter wave transformers have lower reflection coefficients and wider bandwidths than the straight taper. The main advantage of adding an extra section to the quarter wave transformer is to increase the bandwidth.

To check the Mafia results, the 1-section quarter wave transformer, as an example, was simulated by a different code (Ansoft HFSS version 6.0.12) [15]. This code is a finite element code which is different in nature from that of Mafia. The difference in the magnitude of the reflection coefficients between the two codes is 0.0005 at 805 MHz, which is insignificant. The bandwidths are similar in both cases.

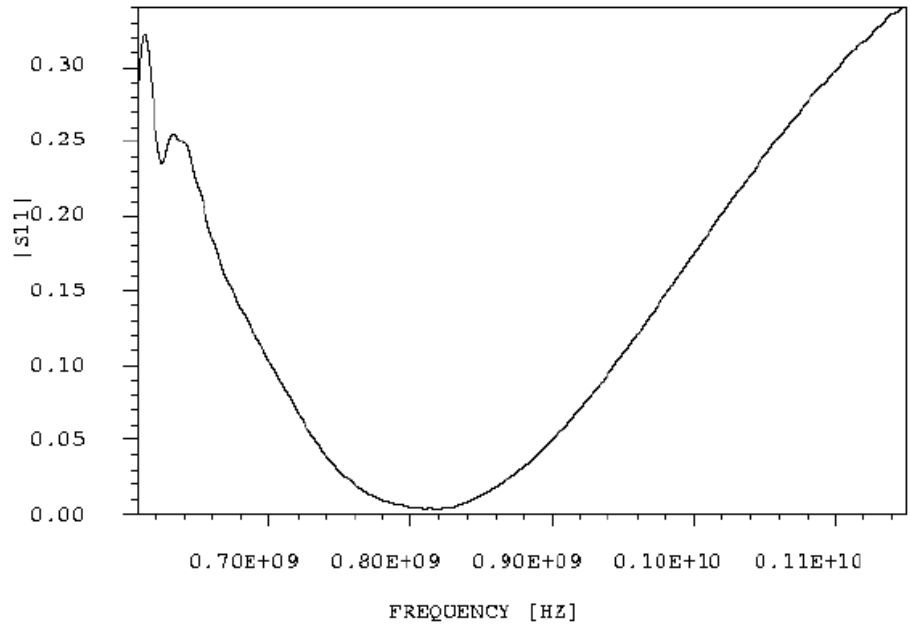

Figure 3.41: Magnitude of the reflection coefficient of the 2-section quarter wave transformer.

3.3.4 Specifications of the straight taper and the quarter wave transformers

The dimensions and the passband characteristics of each design are summarized in table 3.13 through 3.16. The widths of all tapers are 24.765 centimeters and the

Table 3.13: Dimensions and passband characteristics of the straight taper.

Length (cm)	Frequency (MHz)	$\|S_{11}\|$	Bandwidth (MHz)
55.984	804.950	0.017	19

bandwidths are calculated at the points where $|S_{11}|$ reached 2%. Finally, the straight taper was chosen because of its lower cost and ease of fabrication.

Table 3.14: Dimensions and passband characteristics of the 1-section quarter wave transformer.

Length (cm)	Height (cm)	Frequency (MHz)	$\|S_{11}\|$	Bandwidth (MHz)
13.272	8.755	805.020	0.004	25

Table 3.15: Dimensions of the 2-section quarter wave transformer.

	Length (cm)	Height (cm)
1st section	13.122	7.296
2nd section	13.622	10.319

Table 3.16: Passband characteristics of the 2-section quarter wave transformer.

Frequency (MHz)	$\|S_{11}\|$	Bandwidth (MHz)
804.958	0.004	100

Chapter 4

Low Power Test

The first tests performed on the MUCOOL 6-cell cavity were low power test. These were done on a full scale aluminum model (Fig. 4.1) in the A0 area of Fermilab. The

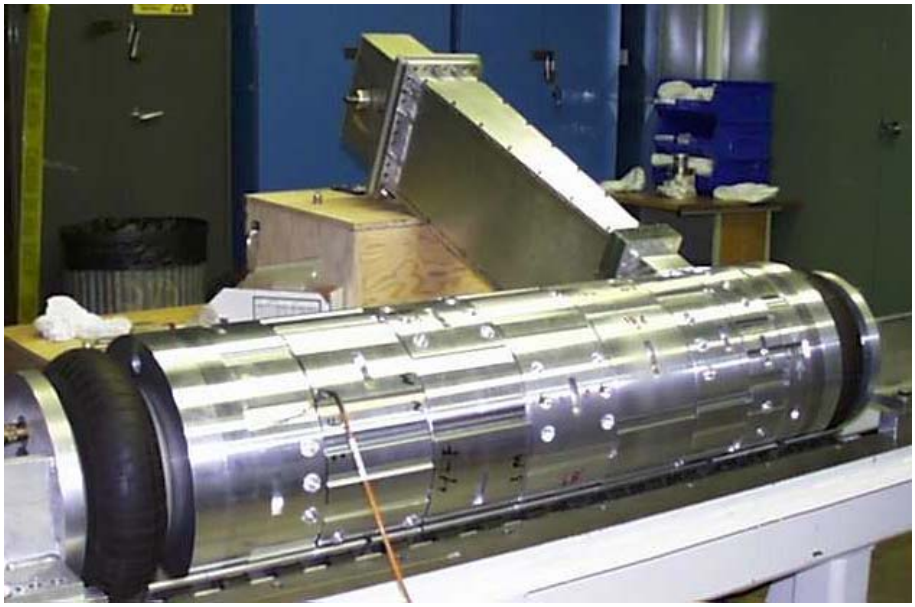

Figure 4.1: The full scale aluminum model of the 6-cell cavity system.

goals of the test were to check the simulation results and the machining accuracy, and to develop a tuning procedure for the copper cavity. The mode spectrum, the quality

factor, the external coupling coefficient, and the electric field profile were measured and compared to the simulation results. After the aluminum model tests, the copper cavity was fabricated to final dimensions and any subsequent deviations from design goals were corrected by fine tuning the cavity.

The aluminum cavity and the end cells of the copper cavity were made at the Fermilab machine shop, and the rest of the copper cavity was machined at the Walco machine shop in Lockport, Illinois. The cavity was fabricated into 5 pieces of two-half cell. The end cells were made into half cells and one center piece involving the coupling slot. The drawing in Fig. 4.2 shows the partitions of the cavity (in which they

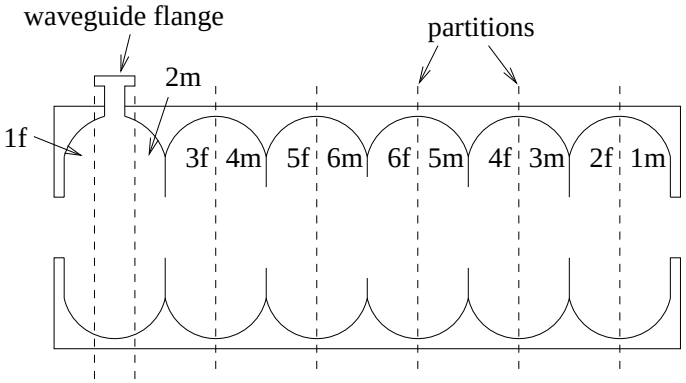

Figure 4.2: Partitions of the 6-cell cavity in which the cavity pieces were made. The connections between cavity pieces are in the form of step joints. The letters f and m designate female joint and male joint respectively.

were made) and their designations. The picture in Fig. 4.3 shows an actual two-half cell piece. Notice that there are six dimples at the outer cavity wall. These were for cavity fine tunings. There are six more dimples on the opposite side. However, for the aluminum prototype, tuning was done by removing (*i.e.*, machining) material from the interior walls of the cavity. The channels that run longitudinally along the outer

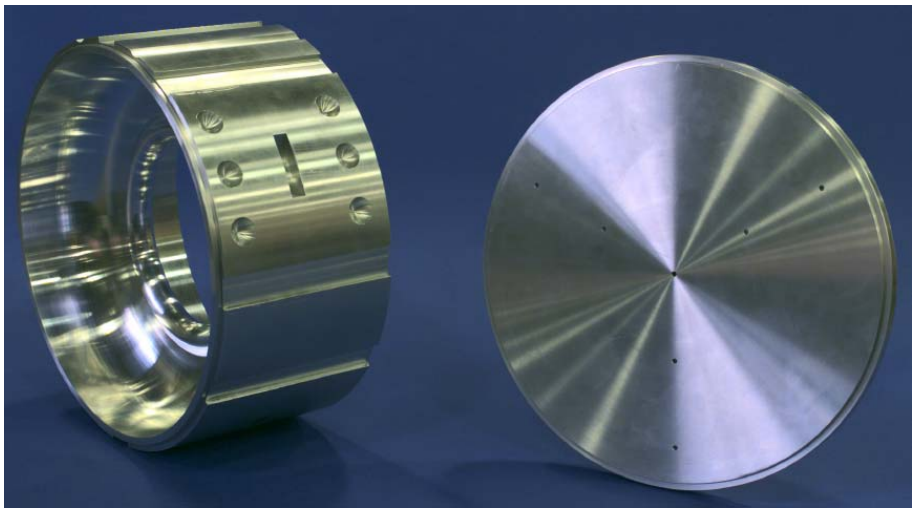

Figure 4.3: A two-half cell of the aluminum test cavity (left) and a shorting plate (right). The center hole on the shorting plate was for bead pull measurements (*i.e.*, electric field profile measurements). The other holes were not used.

cavity wall were for cooling pipes. The shorting plate in Fig. 4.3 was for measuring the RF properties of the two-half cell pieces. The center hole on the shorting plate was for bead pull measurements (*i.e.*, electric field profile measurements). The other holes were not used. The material of the aluminum model is Al 6061-T6. The electrical conductivity of the material is $2.5 \times 10^7 (\Omega m)^{-1}$.

To account for possible machining and simulation uncertainties, the coupling cell of the aluminum model was made with 50 mil of extra material at its interior surface, while the other cells with 10 mil of extra material. The extra material in the coupling cell was used to compensate the frequency decrease due to the coupling aperture. All irises were machined to design dimensions, *i.e.*, no extra material. After testing and tuning, a final machine cut was applied to every cell to bring the cavity to the design frequency.

4.1 Experimental Apparatus

The main measuring instruments were: (1) the Hewlett Packard 8753C network analyzer and the 85046A S-parameter test set which were used for RF property measurements, and (2) the bead pull set for cavity electric field measurements. The auxiliary devices included the Kalmus 706FC wide-band RF power amplifier, the hand-made electric and magnetic probes, and the cavity support stand. The schematics of the experimental setup is shown in Fig. 4.4.

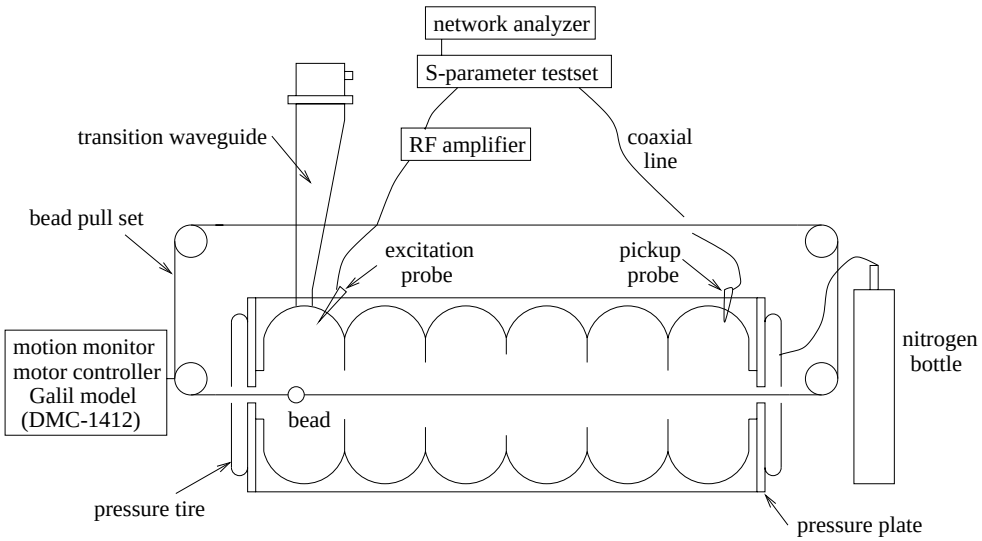

Figure 4.4: Schematics of the low power test setup.

In order to make good RF contacts between the cell pieces for the measurements, the ensemble of the cell pieces were pressurized at both ends. The aluminum cavity was pressed at 75 psi by compressed dry nitrogen from the nitrogen bottle. Higher pressures were possible, but experiments showed that 75 psi was sufficient to produce consistent readings of the cavity Q values. For the copper cavity, compressed air at

a lower pressure of 45 psi was used to avoid damaging the contact edges between the cell pieces. Because of the weaker RF contacts between the cell pieces, lower Q value for the copper cavity was expected in the low power test than would be achieved in the final brazed cavity.

For the measurements of the electric field profile, the properties of the bead pull string and the bead were chosen carefully not to induce frequency perturbations that were larger than the bandwidth of the cavity mode. The bead pull string was very thin (a few 0.1 millimeter) and its material was nylon. Both metallic (brass) and dielectric (plastic like) spherical beads of diameter 0.184 inches were used in the measurements.

4.2 Environmental Conditions

The mode frequencies of the cavity depend on the ambient atmospheric conditions. The temperature fluctuation would expand or contract the cavity causing a frequency change that was proportional to the linear coefficient of thermal expansion of the cavity material. Inside the cavity volume, changes in humidity would alter the dielectric constant, which in turn cause changes in the frequency. For future high power test, the operating conditions would be vacuum and stable temperature (maintain by water cooling). Thus, the measured frequencies needed to be corrected to the case of vacuum and constant temperature. During the measurements, the room temperature T (°C), the barometric pressure of air P_b (mbar), and the relative humidity H_r (%) were recorded for frequency corrections.

The following methodology taken from the Fermilab linac upgrade was used for the frequency correction. As a function of temperature, the vapor pressure of water P_v was found from the empirical fit to data taken from the CRC handbook,

$$P_v = 5.7232e^{[(0.053546T)+1.6878+0.23539(T-24)+0.00544721(T-24)^2]}. \tag{4.1}$$

The partial pressures of water P_w and of dry air P_a are

$$P_w = \frac{H_r}{100}P_v \tag{4.2}$$

and

$$P_a = P_b - P_w. \tag{4.3}$$

The dielectric constant κ expressed in terms of the various pressures and the temperature is

$$\kappa = 1 + 210 \times 10^{-6}(\frac{P_a}{T_k}) + 180 \times 10^{-6}(1 + \frac{5580}{T_k})(\frac{P_w}{T_k}), \tag{4.4}$$

where T_k is the temperature in unit of Kevin. In terms of the above quantities, the corrected frequency in vacuum at 25°C is

$$f_{cor} = f\kappa^{1/2}[1 + \alpha(T - 25°C) \times 10^{-6}], \tag{4.5}$$

where f is the measured frequency and α is the linear coefficient of thermal expansion.

The device for measuring the pressure was the mechanical Aneriod barometer which also has a temperature scale. For relative humidity measurements, the Hanna Instrument HI 8565 stick hygrometer was used. The devices read out in units of 1°C, 1 mbar and 0.1%, respectively. During the course of a single measurement, which lasted anywhere from a few minutes up to 20 minutes, there were no noticeable

fluctuations in the temperature and the pressure. The changes in the relative humidity were usually at the 0.5% level. Given the typical range of frequency corrections, *i.e.*, 110 to 180 kHz, the errors in f_{cor} due to the random uncertainties in the temperature, the pressure and the relative humidity readings were insignificant.

4.3 Characterization of Cavity Modes

4.3.1 Mode Spectrum and Q Measurements

The technique for measuring the mode spectrum and the quality factor was the transmission S_{21} measurement. Using magnetic probes, the cavity was excited in an end cell and the transmitted signal was pickup in the opposite end cell. The probes were inserted at the outer walls of the end cells. The loops of the magnetic probes were oriented perpendicular to the magnetic fields (*i.e.*, parallel to the cavity axis) to obtain the best couplings to the fields. The presence of the probes in the cavity inevitably perturbed the quantities that we were trying to measure. Therefore, for accurate results, the probes were inserted into the cavity just enough to excite the modes.

Measurements were done first on the individual cell pieces (1m through 4m in Fig. 4.2) to check their frequencies and to determine the discrepancy between simulations and measurements. The measurements in table 4.1 shows that the average frequency discrepancy between the measurements and the simulations is about 600 kHz, and the spread among the frequency measurements is less than 200 kHz. The frequency discrepancy is within the variations observed in the simulated frequencies with different meshes. The variations due to mesh choice range from a few hundreds kHz to one MHz. All the frequencies are higher than 805 MHz. This is because the

Table 4.1: Measured frequencies of the aluminum two-half cell pieces.

Cavity Piece	Measured Frequency (MHz)	Simulation Frequency (MHz)
1m	806.595	none
2f3m	806.559	806.015
4f5m	806.608	805.757
6f6m	806.408	806.258
5f4m	806.512	805.757

cell pieces have a radius that is 10 mil smaller than the design.

The spectra of the TM_{010} passband and the loaded Q of the π mode for the 6-cell cavity are shown in Figs. 4.5 and 4.6, respectively. In both figures, the magnitude

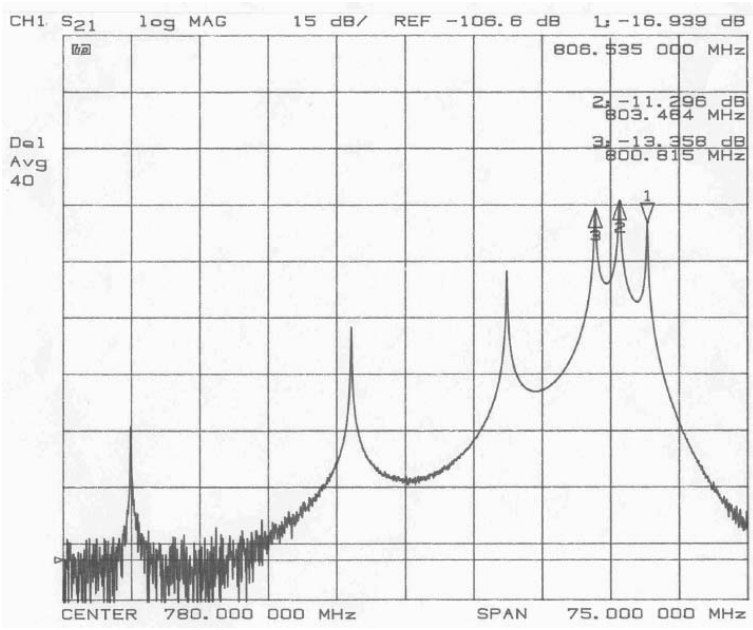

Figure 4.5: Spectra of the TM_{010} passband of the aluminum cavity. The right most peak (marker 1) is the π mode.

of the transmission coefficient S_{21} is plotted as a function of frequency. The peaks in

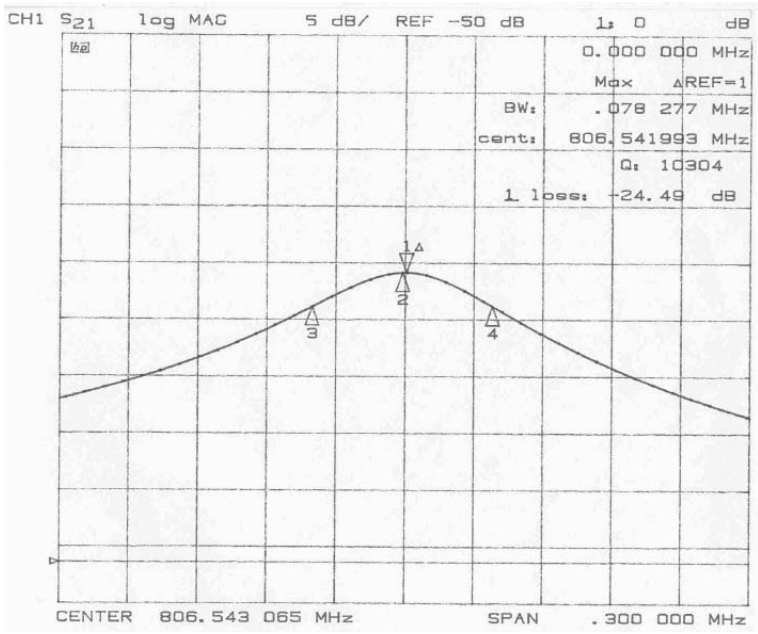

Figure 4.6: The Q_L measurement of the π mode of the aluminum cavity at the 3 dB bandwidth.

the spectra indicate the resonances, *i.e.*, the maximum transmissions of the excitation frequency components that match the cavity modes. By zooming into a particular mode, for example the π mode (the right most peak in Fig. 4.5) as shown in Fig. 4.6, one could determine the frequency, the Q and the bandwidth of the mode. The π mode frequency, corrected by the atmospheric conditions, is 806.542 MHz. It is about the average of the measurements of the individual cell pieces (according to the measurements in table 4.1). This indicates that the effects of cell to cell couplings on the π mode frequency is small, at most 100 kHz. The Q_L value (equals $f_o/\delta f$) is 10304 at the 3 dB bandwidth (δf) of 78 kHz. At critical coupling, the unloaded Q is 20608, twice that of the loaded Q. It is slightly lower than the simulation value of 21300. This maybe due to the imperfect RF contacts between the cavity pieces.

Note that the aluminum cavity has lower Q value than the copper cavity because of aluminum's higher resistivity.

The passband modes can be displayed in a dispersion diagram (a plot of frequency vs. phase advance in a cell). For a N-cell cavity, the phase advance per cell is calculated as $\phi_c = (n-1)\pi/(N-1)$ where $n = 1, 2 \ldots N$. The measurement and the simulation results are plotted in Fig. 4.7. They agree within 1 MHz of each other.

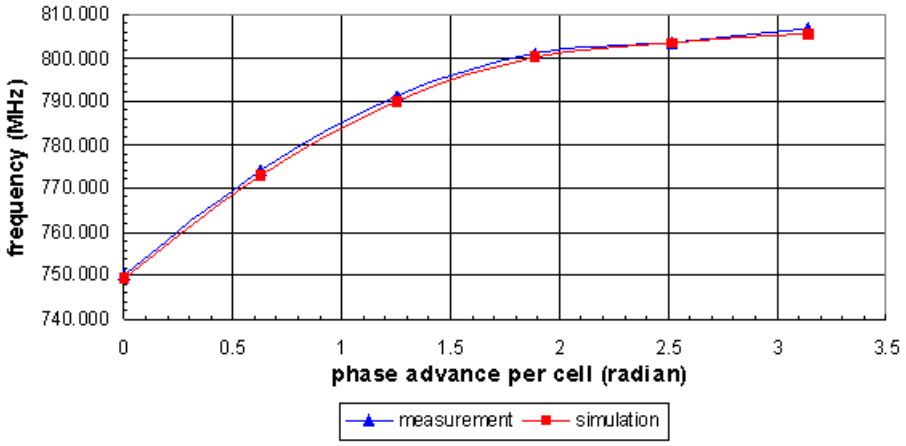

Figure 4.7: Dispersion relation of the TM_{010} passband of the 6-cell aluminum cavity.

At this point, it is worthwhile to discuss the uncertainties in the frequency measurements. During a typical measurement, the frequency varied by a few kHz. Presumably, this could be caused by the fluctuations in the surrounding atmospheric conditions or by the noise in the electronics. Anyhow, a few kHz frequency fluctuation is unimportant. However, day to day measurements of the same mode showed a 10 to 20 kHz variation in the frequency. The source of these frequency variations was possibly due to the small variations in the amounts of probe insertion and orientation between the daily measurements. The loaded Q measurements were very sensitive to

the oxidation on the cavity surface, the end plate pressures and the coupling strengths of the probes to the cavity modes. The solutions to these problems were to clean the cavity surface well with alcohol before measurements, to apply sufficient end plate pressures and to have minimum probe couplings (or probe insertions).

4.3.2 Electric Field Profiles

Introducing an obstacle into a metallic enclosure will perturb the resonant frequency by an amount depending on the local electric and magnetic fields. This fact is expressed in the Slater perturbation theorem [16],

$$w^2 = w_\circ^2(1 + \int (H_u^2 - E_u^2)dv) \ , \tag{4.6}$$

where w is the perturbed frequency, $w_\circ$ is the unperturbed frequency, and H_u and E_u are the normalized magnetic and electric fields in the unperturbed cavity. (H_u and E_u are normalized so that the integral of H_u or E_u over the cavity is unity.) The integral is taken over the volume occupied by the obstacle. Experimentally, by moving an obstacle through the cavity, one can map out the field strength. This was done by the bead pull setup shown in Fig. 4.4.

The application of the Slater perturbation theorem to a spherical bead of relative permittivity ϵ_r and permeability μ_r showed that the fractional frequency deviation [17] is

$$\frac{\delta w}{w_\circ} = -\frac{3v}{4U_T}(\frac{\epsilon_r - 1}{\epsilon_r + 2}\epsilon_\circ E^2 + \frac{\mu_r - 1}{\mu_r + 2}\mu_\circ H^2) \ , \tag{4.7}$$

where v is the volume of the sphere, U_T is the total stored energy in the cavity, E and H are the local electric and magnetic fields at the sphere relative to the average field

in the cavity, respectively. The perturbation equation is not valid for bead that is close to the metallic surface because of the image charge effects. In this experiment, only the data near the cell centers were used for comparison with the simulations.

The measurement technique for the electric field profiles was the S_{21} phase measurement. The phase perturbation of the transmission coefficient was recorded as the bead passed through the cavity. As an example, the bead pull result of the π mode is shown in Fig. 4.8, where the phase perturbation of the transmission coefficient is

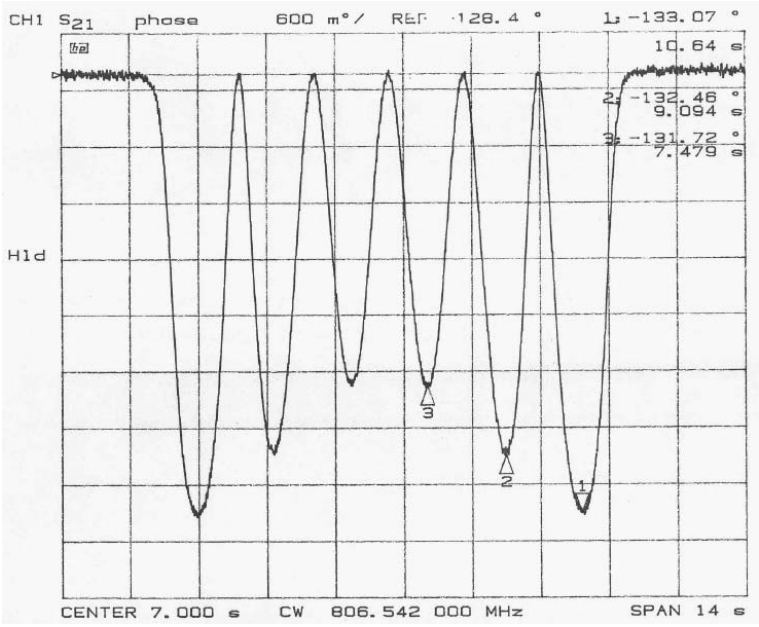

Figure 4.8: The phase perturbation of the transmission coefficient as a function of time for the π mode (the sixth mode in the TM_{010} passband). It is proportional to the square of the on-axis electric field (E^2).

plotted as a function of time. The field profile was for a coupling slot width of 3.23 inches, the case closest to critical coupling in the simulation. In the measurement, the coupling cell was slightly out off tune, as indicated by the field asymmetry in the

end cells. The tuning of the field profile was done by the insertion of a dielectric rod into the coupling cell. This lowered the frequency by 28 kHz. The field strength was calculated as

$$E = \sqrt{\frac{\delta\phi}{\delta\phi_\circ}}\ , \tag{4.8}$$

where $\delta\phi$ is the recorded phase perturbation and $\delta\phi_\circ$ is the reference (normalization) phase. The fields were normalized to those of the middle cells. Disagreement between measurements and simulations, shown in table 4.2, are about 1%.

Table 4.2: Bead pull and simulation electric field data for the aluminum cavity.

Cell	1	2	3	4	5	Coupling
Measurement	1.186	1.106	1.000	1.000	1.103	1.191
Simulation	1.176	1.108	1.000	1.000	1.108	1.176

The bead pull results of a few other modes in the TM_{010} passband are shown in Figs. 4.9, 4.10 and 4.11. As one can see, the field distributions of these modes are highly irregular among the cells. Some cells have negligible fields. These modes are not suited for effective beam accelerations. The disagreements with simulations are from 4 to 8 percents. The first two modes of the passband are not shown here because their signals are very noisy.

The accuracy of the field measurements depended mainly on two factors: (1) mechanical stabilities of the cavity and the bead pull systems, and (2) the error in positioning the bead. The mechanical vibrations of the cavity support structure and the bead pull string due to human handling and the surrounding machine operations introduced noise and shift into the phase signals. The measurements were to be

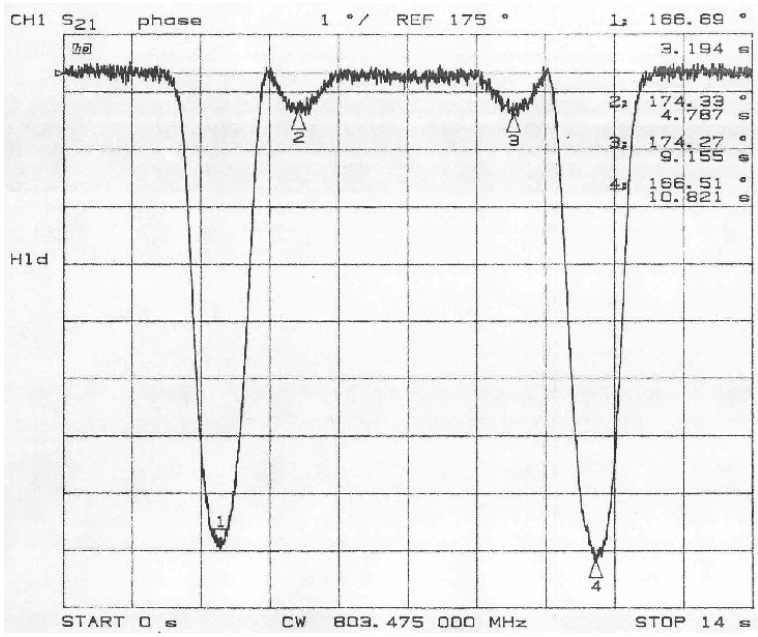

Figure 4.9: On-axis E^2 of the fifth mode in the TM_{010} passband.

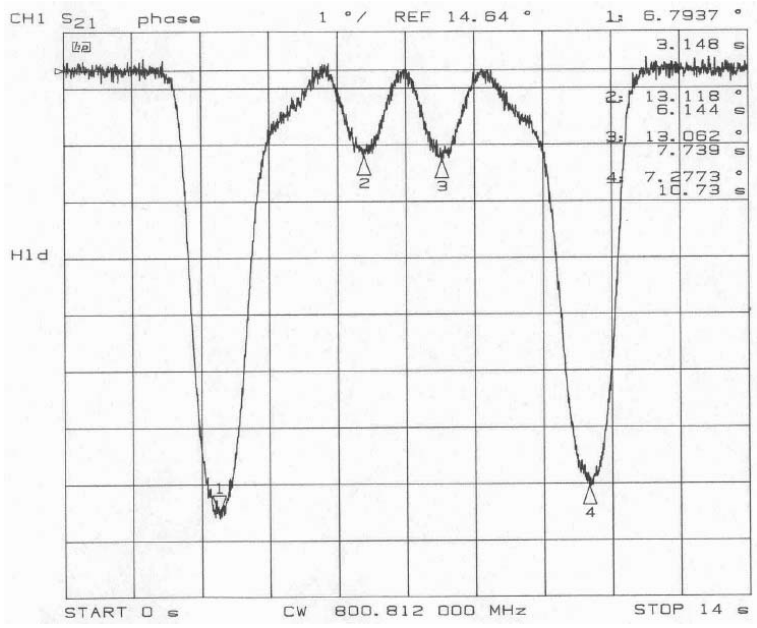

Figure 4.10: On-axis E^2 of the fourth mode in the TM_{010} passband.

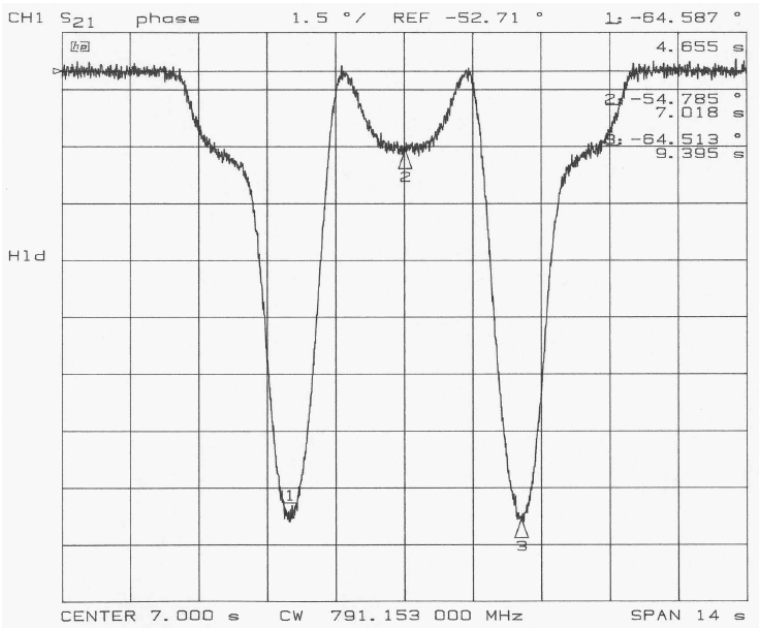

Figure 4.11: On-axis E^2 of the third mode in the TM_{010} passband.

taken when the signal of the transmission phase was steady and flat. The centering of the bead pull string or bead on the cavity axis was done by ruler and eyes. The positioning error was about 1 millimeter.

For the π mode, the measurement error in the field due to the noise in the signal is estimated as follows. Propagation of random errors in Eq. 4.8 yields

$$\frac{\delta E}{E} = \frac{1}{2}\sqrt{\left(\frac{\Delta(\delta\phi)}{\delta\phi}\right)^2 + \left(\frac{\Delta(\delta\phi_\circ)}{\delta\phi_\circ}\right)^2}\,. \tag{4.9}$$

The noise in the phase signal is typically between 0.3 and 1 degree. This gives one to two percent fractional error in the field measurements.

4.3.3 Machining of the Copper Cavity

With the knowledge of the frequency discrepancy between the simulations and the measurements, and the good agreement in the field measurements, the dimensions of the copper cavity could be predicted with good accuracy. According to the measurements (as indicated by the spread in the frequency measurements), the maximum amount of frequency tuning for the copper cavity should be less than a few hundreds kHz. This could be easily handled by the dimples at the outer wall of the cavity. Thus, elaborate tuning procedure for the copper cavity was not needed. The copper cavity pieces would be machined to a target frequency of 804.925 MHz. The frequency was made lower than 805 MHz because fine tuning using the dimples could only increase the frequency.

4.4 Measurement of the External Coupling of the Cavity

The external coupling of the π mode was studied by measuring the coupling coefficient β for a series of slot widths of the coupler. Since the aluminum cavity has different conductivity from that of the copper cavity, the requirement on its coupling coefficient is not the same as copper cavity. As defined previously (Eq. 3.1), β is the ratio of unloaded Q to external Q. For two identical cavities of the same coupler dimensions but different conductivities, their β's are related by

$$\beta_{Al} = \beta_{Cu} \frac{Q_{\circ}^{Al}}{Q_{\circ}^{Cu}} \tag{4.10}$$

where Al and Cu denote aluminum and copper, respectively. Simulation has shown that $Q_\circ^{Cu} = 1.643 Q_\circ^{Al}$. In order to have $\beta_{Cu} = 1$ for the copper cavity, β_{Al} must equals 0.608.

The coupling coefficient was measured by performing reflection S_{11} measurement using the experimental setup shown in Fig. 4.12. The structure was excited at the

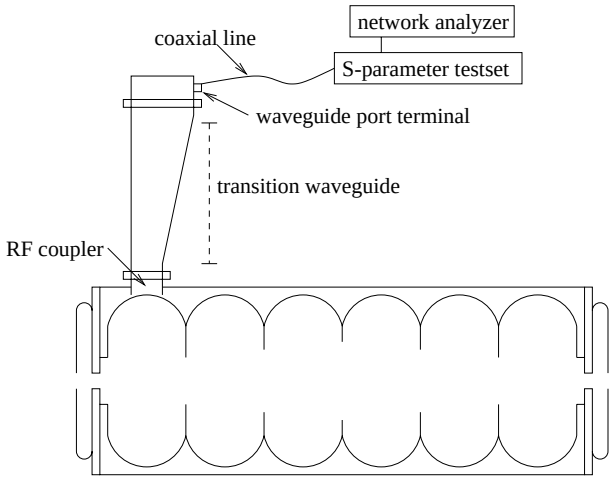

Figure 4.12: Schematics of the experimental setup for external coupling measurements.

waveguide port terminal. In order to measure the reflection coefficient at the terminal plane, the coaxial cable was calibrated at its end (away from the network analyzer) with a short, open and load connectors (Hewlett Packard 85032B type N calibration kit).

The reflection coefficient measurements are expressed in the Smith chart format. Figure 4.13 shows an example of such a measurement. The circle labeled by the markers 1 and 2 is called the resonance circle, which is a locus of reflection coefficient

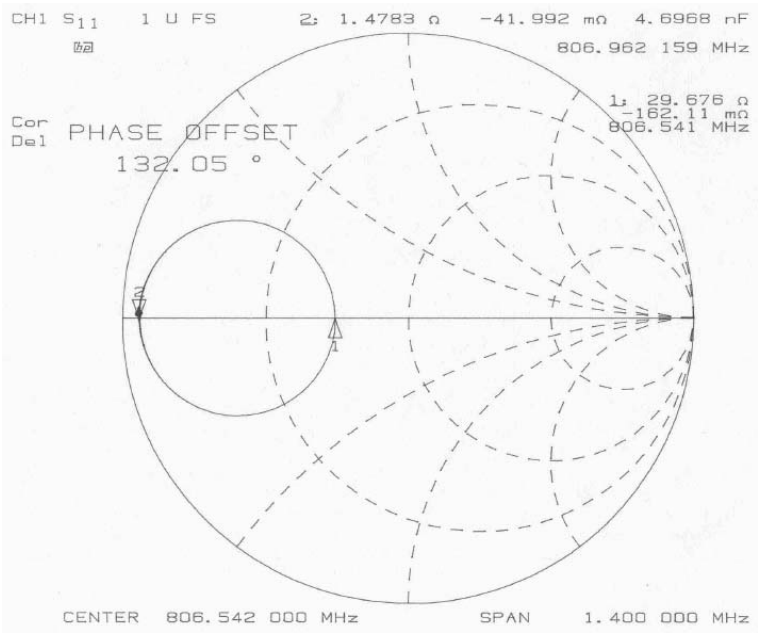

Figure 4.13: An example of reflection coefficient measurement using Smith chart. The coupling slot width is 3.23 inches. The solid circle labeled by markers 1 and 2 is the resonance circle. The point at marker 1 is the reflection coefficient of the π mode.

points at the various frequencies[1] scanned by the network analyzer. The point at marker 1 is the reflection coefficient of the π mode. For a resonance circle centered on the horizontal axis, the coupling coefficient is $\beta = r/50\ \Omega$, where r is the real (resistive) part of the impedance for the π mode, and 50 Ω is the impedance of the coaxial line at the waveguide port terminal. When $r = 50\ \Omega$, one has the matching condition (no reflection from the cavity). The measured and simulated β's of 0.594 and 0.584, respectively, are within 2% of each other.

The measurement and simulation results of the coupling coefficient for several cases of slot width are plotted in Fig. 4.14. The measured coupling coefficients were

[1]The center frequency of the measurement was the π mode frequency. To get a complete resonance circle, a frequency span of 1.4 MHz was used.

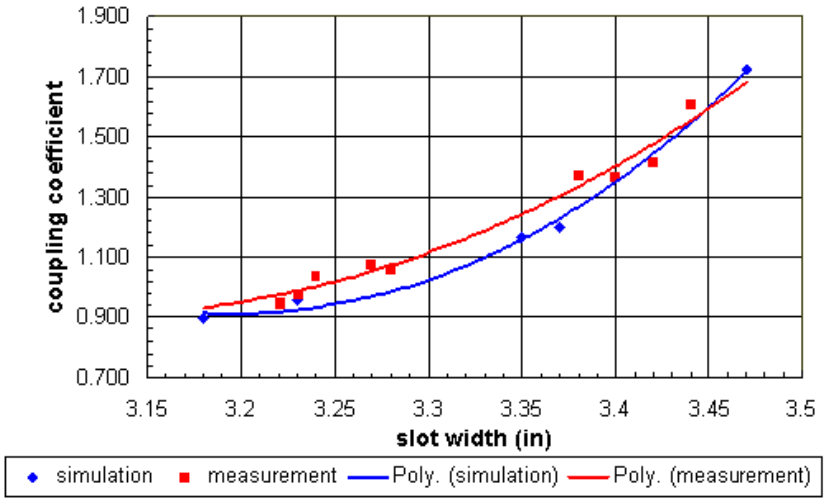

Figure 4.14: The measurements and simulations of the coupling coefficient.

translated to those of copper cavity by Eq. 4.10. The maximum disagreement between the simulation and the measurement is less than 10%. The disagreement is possibly due to the fact that the measured electric field profiles were not perfectly in tune, whereas in the simulations, the electric field profiles were in tune[2]. Finally, the width of the coupler for critical coupling was chosen to be 3.22 inches for the copper cavity.

4.5 Copper Cavity

After the aluminum model test, the copper cavity was fabricated with OFHC (oxygen free high conductivity) copper and undergone a series of processing steps. The target frequency of the cavity was 804.925 MHz. The cells of the copper cavity (Fig. 4.15) were machined with larger cell radii[3] than the original design dimensions because the

[2]This is a source of disagreement between the measurements and the simulations because the coupling coefficient depends on the field level in the coupling cell. Stronger field level in the coupling cell would give larger coupling coefficient.

[3]Final cavity dimensions are in chapter 3.

Figure 4.15: The brazed copper cavity.

simulated frequency (on the average) was 600 kHz lower than the measurements. After machining, the frequencies of the individual cell pieces were first checked for accuracy. Then they were chemically treated in a clean room in preparation for brazing. After brazing, the RF properties of the cavity were checked, and if necessary, fine tuning could be done to correct deviation from the design goal.

4.5.1 Measurements of the Two-Half Cells

The frequencies of the two-half cell pieces and the coupling cell are presented in table 4.3[4]. For the measurement of the coupling cell (3f2m1f), the transition waveguide

Table 4.3: Frequencies of the two-half cells of the copper cavity.

Cavity Piece	1m	2f3m	4f5m	6f6m	5f4m	3f2m1f
Frequency (MHz)	805.072	804.964	805.058	805.040	805.051	804.988

[4]The meanings of the cell labels are shown in Fig. 4.2.

was attached to the coupler. According to the data, the maximum deviation from the target frequency is about 150 kHz. This is consistent with the frequency spread (about 200 kHz) observed in the aluminum cavity measurements. The data indicates that the π mode frequency of the 6-cell cavity would be within 70 kHz of 805 MHz. After the RF properties of the individual cell pieces were checked, chemical cleaning of the cavity was undertaken.

4.5.2 Chemical Cleaning and Brazing

The performance of the cavity under high power depends critically on the quality of the interior RF surface of the cavity. A smooth and clean surface greatly reduces surface electron emission and lowers the risk of surface breakdown. Since electron emission extracts (or wastes) energy from the cavity, lower emission means higher achievable accelerating gradient. Therefore, it is important to have the cavity as clean as possible.

In the A0 clean room, the cavity was: (1) degreased in a warm base solution of 2% Micro and purified water, (2) chemically etched in a warm acid solution of 2% Citronax and purified water and (3) rinsed in purified water. Both steps 1 and 2 were about 15 minutes long. Step one removed oily material that fell on the surface during machining and the finger prints. Chemical etching removed the oxides from exposure to atmospheric conditions, and the other surface contaminants. Because of the small amount of Citronax used and the short etching time, the frequency change due to the removed surface layer was negligible. The three step process was repeated until the cell pieces were visually clean. After the chemical treatments, the cell pieces were

quickly cleaned with alcohol and blow dried with dry nitrogen. Figure 4.16 shows the picture of a clean cell piece. Finally, the cell pieces were sealed in air depleted plastic

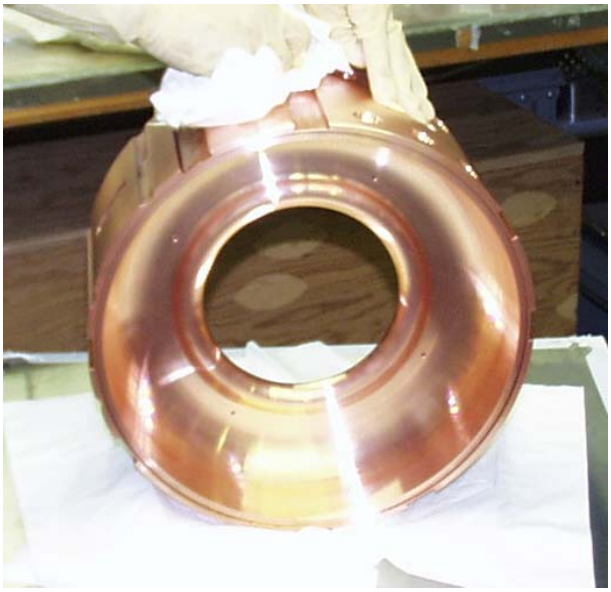

Figure 4.16: A copper cell piece after chemical cleaning.

bags.

The cavity was sent to the company Alpha Braze of Bodycote Inc., in California for brazing. Inside a high temperature furnace purged with hydrogen, the cavity went through a series of brazing process. The brazing materials used for the beam pipes and the waveguide flange at the coupler were gold and copper; silver and copper were used for the cavity pieces. Brazing started with the beam pipes and the waveguide flange at a temperature of 1905°F. Then the cavity pieces were brazed at 1500°F. The high temperature furnace environment provided additional cleaning to the cavity by evaporating many deposits of dirts off the cavity surface.

4.5.3 Measurements of the Brazed Cavity and Fine Tuning

The π mode frequency, quality factor, coupling coefficient and electric field profile of the copper cavity were measured after brazing. To prevent oxidation from exposure to air, the cavity volume was filled with dry nitrogen during measurements. Thus, frequency correction for atmospheric conditions was not performed. The measurements (before any fine tuning) are plotted in Figs. 4.17, 4.18 and 4.19. The experimental

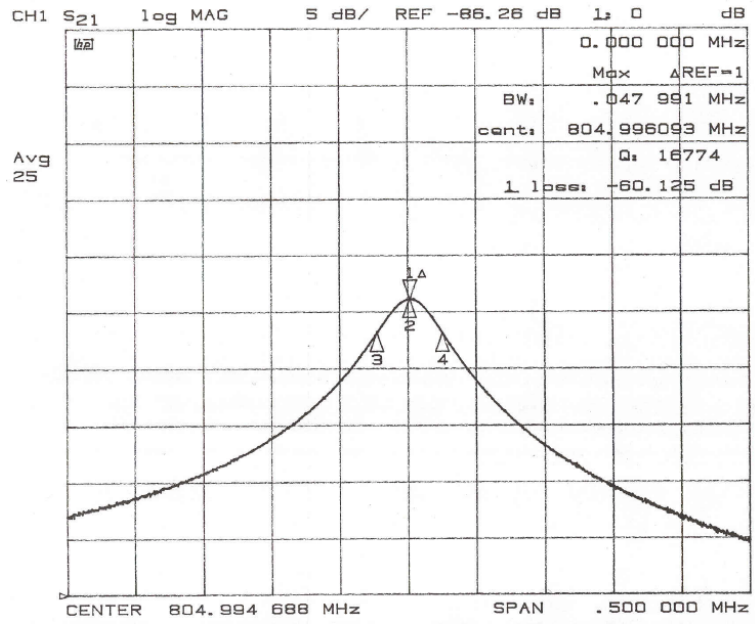

Figure 4.17: The π mode frequency and Q of the brazed copper cavity before tuning.

results and their disagreements with the design are summarized in tables 4.4 and 4.5.

For the measured coupling coefficient, less than 0.1% of the incident power was reflected. Thus, a 5% discrepancy in the coupling coefficient is unimportant. The field measurement shows an asymmetry in the field profile due to the 6% disagreement in the coupling cell. Fine tuning was needed to bring the field profile to agreement with

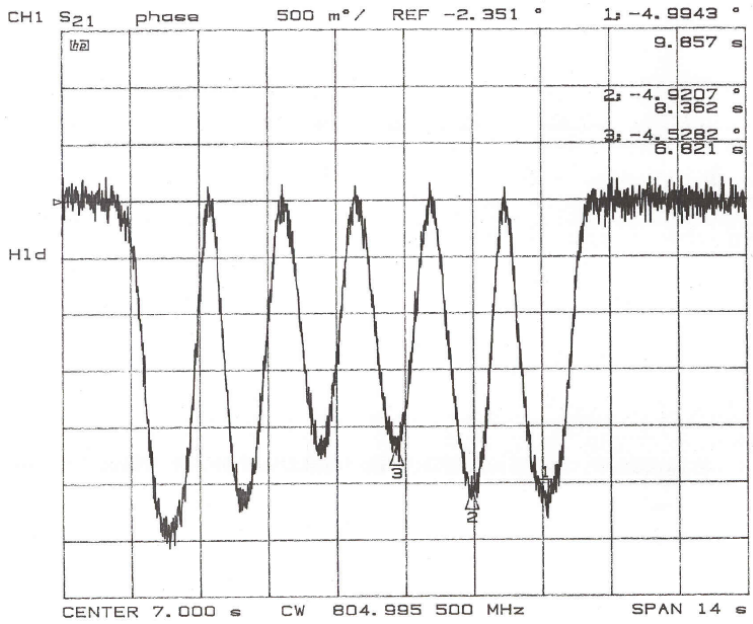

Figure 4.18: E^2 of the brazed copper cavity before tuning. The field in the coupling cell is on the right.

Table 4.4: RF properties of the brazed copper cavity before tuning. The plus sign means higher than design values.

	Frequency (MHz)	Q_o	Coupling Coefficient
	804.996	33548	1.053
Disagreement	negligible	+2%	+5%

Table 4.5: Electric field profile of the brazed copper cavity before tuning. The fields are normalized to the middle cells 3 and 4. The minus sign means lower than design values.

Cell	1	2	3	4	5	Coupling
$\|E\|$	1.156	1.093	1.000	1.000	1.086	1.102
Disagreement	-2%	-1.5%	none	none	-2%	-6%

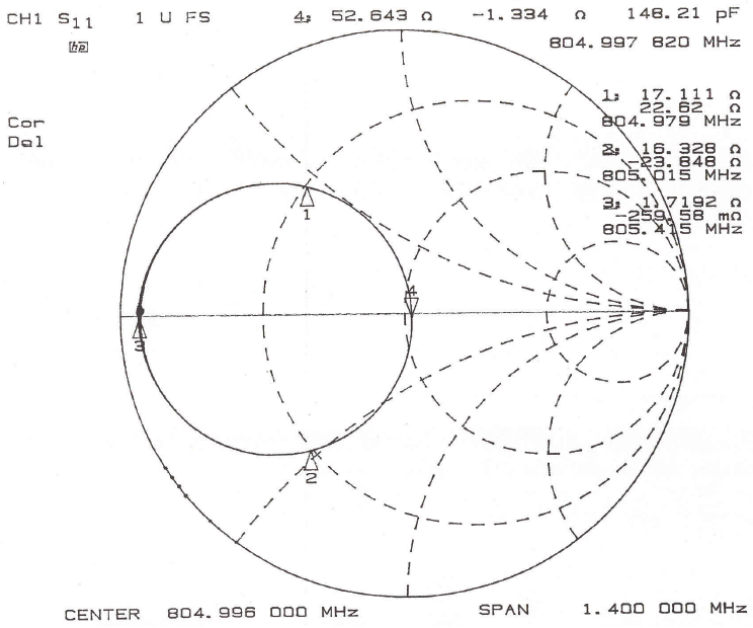

Figure 4.19: Coupling coefficient of the brazed copper cavity before tuning. Marker 4 is the reflection coefficient of the π mode.

the design distribution at the 1% level.

In general, cavity tuning refers to making fine alterations of the cavity geometry to correct frequency and field deviations. It is basically an iterative experimental process. The tuning procedure is as follows. First, a bead pull measurement identifies the cell with the largest field deviation that is at the low side with respect to the design distribution. Then its field is raised by striking the dimples at its outer cavity wall with a steel stick. At the same time, one monitors the frequency change. Once a symmetric field profile is achieved, the fields of the two opposite cells with the largest field deviation (at the low side) are increased. The field distribution is checked every 10 to 30 kHz frequency increment. This process continues until the field distribution comes reasonably close to the desired goal. The electric field profile was tuned to

within 2% of the design. Table 4.6 shows the RF properties of the cavity after the

Table 4.6: RF properties of the copper cavity after the final tuning.

frequency (MHz)	Q_L	β
805.199	14957	1.361

last tuning. As a result of tuning the field profile, both the frequency and coupling coefficient were increased. The 200 MHz offset in the frequency is well within the bandwidth of the klystron; so it could be accommodated during high power operation. The measured coupling coefficient corresponds to 2.3% reflected power. Since the input power into the cavity is proportional to the square of the cavity gradient, there is a 1.2% reduction in the achievable gradient. In retrospective, the field distribution shouldn't be tuned to the 1% level because increasing the fields in the coupling cell and the opposite end cell raises the coupling coefficient, resulting in larger reflected power. A compromise should be made to have a lower field distribution in exchange for lesser power reflection.

Chapter 5

High Power Test

The goals of the high power test were the following: (1) determine the maximum attainable accelerating gradient under stable cavity operating conditions, (2) characterize the dark current (electron emissions) from the cavity, (3) study the effects of high power and high magnetic field operations on cavity out-gassing, radiation emission, RF breakdown and dark current emission, and (4) study the effects of high radiation and high magnetic field on the cavity. The high power test began with RF processing of the cavity without the solenoidal field. When the RF processing reached peak klystron output power at stable cavity vacuum and radiation level, the solenoidal field was turned on. During this period, the solenoid was turned on and off to study the effects of the solenoidal field. The high power test concluded with nitrogen gas processing of the cavity.

The 6-cell cavity was high power tested in lab G of Fermilab. A schematic diagram of lab G and the cavity system is shown in Fig. 5.1; and a picture in Fig. 5.2. The cavity system and the 5 Tesla superconducting solenoid were housed inside a concrete enclosure of inner dimensions 12'×18'×8' (length×width×height). As shown

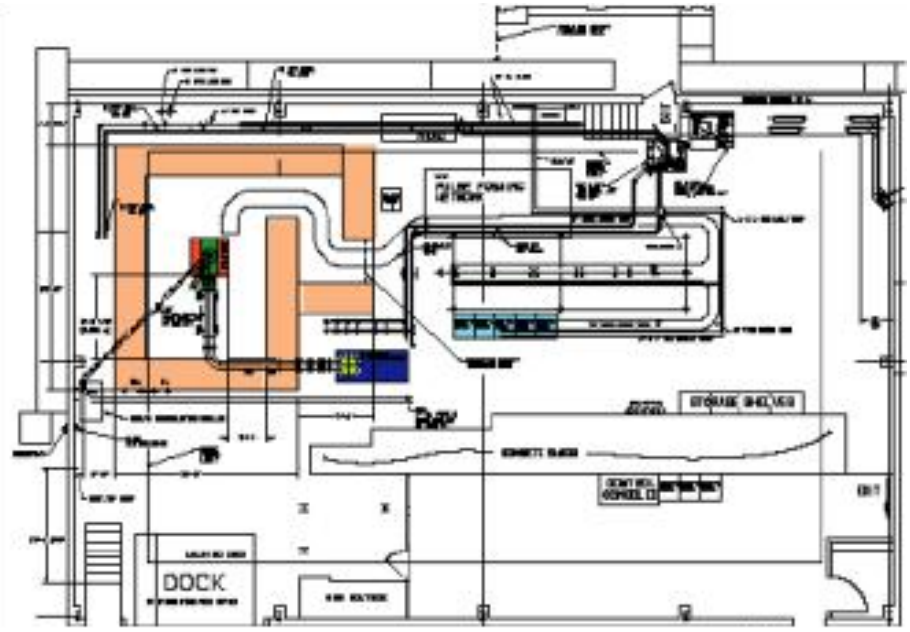

Figure 5.1: The floor plan of lab G. The enclosure of the cavity is located at the upper left hand corner.

in Fig. 5.2, five of the six cells of the cavity was inside the solenoid. The coupling cell and the power transmission waveguide were outside of the core of the solenoid. The other end of the cavity was about one foot from the end of the solenoid. The electric probes for measuring the cavity field signal were located at the cavity ends above the beam pipes. Two directional coupler output lines were located on the waveguide as shown in the upper right hand corner of Fig. 5.2. They were used to measure the input power to and the reflected power from the cavity. The cavity vacuum was maintained by an ion pump which is the rectangular box located at the lower left hand side in Fig. 5.2. The pump was connected to the cavity vacuum through a vacuum port at the transition waveguide that was located directly above the cavity. The ion pump operated between 10^{-7} and 10^{-9} Torr. An auxiliary (backup) getter pump was

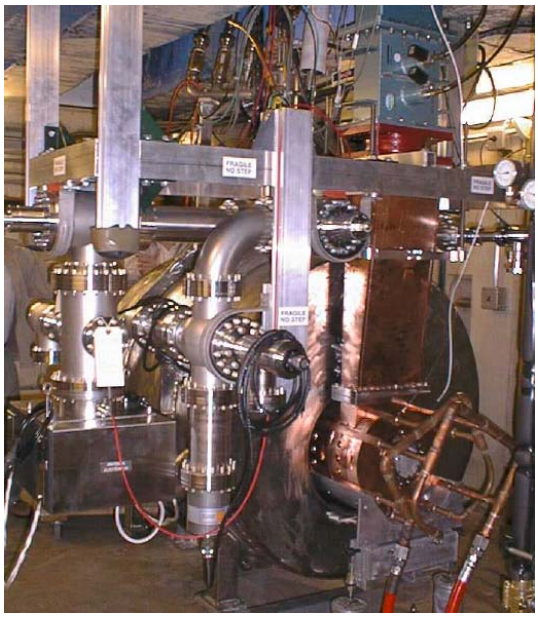

Figure 5.2: The 6-cell cavity system inside the lab G enclosure. The cavity was housed in the 5 T superconducting solenoid.

installed adjacent to the ion pump. The cavity was water cooled and maintained at a temperature of 34.8° C (with 1° C tolerance) by an industrial chiller. The power source for the cavity was a 12 MW klystron (Fig. 5.3) with an operating bandwidth of about 1% of 805 MHz.

5.1 Determination of the Accelerating Gradient

An important task of cavity high power test was to determine the maximum sustainable accelerating gradient under conditions of stable cavity vacuum and radiation emission. The input power to the cavity was determined by measuring the forward power to and reflected power from the cavity. Input power together with the shunt impedance of the cavity yield the total accelerating gradient across the cavity. The ac-

Figure 5.3: The 12 MW klystron for the high power test of the 6 cell cavity. The high voltage transformer for the klystron electron source is shown at the foreground of the klystron.

celerating gradient was checked by measuring the momenta of the electrons produced by field emission in the cavity.

The forward and the reflected powers were measured by two 60 db directional couplers inserted at the long face of the waveguide upstream of the RF window. The RF window was located upstream of the transitional waveguide section. The extracted powers were analyzed with a peak power analyzer (Hewlett Packard, 8991A). An example of the power measurement with a RF pulse of 19 μs (3 times the cavity time constant) is shown in Fig. 5.4. The accelerating gradient (E) is calculated from the input power (P) per unit length using the relation $E = (31 \times 10^6 P)^{1/2}$ [V/m]. The highest accelerating gradient obtained was about 21 MV/m for an input power of 14 MW.

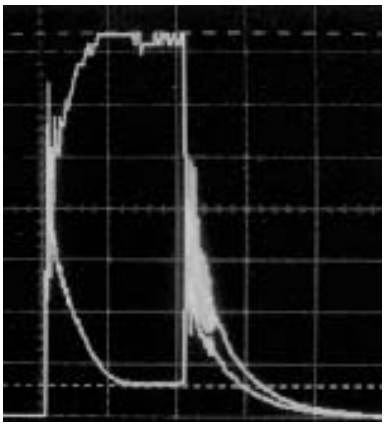

Figure 5.4: Time signals of the forward power (upper curve) to and reflected power (lower curve) from the cavity.

The cavity gradient was checked by measuring the momenta of the field emission electrons coming out of the cavity. A magnetic spectrometer as shown in Fig. 5.5 was used to measure the momentum distribution of the electrons. The spectrometer

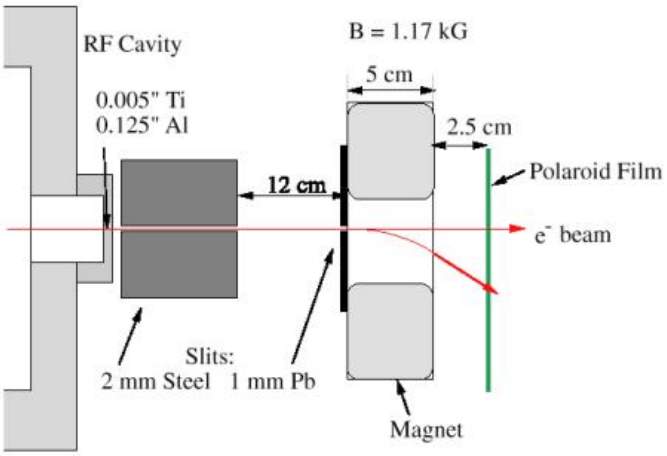

Figure 5.5: Top view of the magnetic spectrometer for the momentum measurements of the field emission electrons.

was constructed using thin steel sheets and two 2.54 cm thick[1] ceramic permanent

[1]The thickness of the magnet points along the direction into or out off the drawing in Fig. 5.5.

magnets. The gap region had a cross sectional area of (4×5) cm and a height (thickness) of 2.54 cm. The maximum field inside the gap was 0.117 T. Downstream of the magnets, Polaroid film was used to detect the bending electrons. In order to have good electron image on the Polaroid film, steel and lead blocks were used as collimators to select a thin strip of electrons into the spectrometer. The top portion of the electrons emerging from the steel collimator was allowed to pass over the magnets (undeflected) to the film and served as the reference line for displacement measurements. The arrangement of the collimators and the small aperture of the magnet allowed only measurements of the higher momentum electrons. Lower momentum electrons were absorbed either by the collimators or not pass through the entire magnet.

Example of the spectrometer measurement is shown in Fig. 5.6 for the case of

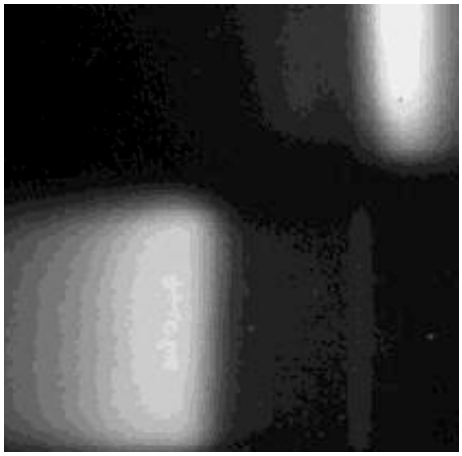

Figure 5.6: Polaroid image of a magnetic spectrometer measurement with 6 MW of input power. The image on the right are the undeflected electrons.

6 MW input power to the cavity. The momentum spectrum in Fig. 5.7 yields a maximum momentum of about 10 MeV/c. This equals about 74% of the value obtained

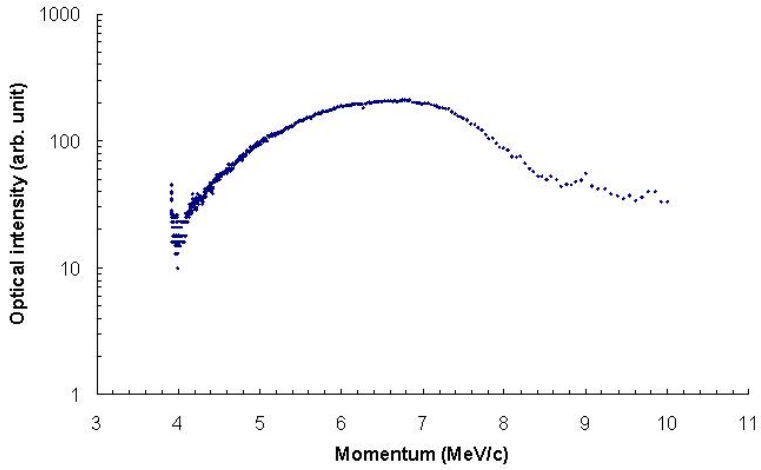

Figure 5.7: Momentum measurements of the field emitted electrons using magnetic spectrometer with 6 MW of cavity input power. The vertical scale corresponds to the optical intensity (arbitrary unit) in Fig. 5.6.

using the cavity input power and shunt impedance. The electrons didn't acquire the full momentum because of the transit time effect and the fact that the cavity cell length was designed (or tuned) for muon with a velocity ratio of $v/c = 0.87$. Muons traveling on axis with the design velocity ratio and a synchronous phase of $\phi_s = 0$ would receive 76% of the full momentum (due to transit time effect) upon traversing the entire cavity. The two percent discrepancy in the maximum electron momentum gain was possibly due to: (1) electrons were originated off-axis and (2) electrons were not in phase with the RF field. In conclusion, the accelerating gradient determined from the input power was consistent with the magnetic spectrometer measurement.

5.2 Characterization of the Dark Current

Dark current emissions in cavities can limit accelerating gradient, cause RF breakdown, and damage cavity surface. Therefore, it is important to study dark current

emissions from cavities. Generally speaking, dark current is the electron emissions from the high electric field regions of the cavity surface under high power operation. During high power operation, some emitted electrons are accelerated by the electric field in the cavity and escaped into the beam pipes, while others hit the cavity walls, possibly damaging the walls and creating additional electrons or X-ray. Large dark current would produced significant beam loading in the cavity and limit the accelerating gradient. High levels of dark current and X-ray can create large backgrounds for beam detectors in muon cooling experiment.

5.2.1 The Sources of Dark Current

When a high electric field is applied to the surface of a metal, electrons can tunnel through the reduced potential barrier. Fowler and Nordheim [18] showed that the tunneling current density j in A/m^2 is

$$j(E) = \frac{A_{FN}E^2}{\phi} exp\left(-\frac{B_{FN}\phi^{3/2}}{E}\right) ,$$

where $A_{FN} = 1.54 \times 10^6$ and $B_{FN} = 6.83 \times 10^3$ are calculated parameters, E is the applied electric field in MV/m and ϕ is the work function in eV. For copper, ϕ is about 4.6 eV. The emitted current is $I = jA_e$ for an effective emission area of A_e. The theory had been confirmed by experiment [19] with point-like emitters. Past experiments with RF cavities showed that the measured dark current also obeyed the functional form of the Fowler and Nordheim law, but with magnitude much higher than the theoretical prediction [20]. The field enhancement factor β_{FN} was introduced as a multiplicative factor to the electric field E to fit the data. Hence the dark current

becomes

$$I(E) = \frac{A_{FN} A_e (\beta_{FN} E)^2}{\phi} exp\left(-\frac{B_{FN}\phi^{3/2}}{\beta_{FN} E}\right) \ . \tag{5.1}$$

The field enhancements in RF cavities are possibly due to surface roughness and contaminant particles from handling and machining.

5.2.2 Dark Current Measurements

Dark Current Amplitude

The dark current was measured over a wide range (10^{-14} A to 10^{-1} A) with three kinds of devices. Beam transformer (which is essentially a current loop) measured dark current in the range of 2 mA up to 200 mA. The signal saturated at about 200 mA and was lost in the noise below 1 mA. For dark current measurements at sub-mA level, the SmartIon radiation monitor was used. It is an ionization chamber type of device and has a range of about 5 orders of magnitude. A photomultiplier tube (PMT) with a 5 cm diameter times 2.5 cm thickness scintillator was used to measure dark current at 10^{-10} A level and below. The measurements took place at the exit of the beam pipe where the dark current was the strongest. Since all devices were sensitive to magnetic fields, the measurements were made with the solenoid off.

Example of dark current measurement using the beam transformer for a 19 μs RF pulse is shown in Fig. 5.8. The cavity field signal was measured directly by RF probe at the cavity. The dark current signal shows that dark current rises as the cavity field rises and drops off rapidly at the end of the RF pulse. Measurements with larger RF pulse widths (*i.e.*, more RF flat top) showed that the dark current leveled off as the RF reached flat top. This implied that the dark current depends only on the peak

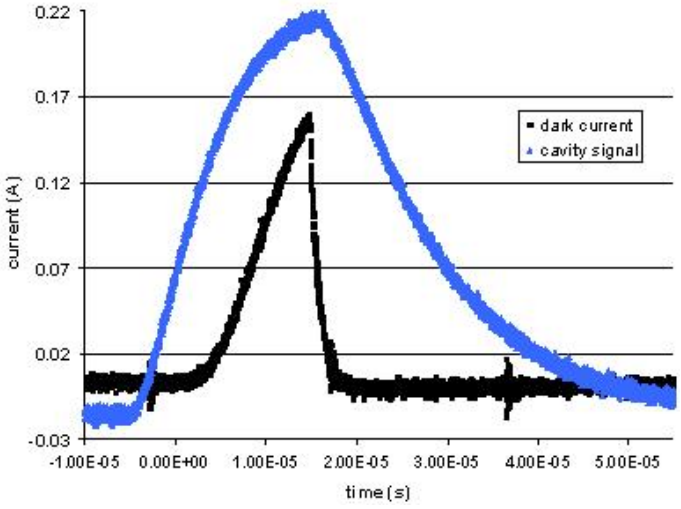

Figure 5.8: Dark current measurement using beam transformer for an input power of 10.5 MW and a 19 μs RF pulse. The larger signal is the trigger (cavity field signal) in arbitrary unit. The smaller signal is the dark current in units of A.

cavity field.

Dark current measurements at sub-MW of cavity input power were made by the scintillation counter. Example of a measurement for a 19 μs RF pulse is shown in Fig. 5.9. The dark current rate was assumed to be proportional to the electron counting rate in a 2 μs interval at the end of the RF pulse.

The results of dark current measurements are summarized in Fig. 5.10. The data show that electron field emissions follow the Fowler-Nordheim law, but with significant emission enhancement. The field enhancement factor was about 700 in the early days of the high power test and decreased to about 400 before the application of the solenoid. The effective emitter areas were in the range of about 1×10^{-6} m^2 to 6×10^{-6} m^2. Since only the high current data are real concern in practice, it is useful to approximate the dependence of the high current data on the accelerating

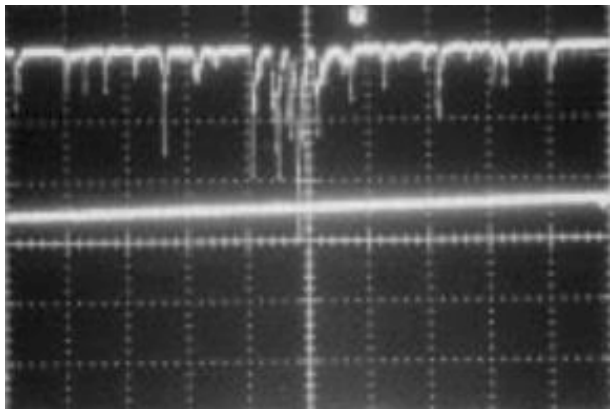

Figure 5.9: Dark current measurement using photomultiplier tube for an input power of 700 kW and a 19 μs RF pulse. The upper curve shows the individual electrons. The dark current was measured by counting individual electrons over 2 μs of the flat top of the cavity field signal (bottom curve).

gradient. The four sets of high current data (in Fig. 5.10) can be approximated by power laws E^n where E is the accelerating gradient in MV/m. The exponent n ranges from about 8 to 12. The highest dark current measured is in excess of 440 mA for cavity input power of 11 MW or more.

Microstructure of Dark Current

The microstructure (*e.g.*, width and shape) of the dark current pulse $I(t)$ was studied using a coaxial Faraday cup (Fig. 5.11). A Faraday cup is essentially a beam dump with a cylindrical (coaxial) geometry. It was tuned to 50 Ω with a time domain reflectometer. The charge of the dark current pulse was collected by the Faraday cup and discharged through a 50 Ω terminal. The voltage pulse $V(t)$ was analyzed by a HP 8593A Spectrum Analyzer. Fourier transformation of the pulse yielded the dark current spectrum. The spectrum appears as a series of harmonics of the

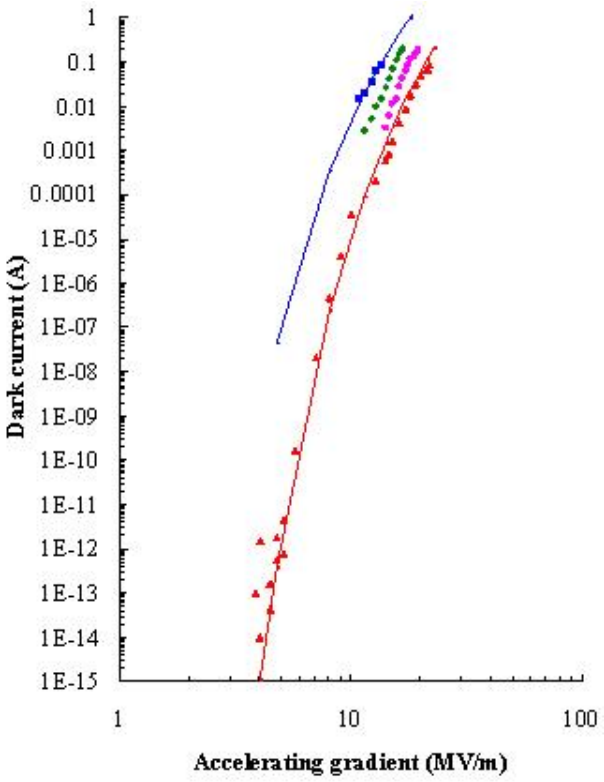

Figure 5.10: Dark current emissions follow Fowler-Nordheim (FN) law with field enhancement factors in the range of about 400 to 700. The effective emission area ranges from about 1×10^{-6} m^2 to 6×10^{-6} m^2. The line to the left is the FN fit with field enhancement factor 700 (in the early days of the high power test) and the line to the right is for field enhancement factor 400 (at the end of the high power test). (Note that these measurements were done before the turn on of the solenoid.) The upper portion of the data set (*i.e.*, the four sets of high current data) are the beam transformer measurements.

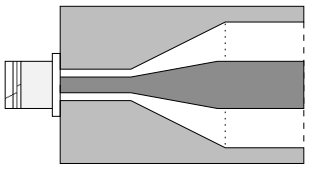

Figure 5.11: Schematics of a copper coaxial Faraday cup for microstructure study of the dark current.

drive frequency 805 MHz as shown in Fig. 5.12. According to the data, the first few

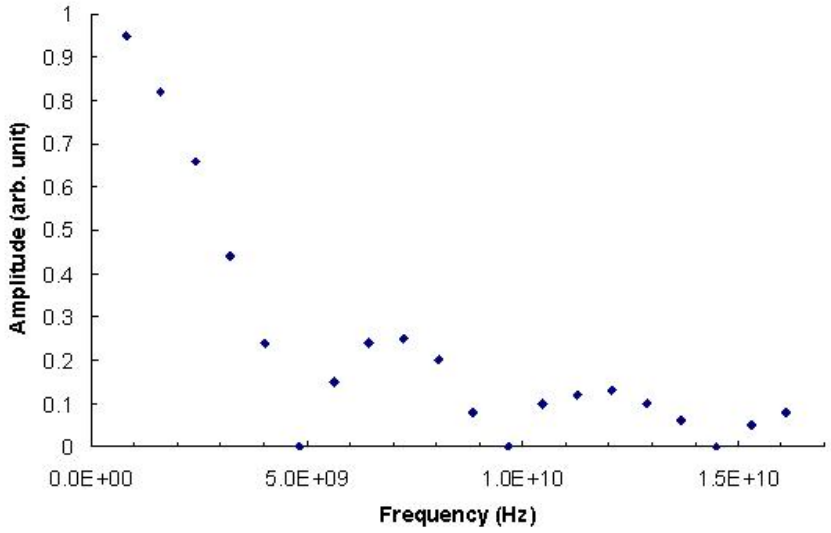

Figure 5.12: Spectrum (frequency components) of the dark current pulse appears as a series of harmonics of the drive frequency 805 MHz. The first 20 harmonics are measured.

harmonics dominate the pulse and a minimum occurs at every sixth harmonic. The first 20 harmonics were used to reconstruct the approximate shape of the dark current pulse. Equal phases were assumed for the different harmonics. The reconstructed pulse is shown in Fig. 5.13. The dark current pulse is basically a rectangular pulse with a full width of about 250 ps.

5.3 RF Processing of the Cavity

This section presents the results of RF processing of the 6-cell cavity with and without the solenoidal field. In general, the purpose of RF processing is to condition the cavities for stable beam operation. During initial high power operation, a virgin cavity generally has poor vacuum, high sparking (RF breakdown) rate and high radiation

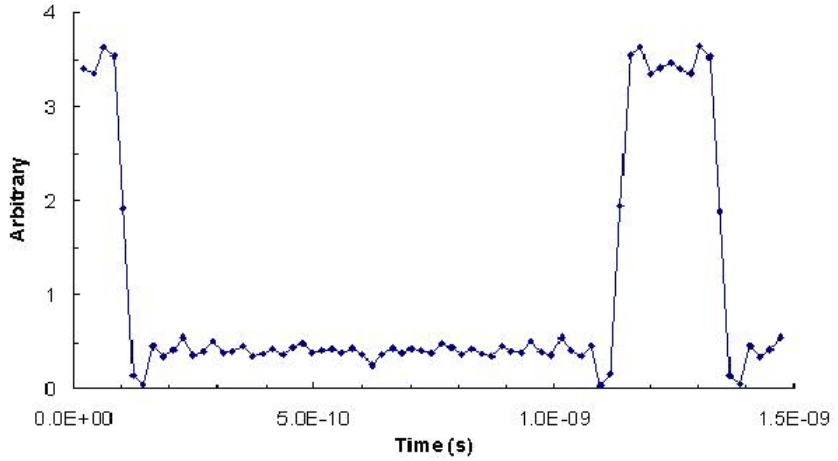

Figure 5.13: Reconstructed dark current pulse using the first 20 harmonics. The full width of the pulse is about 250 ps, which is 21% of the RF period.

emission. This is usually due to the release of trapped gases from the cavity surface and the presence of contaminant particles and roughness on the cavity surface. High power RF processing burns off trapped gases and contaminant particles from the RF surface, and smooths out surface roughness. As a result, the cavity vacuum is improved and the radiation emission from cavity is decreased. At the end of the processing, the cavity usually runs at conditions of stable high vacuum, low sparking rate and low radiation emission. These are optimum cavity conditions for stable beam operation. This high power conditioning process is called RF processing of a cavity.

The RF processing of the 6-cell cavity had three phases: (1) the cavity was high power tested to peak klystron power, (2) the solenoidal field was introduced into the cavity together with the RF, and (3) the cavity was RF processed with nitrogen gas filling the cavity. In phase 1, the cavity was processed such that the maximum RF power applied to it was increased by 0.5 MW per day. In a typical day, RF power

was increased in small amount at a time. For each power increment, the power level was held constant until the radiation and the vacuum pressure came down. This usually took a few hours. The effects of RF processing were studied by monitoring the cavity vacuum and the radiation emission from the cavity. In addition, the dark current emission was measured at various times during RF processing. The rate of RF breakdown in the cavity was also monitored. After phase 1, the solenoid was turned on together with the RF power. Then a procedure similar to that of phase 1 was repeated in the presence of the magnetic field. After phase 2, the solenoid was turned off and the cavity was RF processed with nitrogen gas.

The vacuum pressure of the cavity varied over several orders of magnitude throughout the history of RF processing. The vacuum pressure started at 3×10^{-6} Torr when the cavity first turned on at 70 kW of input power and stabilized at a minimum of about 4×10^{-9} Torr after reaching 12 MW in 8 weeks of processing. This implied that the cavity interior was fairly clean with little out-gassing[2] at the end of phase 1 RF processing. When the cavity was left idle (*i.e.*, no RF input) overnight, the vacuum pressure was about 1.5×10^{-9} Torr the next morning. In the absence of the solenoidal field, the vacuum pressure generally increased each time the input power was raised to new level. Then it gradually stabilized to a lower pressure. The presence of the solenoidal field usually increased the vacuum pressure to the level of 10^{-7} Torr, an indication of enhanced out-gassing and possibly surface breakdown (which will be discussed later). This generally was accompanied with higher dark current emission

[2]Cavity out-gassing is the process in which deposited gases and contaminant particles from the RF surface are burned off and pumped out of the cavity.

and background radiation[3]. The situation was similar to that of the initial turn on of the new cavity where the radiation emission and vacuum pressure were high. The increases in the vacuum pressure and the radiation emission could be reduced by RF processing with the magnet on. The pressure was brought back to 10^{-9} Torr level. Thus, every application of the solenoid required the repeat of RF processing for the cavity.

The partial pressures of the gases in the cavity were studied by the residual gas analyzer (RGA). Examples of the gas partial pressures are shown in table 5.1. The

Table 5.1: Partial pressures (nTorr) of gases in the cavity.

Gas	RF off	RF on	RF and solenoid on
H_2	7.8	9.2	3.1
O_2	2	2.5	1.1
H_2O	1.9	2.4	2.1
N_2/CO	9	6	7
CO_2	7.2	7.8	12
Cu	0	< 0.1	0.95

data in the RF off and on columns were taken without the magnetic field and the data in the RF and solenoid on column was taken during magnetic field operation. The vacuum composition shows that the gases are mainly atmospheric gases. When the RF was on, out-gassing occurred in the cavity. The low level of copper in the cavity during phase 1 processing means that there was little surface breakdown (damage). In phase 2 processing, the presence of copper in the cavity was significantly higher by about an order of magnitude. This indicated that surface breakdown was happening

[3]Dark current emission and background radiation in the presence of magnetic field will be discussed at later section.

during solenoid operation.

The radiation history of the cavity during RF processing provides a way to see the effects of high power and high magnetic field operations on the cavity. The radiation history gives indications when there are severe RF breakdown and surface damage happening in the cavity. The radiation emission from the cavity was measured by a radiation monitor located inside the cave at the corner of the entrance. Figure 5.14 summarized the radiation history for 6 months of RF processing (from phase 1 through

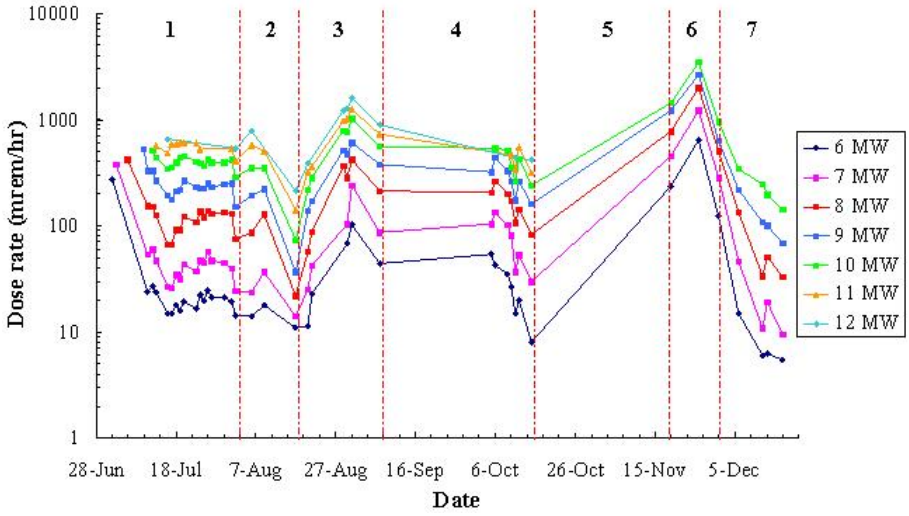

Figure 5.14: The radiation history of the cavity for 6 months of RF processing that started on 5/30. The radiations were measured by the radiation monitor located at the entrance inside the enclosure. Data acquisition started at the end of June. Each curve is for a particular input power level. Regions 1, 4, 6, 7: RF on and solenoid off. Region 2: RF on with solenoid in gradient mode at 3.5 T (maximum). Region 3, 5: RF on with solenoid in solenoid mode at 2.5 T (half of maximum). Region 7: RF processing with nitrogen filling the cavity. It ended on 12/17. The titanium window at the beam pipe end located inside the core of the solenoid was broken on 9/7 and 12/19.

3). During period 1 (a period of about 6 weeks), RF processing reduced the radiations by a factor of about 2 to 20 for the various input power levels. At the end of this

period, the cavity was relatively calm with a sparking rate (sparks/pulse) of less than 0.0002. In period 2, the solenoid was first turned on in gradient mode[4] at 3.5 T together with the RF. The radiations showed initial rises followed by sharp declines due to RF processing. The rises in the radiations were accompanied by a moderate increase in the frequency of RF breakdown. In period 3, the increases of the radiations were more dramatic when the solenoid was operated in solenoid mode at 2.5 T. The radiation levels were increased by a factor of about 7 to 19 in 2 weeks. RF processing lowered the radiations, but the levels were still higher than before. RF breakdown increased sharply during this period with a sparking rate of greater than 0.003. Sometimes RF breakdown, as shown in Fig. 5.15, lasted continuously for

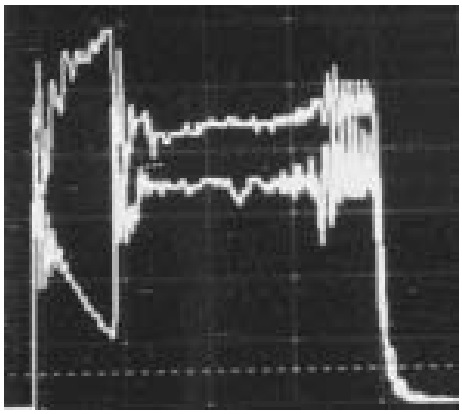

Figure 5.15: RF breakdown during magnetic field operation as manifested in the input power (upper curve) to the cavity and in the reflected power (lower curve) from the cavity. During a RF breakdown, the discharge across the cavity creates a short circuit effect and results in an impedance mismatch situation. The input power to the cavity was quickly reflected as seen from the figure. In a severe RF breakdown, the reflected power equals the input power (*i.e.*, all input power is reflected).

[4]The solenoid was made of two sets of independent coil. The two coils could produce fields in the same direction (called solenoid mode) or in the opposite direction (called gradient mode).

many RF cycles. The sharp increases in the radiation and in the RF breakdown might be an indication that surface breakdown (damage) was occurring in the cavity. On 9/7 (near the end of period 3), the titanium window at the beam pipe end located inside the solenoid was broken. After the replacement of the broken window, the cavity was operated without the magnetic field (period 4) in an attempt to find out whether solenoid operation had caused the window breakdown. During this period, the radiation levels were steady for the first three and half weeks, followed by sharp declines. This was RF processing at work. No visual damage was found on the titanium window. Next, the solenoid was turned on again in solenoid mode with RF (period 5). The radiations increased by a factor of about 6 to 30 in 4 weeks. Cases of continuous RF breakdown were common events. Severe RF breakdown prevented the cavity input power to go beyond 10 MW. Dented marks and traces of discoloration were found on the titanium window during this period. The solenoid was turned off and the cavity was RF processed (period 6). Surprisingly, the radiation levels continued (in the absence of the magnetic field) to rise to maxima before they declined. The radiation increases were possibly due to the surface damages initiated in the previous period. The radiation decreases were again due to RF processing. In period 7, nitrogen gas was introduced into the cavity to see its effects on reducing the amount of radiation[5]. The cavity was RF processed at vacuum pressure levels of 10^{-5} Torr. The magnetic field was not present. In two weeks, RF processing with nitrogen gas decreased the radiation levels by a factor of 7 to 28. Thus, nitrogen RF

[5]Nitrogen RF processing is a discharge cleaning technique using the gas in a metallic chamber. In this method, ions that are produced by high pressure discharges in the cavity presumably scrub the rough RF surface to improve its smoothness.

processing was more effective in reducing the radiation levels of the damaged cavity than normal RF processing. Two days after nitrogen RF processing, the titanium window was broken the second time. During both of the replacements of the broken windows, substantial damages were found at the iris regions of the cavity. Details of the window breakdowns and the cavity damages will be discussed in the next section. In conclusion, the turn on of the magnetic field during RF operation always increases the radiation, and subsequent RF processing was able to reduce the radiation increase. However, the sharp radiation increase during magnetic field operation had caused serious damages on the titanium window. This resulted in subsequent window breakdown.

The behavior of the dark current emission exhibits similar pattern as that of the radiation monitor data. Figure 5.16 displays the dark current data (beam transformer data) as a function of the accelerating gradient at various days during RF processing. Before the application of the solenoid, there was a general trend of the dark current data set to move toward higher values of accelerating gradient (or toward lower dark currents) as RF processing progressed forward. During this period, cavity processing reduced the dark current by about two orders of magnitude, lowered the peak dark current to 100 mA at the maximum gradient and improved the accelerating gradient by about 60%. The application of the solenoid reversed the trend in dark current reduction. The peak dark current (at the maximum gradient) increased by a factor of 2 or more (*i.e.*, beyond 200 mA). Near the end of the high power test, nitrogen gas processing brought the dark current back to lower level.

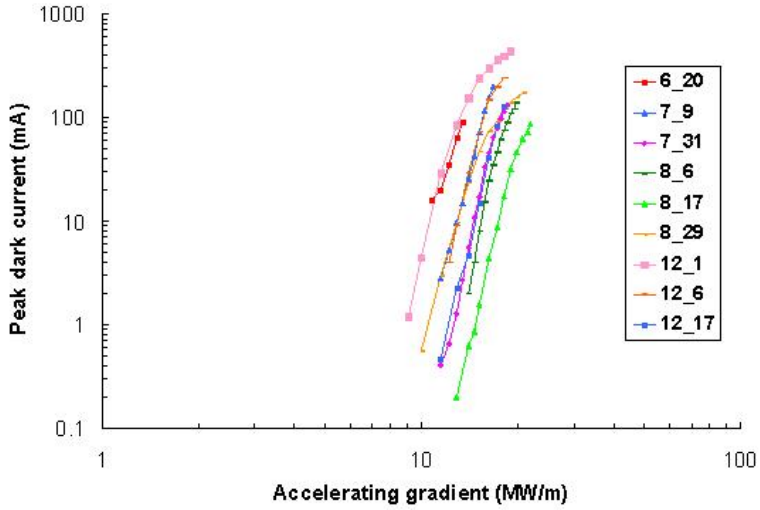

Figure 5.16: The evolution of dark current during RF processing. The data are the beam transformer data. Each curve represents dark current measurement at a particular day. The solenoid was first turned on in solenoid mode on 8/17 and RF processing with nitrogen filling the cavity began on 12/3 and ended on 12/17.

The solenoidal field dependence of the radiation emission was studied after the nitrogen gas processing and the replacement of the second broken titanium window. At this time, the radiation and the vacuum pressure were relatively low and stable. So the effect of RF processing was minimal. The study was carried out using the radiation monitor inside the cavity. The monitor measured only the gross radiation levels in the cave. It could see only the backscattering radiation, not the cavity and solenoid system itself. Figure 5.17 shows that there is a linear dependence of the radiation on the magnetic field for a constant cavity input power[6].

[6]The radiation data were corrected for the magneto-resistivity effect for each magnetic field level.

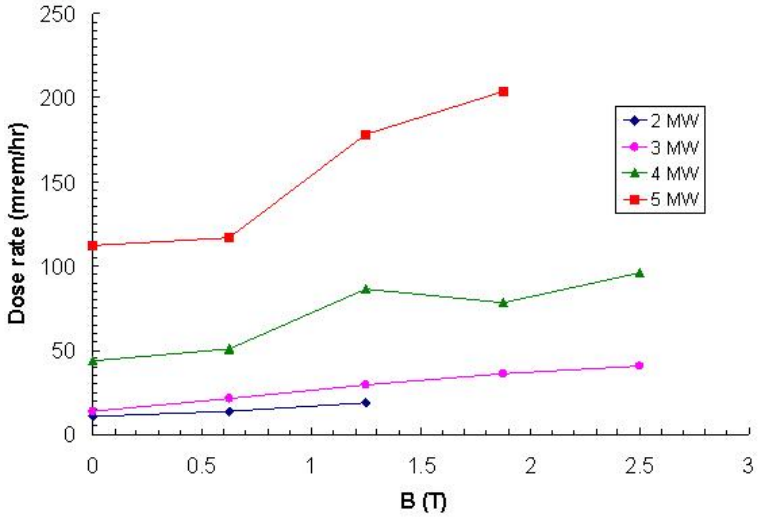

Figure 5.17: The dependence of the radiation emission on the solenoidal field. The radiation data was corrected for the magneto-resistivity effect for each magnetic field level. The different curves correspond to different cavity input powers. The error (random fluctuation) in the radiation readings is about 10 mrem/hr.

5.4 Effects of High Power and High Magnetic Field on the Cavity

The application of the solenoidal field in the cavity environment during high power test had some adverse effects on the cavity. Dark current and radiation emissions were enhanced during solenoid operation (as discussed in previous section). The large increase in dark current emission had damaged twice the cavity titanium window. During the replacements of the titanium windows, serious surface damages were found on the iris regions of the cavity. The presence of copper in the vacuum (detected by the RGA vacuum scan) during magnetic field operation indicated that the surface damages had occurred. This section presents the titanium window and surface damages, and the possible role that the magnetic field played in causing the

damages.

5.4.1 Titanium Window Breakdown and Cavity Surface Damage

The titanium window (125 μm thickness) located at the beam pipe end inside the solenoid was broken in two occasions, and caused cavity vacuum failures and contaminations. The relative positions of the cavity and the solenoid are shown in Fig. 5.18. The damages as shown on the outside face of the window in Fig. 5.19 were basically

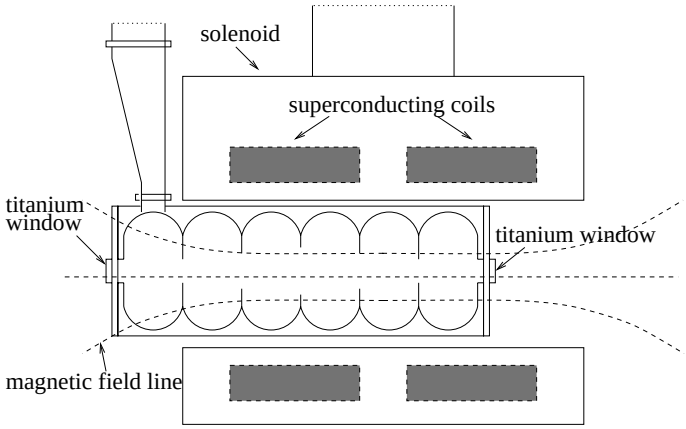

Figure 5.18: Cavity in the solenoid.

grouped into three concentric bands of burned marks. These burned marks were due to the bombardments of the dark current electrons (beamlets) emitted from the three different kinds of irises in the cavity. The three bands of burned marks were off center from the window because of the offset between the cavity and the magnetic axes. An example of a burned through hole on the window that caused the vacuum failure is shown in Fig. 5.20. The interior side of the window (see Fig. 5.21), is covered with copper debris from cavity surface damages. The copper debris are melted onto the

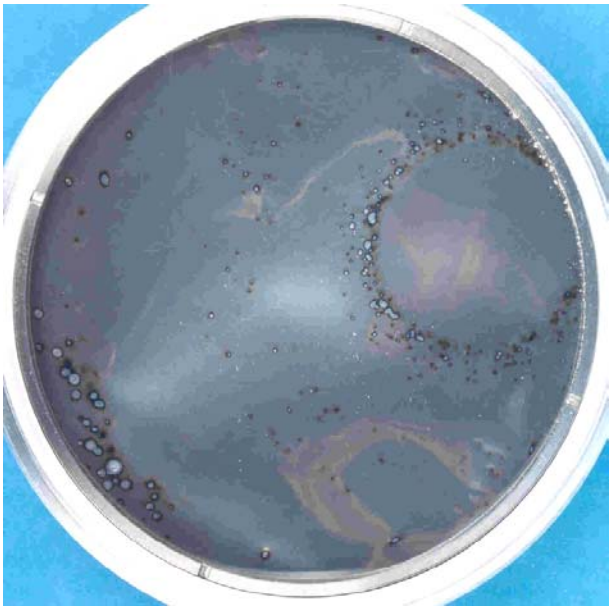

Figure 5.19: Titanium window damages showed on the outside face of the window. The burned marks are basically grouped into three bands. The diameter of the window is 8 cm.

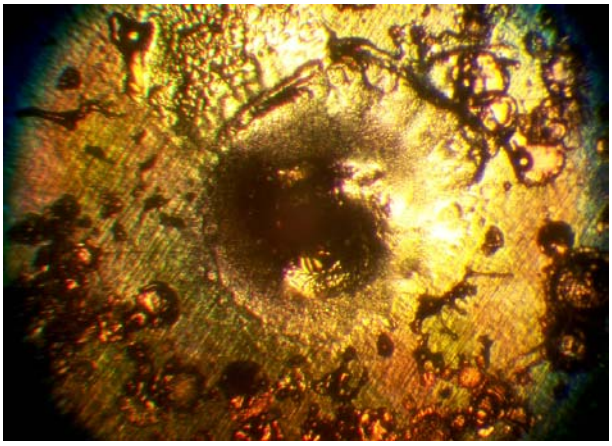

Figure 5.20: Example of a burned hole on the titanium window (shown at the center of the picture) that caused the cavity vacuum leak. The size of the hole is on the order of 0.1 millimeter.

titanium like liquid solders fell on a surface. This indicated that the copper debris coming off the cavity surface was not in solid form. The sizes of the copper droplets

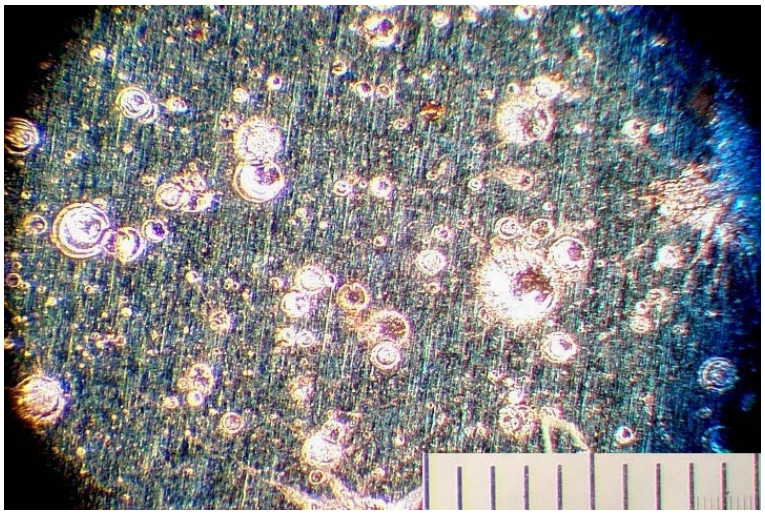

Figure 5.21: Copper debris on the interior side of the titanium window that came from cavity surface damages. The scale has a full length of 1 mm. The largest copper debris on the picture has size of about 0.2 mm.

are on the orders of 0.1 millimeter or less. The titanium window located at the beam pipe end outside of the solenoid suffered no damages (*i.e.* there are no burned marks). However, copper debris was also found uniformly over the interior side of the window.

After the titanium window failure, close examination of the cavity interior revealed that serious surface damages occurred on the irises of all cells, except for the coupling cell which was located outside the bore of the solenoid. Figure 5.22 shows a general view of the damaged irises looking from the broken window direction and Fig. 5.23 gives a close up view of the damages on the first iris. The irises appear to be scared with uniformly distributed pits whose sizes are on the order of a millimeter. The worst damages appeared on the irises of the second cell which was located in the middle of the solenoid. The pitting on the rises was less severe when going toward the coupling cell. Copper debris were found in numerous places such as the titanium

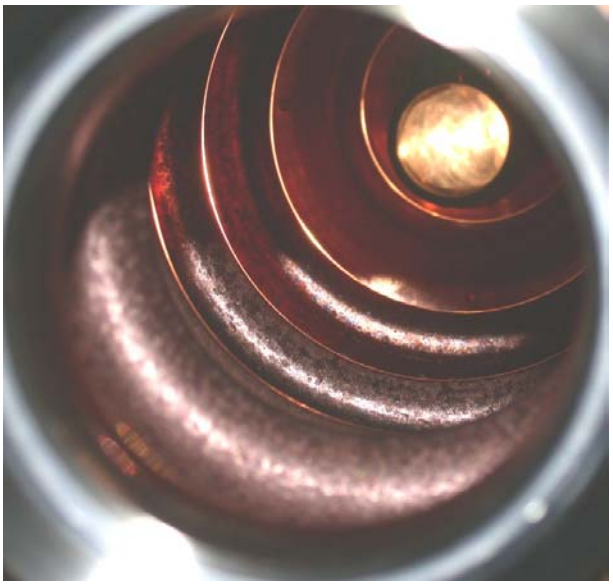

Figure 5.22: General view of the iris damages looking from the broken window direction. The irises (second and third in the picture) of the second cell appear to be damaged the most.

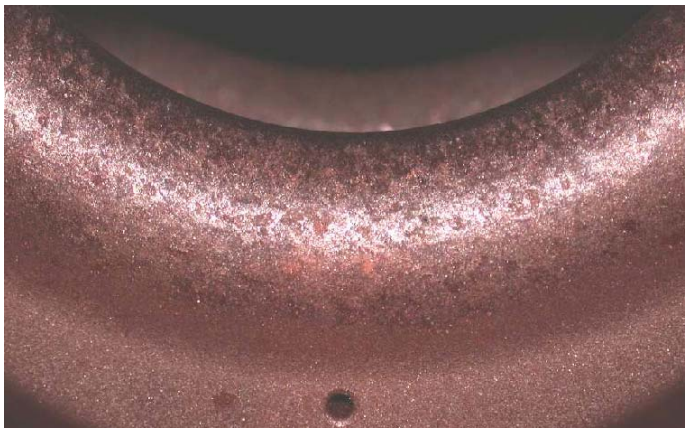

Figure 5.23: Damages on the first iris that was located inside the solenoid. The hole below the iris was a drain hole with a diameter of 1/8". The sizes of the pits are on the order of a millimeter.

windows, the beam pipes, the equatorial regions of the cells and the irises.

The dynamics and physical shape of the dark current (electron) beamlets were

studied using glass plates. Study was first done at the titanium window located inside the solenoid. In order to minimize the multiple scattering effect, the glass plates were placed against the external face of the titanium window. Multiple scattering in the window has limited the spatial resolution of the glass plates to the order of 100 μm. The images of the beamlets created by radiation damage were deposited on the glass plates. Figure 5.24 shows pictures (of glass plates) of beamlets. Only portions of the

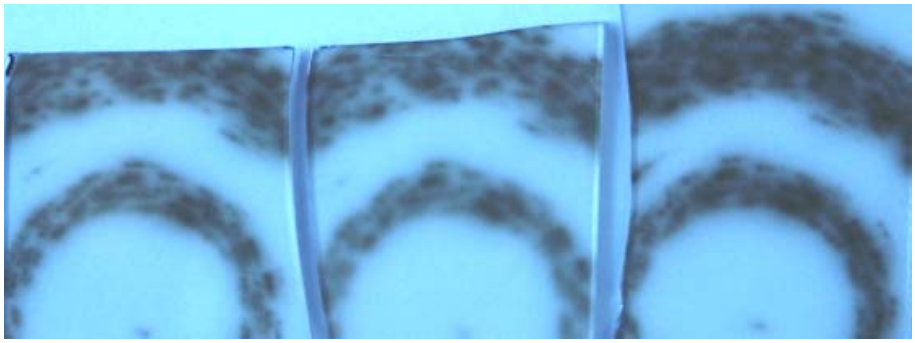

Figure 5.24: Dark current beamlets from the cavity. The sizes of the beamlets are on the orders of 1mm or less.

inner two bands of the beamlet were recorded. Careful examinations of the images indicate that the beamlets are discrete (having sizes on the order of 1 millimeter or less) and uniformly populated. This implies that the beamlets came from localized sources (consisting of one or more emitters) that are evenly distributed on the irises. Indeed, this is consistent with the pattern of pits found on the irises. The optical intensities of the beamlets are not uniform indicating that some sources were stronger dark current emission sites than the other. The stronger current sources presumably have more emitters with larger emission areas. The same study was carried out with glass plate at the titanium window located outside of the solenoid. The radiation

damage was light (indicated by low optical intensity) and uniform on the glass plate. There are no bands of beamlet and discrete damage marks on the plate.

The study of the beamlet's dependences on the accelerating electric field and the solenoidal field showed some interesting features. Lowering of the magnetic field or increasing the electric field turned the beamlets into rings as shown in Fig. 5.25. The

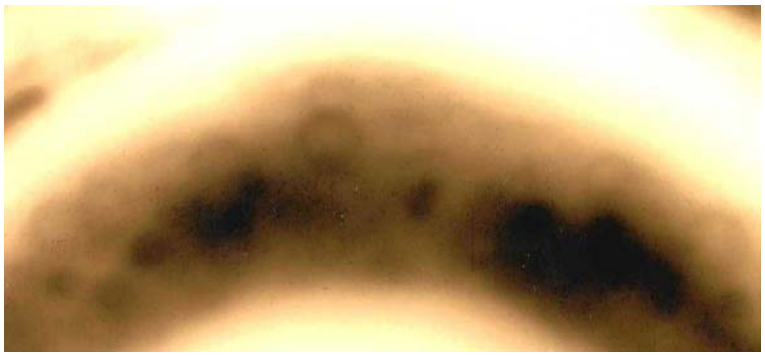

Figure 5.25: Ring structures of the dark current beamlets on the inner band.

radius of the ring was found inversely proportional to the square of the magnetic field and proportional to the electric field as shown in Figs. 5.26 and 5.27. The dynamics of these rings could be explained by electron motion in region of crossed (perpendicular) electric and magnetic fields during the acceleration process. As the electrons traveled through the mostly axial solenoidal field (B), the radial component of the electric field (E) near the irises produced azimuthal drift with orbit radius of $r = \gamma m_{\circ} E/(eB^2)$.

The burned marks and the holes on the titanium windows were produced by local heating due to the dark current beamlets. The windows were heated by ionization losses and the temperature increase should be on the order of $\Delta T = \Delta Q/(cm)$,

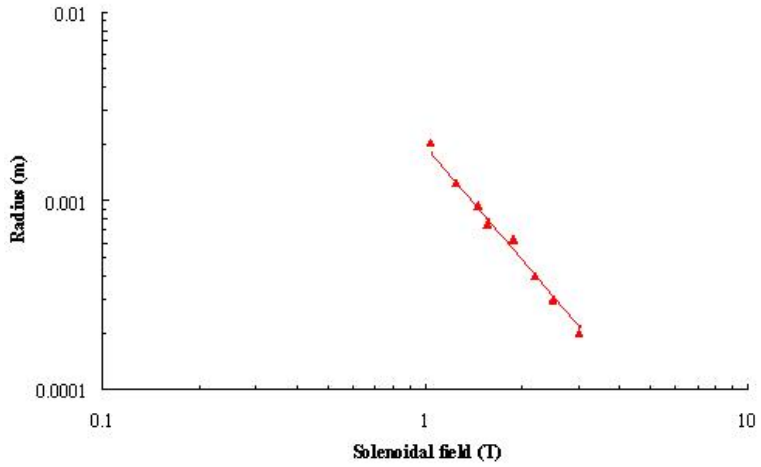

Figure 5.26: Solenoidal field dependence of the radius of the dark current ring. $r \propto 1/B^2$.

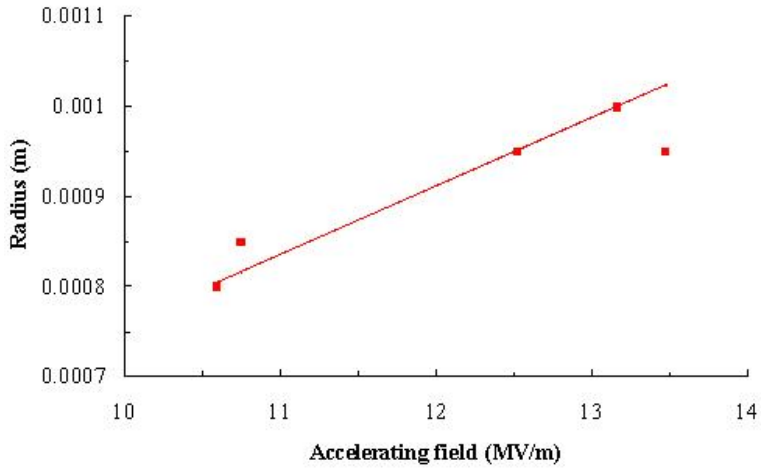

Figure 5.27: Accelerating field dependence of the radius of the dark current ring. $r \propto E$.

where c is the specific heat of titanium, m is the titanium mass in the volume hit by the beamlet, and ΔQ is the deposited energy in the mass volume. Using the measured dark current property, the average beam power could be calculated as $P_d = I_d V_{acc}$ where I_d is the dark current magnitude and V_{acc} is the accelerating volt-

age in the cavity. The energy deposition in the window due to each dark current pulse is $\Delta Q = P_d w$ where $w = 200$ ps is the pulse width of the dark current. The volume of energy deposition was estimated to be the cross section of the beamlet (1 mm$\times$ 1 mm) times the window thickness (125 μm). As an example of heating calculation, let us take a set of high power test parameters of 5 Hz repetition rate, 19 μs RF pulse, 50 mA dark current and 10 MV of accelerating voltage. The temperature rise is about 2500 K. It is sufficient to melt titanium whose melting temperature is about 1950 K.

Since the dark current beamlets had sufficient beam power to produce meltdown in the titanium windows, the beamlets could have caused surface damages. If the dark currents were directed to hit the copper surface by the magnetic field, they could have boiled off copper and created pits on the surface[7]. The pits presumably have rough geometry with sharp points (*i.e.*, emitters). They could have acted as intense dark current emission sites and increased dark current and radiation emissions. The boiled off copper could explained the fact that the copper debris on the windows were similar to liquid solders.

Another possible cause for surface damages is the large surface electric fields at the emission sites. For field enhancement factors in the range of 400 to 700, the local surface electric fields are in the orders of GV/m. This could produce high charge densities, local heating and enormous forces on the surface. Since the force per unit area is proportional to the square of the electric field (*i.e.*, $p = 0.5\epsilon_\circ E^2$), the outward pressure exerted on the surface is in the order of several hundred MPa. This pressure

[7]The melting point of copper is about 1360 K.

range is comparable to the tensile strength of copper which is in the range of 250 to 450 MPa. The outward pressure could break and eject sharp emitters from the surface. The impacts of the break away coppers on other surfaces might create pits and damages.

The absence of damages on the titanium window and in the coupling cell that were located outside of the solenoid could be understood by the magnetic field pattern. In the outside region of the solenoid, the magnetic field lines were strongly divergent. Hence, the dark current beam was diffuse. This was confirmed by the glass plate study of the dark current beamlets. The energy deposition per unit area by the beam would be much less than that of the bore region of the solenoid. Thus, dark current heating in the outside solenoid region didn't cause damages.

After the removal of the cavity from the experiment, low power test was performed on the cavity to see the changes in the RF properties due to the surface damages. The quality factor (loaded Q_l) have changed from 15000 to 13500. The 10% reduction in Q_l resulted in a 5% drop in the accelerating gradient. Experimentally, a few percents reduction in the amplitude of the cavity field signal was observed during times of intense RF breakdown. The π mode frequency have decreased by 13 kHz, while the zero mode frequency increased by 22 kHz. The external coupling coefficient was reduced by 11% which is consistent with the decrease in the quality factor.

5.5 Conclusion

The MUCOOL 805 MHz open iris cavity was tested under high power and high magnetic field conditions. Before the application of the magnetic field, the cavity had reached an accelerating gradient of 21 MV/m for the maximum klystron output power. Under this gradient, the cavity vacuum was stable at 10^{-9} Torr with a sparking rate of less than 0.0002. The dark current emission was consistent with the Fowler-Nordheim field emission for large field enhancement factors. At the maximum accelerating gradient, the dark current was below 100 mA after two months operation.

Cavity operation under the magnetic field had several adverse effects. First, every application of the magnetic field was accompanied by increased dark current emission, cavity out-gassing and RF breakdown. During period of intense radiation emission, dark current was in excess of 400 mA and the sparking rate was greater than 0.003. This required the repeat of RF processing for the cavity. Because of the increased RF breakdown, cavity operation under the magnetic field was limited to about 10 MW of input power. Second, the titanium window at the beam pipe end inside the solenoid was broken twice due to intense dark current heating. The lifetime of the window was one to two months. Third, surface damages occurred in the iris regions that were located inside the solenoid. Large electric field enhancements at the emitters and intense dark current bombardment were contributing factors to the surface breakdown. The deterioration of the cavity occurred with the application of the magnetic field over a three month period. The surface damage was a possible cause for the large increase in the dark current emission because of the increased

numbers of emission sites.

Future R & D work for the MUCOOL cavity is needed to study the issues of surface damage and dark current reduction. Here are some study topics for improving the cavity performance: (1) study of methods to reduce the large electric field enhancement factor at the emitters (some of the methods are electropolishing and gas processing), (2) since the surface electric field enhancement should depend on the characteristic of the RF surface and the surface geometry, the nature of the emission sites needs to be closely examined before and after the high power test, (3) coating the interior cavity surface (high electric field regions) with material that has high melting point and low vapor pressure to lower the risk of surface damage needs to be studied (examples of coating materials are steel and tungsten), and (4) study of different cleaning technique such as high pressure rinsing to better flush out contaminant particles from the surface so as to reduce potential dark current emitters. To facilitate the studies of these issues, a single cell cavity with geometry similar to that of the 6-cell cavity should be used. The single cell cavity allows better access to the interior of the cavity for study and diagnosis.

In conclusion, the present R & D results of the open iris cavity implied that the cavity is not suitable for use in the muon cooling channel of the muon collider. This is due mainly to the facts of cavity deterioration (*e.g.*, surface damages) under high magnetic field operation and large dark current emission. The cavity is also not suitable for single particle muon cooling experiment because the large dark current flux will inevitably create large backgrounds for the beam detectors. Further R & D

work is required to improve the breakdown field level and the lifetime of the cavity and to reduce the dark current flux.

Bibliography

[1] Juan C. Gallardo, *et al.*, *Status of Muon Collider Research and Development and Future Plans*, BNL-65623, Fermilab-PUB-98/179, LBNL-41935.

[2] S. Geer and R. Raja, *Workshop on Physics at the First Muon Collider and at the Front End of the Muon Collider*, (Fermilab, Nov. 1997), AIP Conf. Proc. 435, 1998.

[3] The $\mu^+\mu^-$ Collider Collaboration, $\mu^+\mu^-$ *Collider Feasibility Study*, BNL-52503, FERMILAB-Conf-96/092, LBNL-38946, July 1996.

[4] The MUCOOL Collaboration, *Ionization Cooling Research and Development Program for a High Luminosity Muon Collider*, Proposal 904, Fermilab, April 15, 1998.

[5] A. N. Skrinsky and V. V. Parkhomchuk, *Sov. J. Nucl. Phys.* **12**, 3 (1981).

[6] E. A. Perevedentsev and A. N. Skrinsky, *Proc. 12th Int. Conf. on High Energy Accel.*, p.485, 1983.

[7] D. Neuffer, *Proc. 12th Int. Conf. on High Energy Accel.*, p.481, 1983.

[8] U. Fano, *Annual Review of Nuclear Science* **13**, 1 (1963).

[9] D. Neuffer and A. Van Ginneken, *Nucl. Instrum. & Methods* **A403**, 1 (1998).

[10] Robert E. Collin, *Foundations For Microwave Engineering*, 2nd Ed., McGraw-Hill, 1992.

[11] Computer Simulation Technology, *MAFIA 4*, Germany.

[12] A. Moretti, *et.al.*, Proceedings of the XX International Linac Conference, August 18, 2000.

[13] D. Li, *et.al.*, Proc. of 1998 Linac Conf., p.977, Chicago, 1998.

[14] The MathWorks Inc., *MATHLAB v.6*, United States.

[15] Mark Champion, Fermilab, private communication, 1999.

[16] John C. Slater, *Microwave Electronics*, D. Van Nostrand Company, 1950.

[17] S. W. Kitchen and A. D. Schelberg, *Jour. of Appl. Phys.*, **26**, 5 (1955).

[18] R. H. Fowler and L. Nordheim, Proc. Roy. Soc. (London) A, *Math. Phys. Sci.*, **119:173** (1928).

[19] W. P. Dyke and J. K. Trolan, *Phy. Rev.*, **89**, 4 (1953).

[20] H. Padamsee, J. Knobloch and T. Hays, *RF Superconductivity For Accelerators*, John Wiley & Sons, 1998.

[21] John D. Jackson, *Classical Electrodynamics*, 2nd Ed., John Wiley & Sons, 1975.

[22] David M. Pozar, *Microwave Engineering*, 2nd Ed., John Wiley & Sons, 1998.

[23] George L. Ragan, *Microwave Transmission Circuits*, pp 188-193, Boston Technical Publishers, 1964.

[24] Edward L. Ginzton, *Microwave Measurements*, McGraw-Hill, 1957.

[25] Thomas P. Wangler, *Principles of RF Linear Accelerators*, John Wiley & Sons, 1998.

[26] S. Humphries, *Charged Particle Beams*, John Wiley & Sons, 1990.